Development of Multi-channel Radio Frequency Technology for Anatomical and Functional Magnetic Resonance at Ultrahigh Fields: Design, Evaluation and Clinical Application

D i s s e r t a t i o n

zur Erlangung des akademischen Grades
d o c t o r r e r u m n a t u r a l i u m
(Dr. rer. nat.)
im Fach Biophysik

eingereicht an der
Lebenswissenschaftlichen Fakultät
der Humboldt-Universität zu Berlin

von
Dipl.Ing. Andreas Gräßl

Präsident der Humboldt-Universität zu Berlin

Prof. Dr. Jan-Hendrik Olbertz

Dekan der Lebenswissenschaftlichen Fakultät

Prof. Dr. Richard Lucius

Gutachter/in:
1. Prof. Dr. Thoralf Niendorf
2. Prof. Dr. Adam Lange
3. Prof. Dr. Martin Falcke

Tag der mündlichen Prüfung: 28.04.2016

Zusammenfassung

Magnetresonanztomographie (MRT) ist eine nichtinvasive Bildgebungsmethode, die in der Medizin sowie in der Forschung eingesetzt wird und auf der magnetischen Kernresonanz beruht. Die Erforschung der Ultrahochfeld (UHF) MRT ab Magnetfeldstärken von 7.0 Tesla und darüber ist durch einen intrinsischen Signalgewinn hin zu hohen Magnetfeldstärken motiviert und beschäftigt sich mit den dabei auftretenden physikalischen Effekten ebenso wie mit den dazu notwendigen neuartigen Technologien. Die vorliegende Arbeit untersucht Mehrkanalantennen zur Anregung der magnetischen Kernresonanz sowie zum Empfang des resultierenden Signals bei 7.0 T. Für die magnetische Kernresonanz von Protonen ergibt sich eine Resonanzfrequenz von 300 MHz. Die zugehörige Wellenlänge in menschlichem Gewebe verlässt in diesem Frequenzbereich im Verhältnis zu den Körperabmessungen den quasistatischen Bereich. Die sich ergebende Wellenausbreitung hat Interferenzmuster in den erzeugten Bildern zur Folge, die zu klinisch nicht verwertbaren Bildinformationen führen können. Vor diesem Hintergrund wurden in dieser Arbeit Mehrkanalantennen mit 4, 8 und 16 unabhängigen Elementen zur Signalanregung und zum Empfang konzipiert, aufgebaut und untersucht. Die Erkenntnisse mündeten in der erfolgreichen Implementierung der weltweit ersten 32-Kanal Antenne zur kardiovaskulären Bildgebung bei 7.0 T. Auf Basis numerischer dreidimensionaler Simulationen der elektromagnetischen Felder wurde die Ansteuerung der einzelnen Antennen hin zu einem in Summe homogenen elektromagnetischen Wechselfeld optimiert. Die Leistungsfähigkeit der neuartigen Antennenkonfigurationen konnte in ihren jeweiligen Anwendungsgebieten in der kardiovaskulären, muskuloskeletalen und orbitalen Bildgebung in vorklinischen Studien belegt werden. Neben der Bildgebung auf Basis von Wasserstoffatomen wurde eine 4-Kanal Antenne zur Bildgebung auf Basis von Natriumatomen entwickelt, welche die ersten auf der Natriumkonzentration beruhenden bewegten Bilder des menschlichen Herzens bei 7.0 T ermöglichte. Der Zusammenhang zwischen Natriumkonzentration und Zellintegrität ermöglicht direkte und ortsaufgelöste Einblicke in physiologische Prozesse. Die Ergebnisse dieser Arbeit belegen die breite Anwendbarkeit von Mehrkanalantennen in der UHF MRT zur Protonen- und Natriumbildgebung und bilden eine solide technologische Basis für breitere klinische Studien, um die Ultrahochfeld MRT reif für den routinemäßigen Einsatz im Gesundheitswesen zu machen.

Schlagwörter: Biomedizinische Bildgebung, Magnetresonanztomographie, Ultrahochfeld MRT, Lokale Sende-und Empfangsspulen

Abstract

Magnetic resonance imaging (MRI) is a non-invasive imaging method based on the effect of nuclear magnetic resonance. It is used in healthcare as well as in research. It offers a wide range of soft tissue contrasts and means to depict the physiological function of tissue. MRI at magnetic field strengths of 1.5 Tesla and 3 Tesla is well established. The gain in signal-to-noise ratio (SNR) intrinsic to higher magnetic field strength fuels the vigorous research field of Ultrahigh field (UHF) MRI at 7.0 T and above. Nevertheless for MRI based upon proton imaging the wavelength of the transmitted electro-magnetic fields slowly departs from the semi-static regime and reaches the dimension of the transection of the human body at 7.0 T. This gives rise to constructive and destructive interferences that potentially render image quality non-diagnostic for clinical use. Therefore is work proposes novel multichannel antenna arrays to tackle this challenge. Arrays of 4, 8 and 16 channels and ultimately the worlds' first 32 channel antenna array for cardiovascular MRI at 7.0 T were implemented. Antenna arrays for cardiac UHF MRI as well as for musculoskeletal and ophthalmic UHF MRI are developed, characterized and successfully applied in pre-clinical studies. Electro-magnetic field simulations are utilized to study the capabilities of multi-channel RF antenna arrays to mitigate destructive interferences and provided the basis for a workflow towards homogenization of the electromagnetic radio-frequency field. Pre-clinical studies showed the capabilities and limits of translating the SNR gain of UHF MRI into clinical beneficial numbers, namely increased spatial or temporal resolution or scan time shortening. To make further use of the benefits of UHR MRI and to make a step towards first-hand spatial resolved information of biological processes in human tissue sodium imaging of the human heart was enabled with the design of a tailored antenna array. The results were reconstructed into the first movies of the human heart at 7.0 T based on sodium signal. The results of the presented pre-clinical studies for both proton and sodium imaging demonstrate the feasibility of multi-channel antenna arrays to overcome the challenges of UHF MRI. The modular approach of radio frequency antenna array design exhibits great flexibility for various clinical applications. Thus the presented results are a profound technological basis for radio frequency excitation and reception in UHF MRI and can be expected to pave the way for broader clinical studies at 7.0 T with the ultimate goal to improve the quality and the earliness of treatment decisions in future clinical practice.

Keywords: Biomedical Imaging, Magnetic Resonance Imaging, Ultrahigh Field MRI, local transmit- and receive antennas

List of abbreviations

μ	magnetic moment
γ	gyromagnetic ratio
$\hbar$	quantum angular momentum
k	Boltzmann constant
m	magnetic quantum number
B_0	static magnetic field
M_0	longitudinal magnetization of a sample when placed in a static magnetic field
ω_0	Larmor precession frequency
f_0	resonance frequency
B_1	RF magnetic field
B_1^-	left handed polarized RF magnetic field
B_1^+	right handed polarized RF magnetic field
t	time
T_1	relaxation time constant describing spin-lattice interactions
T_2	relaxation time constant describing spin-spin interactions
T_2^*	relaxation time constant taking into account susceptibility effects
TE	echo time
TR	repetition time
τ_{RF}	radio freuqency pulse duration
α	flip angle
s(t)	MRI signal in time domain
ϕ	MRI signal phase
C	capacitance
E	energy
G	gradient magnetic field
L	inductance
Q	quality factor
R	resistance
T	temperature
V	volume
X	reactance
Z	impedance
W_{RMS}	root mean square power

ADC	analog to digital converter
BMI	body mass index
CNR	contrast to noise ratio
DAC	digital to analog converter
MRI	magnetic resonance imaging
NMR	nuclear magnetic resonance
PCB	printed circuit board
ppm	parts per million
RF	radio frequency
ROI	region of interest
SAR	specific absorption rate
SNR	signal to noise ratio
Voxel	volume pixel

Table of content

1. Introduction

Magnetic resonance imaging (MRI) is an important imaging modality in nowadays healthcare as well as in fundamental biological and chemical research. The history of MRI starts with the description of the underlying effect of nuclear magnetic resonance (NMR) as early as 1938 by Rabi [1]. Lauterbur extended the technique by adding means to spatially resolve the NMR data in 1973 and reported on the first two dimensionally resolved MRI image [2]. Since then MRI widely spread into clinical routine and by 2008 more than 20.000 MR Scanners were installed worldwide with the number increasing rapidly [3]. For their contribution to the field of MRI Lauterbur and Mansfield were awarded the Nobel Prize in Physiology or Medicine in 2003. A fundamental advantage of MRI over computer tomography (CT) is the absence of ionizing radiation, making it the favorable imaging modality for the future and allowing for preventive checkups and repeated screenings of the course of diseases. Moreover MRI offers a wide range of image contrast options, supporting clear differentiation of soft tissues as well as the visualization of tissue function, namely perfusion, diffusion and blood oxygenation. This makes it especially valuable for tumor distinction, musculoskeletal imaging with an emphasis on the condition of cartilage and muscle and for cardiac imaging (CMR). For CMR the variety of applicable contrasts plays an important role for the diagnosis of coronary artery disease [4][5] and the assessment of myocardial viability [6].

1.1 Motivation

Driven by the inherent signal to noise (SNR) benefits of higher magnetic field strength, the magnetic field strength in clinical use has evolved from 1 Telsa (T) over 1.5 T to 3 T systems in recent years. As nowadays magnet technology expands the available magnetic field strength to B_0= 7 T and above, the research field of ultrahigh field MR (UHF-MR) became a steam engine for MR innovations. Between 2006 and 2011 the number of installed UHR MRI systems nearly doubled [7]. Some contrast mechanisms highly profit from the increased field strength and novel approaches using nuclei other than proton, historically suffering from low signal levels, become feasible in acceptable scan times. At 7.0 T the proton resonance frequency (f = 298 MHz) gradually starts to depart from the semi-static regime so that wave propagation effects strongly influence radio frequency (RF) field characteristics. The effective wavelength reaches the dimensions of the body and several concomitant effects bear the potential to spoil the SNR benefit. This includes the increasingly inhomogeneous RF field

distribution and increasing absorption of the RF by the human tissue. MR technology plays an important role to overcome these challenges and reach clinical applicability for UHF-MR.

At 7.0 T the working frequency of 297 MHz is in the range of radio and television broadcast. In radio communication RF antennas and arrays of multiple antennas are widely used and well characterized. In the field of MRI, moving from the near field coil-subject interaction at 1.5 T to wave propagation at UHF-MR, antennas become the appropriate mean for excitation and reception of the NMR signal. But unlike in communication technology in MR applications the antennas are used very close to the signal source and thus common far field assumptions are not valid. This leads to the need to re-investigate well-known antenna concepts for their new application in MRI.

1.2 State of the art radio frequency antenna arrays

Pioneering reports eloquently speak about RF antenna concepts, also called “RF coils” in the field of MRI, enabling CMR at 7.0 T [8, 9]. These RF antenna designs have been typically laid out as strip line elements on rigid or semi-flexible frames in conjunction with multi-channel transmit/receive (TX/RX) system architecture. Since multi-transmit MR systems are not widely available yet, comparatively simple cardiac coils have also been successfully used [10]. By 2010 several types of RF Coils for excitation and reception were under investigation for UHF MR. Loop antennas are widely used at intermediate magnetic field strength and thus serve as a solid ground for novel ultrahigh field designs. A cardiac-optimized 7.0 T transmit-receive configuration has employed four loop elements [11]. Due to a lack of available technology for the time being, ultrahigh fields MR systems for human imaging are not equipped with an embedded whole body RF resonator that is commonly used for RF transmission at lower and intermediate magnetic field strength. This leads to the need for dedicated transmit and receive technology for every application. Given the smaller region of interest as well as a strong interest in functional MRI, brain imaging was the first application for UHF MR and several RF coil arrays were designed for this purpose [12, 13, 14]. Body imaging is even more challenging, as the diameter of the body is larger than the wavelength and thus achieving a homogeneous excitation inside the whole body without destructive interferences is still subject of investigation. Initial results for cardiac imaging were presented for loop coils [11], as well as for strip line elements [9, 15] and transmission line elements [16].

1.3 Hypothesis and objectives

The clinical applicability of UHF MRI is closely connected with innovations in the field of RF technology. To the patient end of the MR system, the RF antenna or the RF antenna array has major impact on the achievable signal strength, signal homogeneity and acceleration capabilities of the MR acquisition. This technical numbers can be translated into increased spatial resolution, temporal resolution or acquisition time shortenings, summing up to enhanced image quality in the clinical workflow. Reaching the sub millimeter range in spatial resolution may remove common drawbacks of partial volume effects and allows for delineation of subtle anatomical details, as they are present for example in the cardiac anatomy, the human eye, in spine anatomy or the shoulder joint. To increase the number of transmit and receive channels is promising in several respects. Using a large number of elements in an array structure brings the signal-to-noise ratio (SNR) closer to the intrinsic maximum [17]. On the transmit side capabilities for multi-channel B_1^+ modulations may help to improve transmission field shaping and mitigate destructive interferences in the region of interest. On the receive side parallel imaging acceleration factors scale with the number of available receive channels [18]. Reduced scan time requirements would be particularly recognized in cardiac MRI, as the acquisition window is limited by the beating heart and the respiratory cycle or the breath hold time. Along with the intrinsic SNR gain of UHR-MR the use of non-proton nuclei (designated as x-nuclei) like sodium (^{23}Na) or fluorine (19F) for imaging is promising to provide new insights into physiological processes [19]. Thus the objective of this work is to design novel multi-channel radio frequency antenna arrays for proton and x-nuclei imaging at ultrahigh fields and demonstrate their clinical applicability and benefits.

2. Principles of magnetic resonance imaging

2.1 Nuclear magnetic resonance

Nuclear magnetic resonance (NMR) describes the phenomenon of absorption and re-emittance of electromagnetic radiation by nuclei inside of a magnetic field. Nuclei with an odd number of protons or neutrons exhibit a magnetic moment, in the MR community commonly referred to as spin that makes them suitable for NMR. For a nuclei with a spin quantum number of $m = \pm\frac{1}{2}$, like the ^{1}H nuclei most commonly used in MRI, there are two states with an energy given by (2-1). The higher the static magnetic Field B_0 the larger the difference between the energies of the two states ΔE (2-2). This leads to a slightly higher number of nuclei in the preferred lower energy state, resulting in a net magnetization of the macroscopic sample. The ratio of nuclei in the different states is in the order of parts per million (ppm). As the NMR signal is based on that marginal net magnetization it is the underlying driving force for the ongoing trend to raise the static magnetic field strength in NMR and MRI as far as technology allows.

$$E = -\gamma m \hbar B_0 \tag{2-1}$$

$$\Delta E = \gamma \hbar B_0 \tag{2-2}$$

Transitions from the lower to the higher energy level by absorption can be induced by application of electromagnetic radiation with a frequency matching the energy difference. In the following it is referred to as excitation. The frequency is given by the Larmor frequency (2-3). It is direct proportional to the static magnetic field and the proportionality constant is the gyromagnetic ratio γ that is constant for a given nuclei. Therefore the frequencies used in MRI are discrete values defined by the B_0 field strength and the used nuclei, see Table 1.

$$\omega = -\gamma B_0 \tag{2-3}$$

nuclei	γ [1/Ts]	f [MHz] @ 7.0T
^{1}H	26.75	298.02
^{23}Na	7.08	78.83

Table 1: *Gyromagnetic ratios and resonance frequencies for nuclei used in this work at a magnetic field strength of 7.0 T.* [20]

The reverse process to absorption is relaxation, which describes the magnetization returning into its equilibrium state by transmitting electromagnetic radiation of Larmor frequency. This radiation can be received by RF coils or antennas as the NMR signal. As the frequency, dictated by physics, is the same for excitation and reception, the radio frequency excitation coil or antenna is equally capable of signal reception. A comprehensive introduction to NMR physics can be found in [21].

2.1.1 Radio frequency excitation and reception

With the transition to a large number of spins the macroscopic result of the quantum physic effects can be described in a phenomenological way. The equilibrium magnetic moment $\overleftarrow{\mathrm{M}_0}$ of the sample is given by $\overleftarrow{\mathrm{M}_0} = \chi\overleftarrow{B_0}$, with χ denoting the magnetic susceptibility of the sample. The excitation of the equilibrium magnetic moment is done with radio frequency pulses transmitted by radio frequency coils or antennas adjusted to the resonance frequency given by the nuclei and the B_0 field strength. In Figure 1 the overall magnetic moment $\vec{M}$of the spins in a small volume is shown in a static magnetic field $\overrightarrow{B_0}$. With the force of a perpendicular excitation field $\overrightarrow{B_1^+}$ in the x-y plane $\vec{\mathrm{M}}$ gets tilted out of the z-direction and starts a precession around the direction of the $\overrightarrow{\mathrm{B}_0}$ field vector with Larmor frequency. The degree of excitation is given by the flip angle φ between $\overrightarrow{\mathrm{B}_0}$ and $\vec{M}$. To perpetuate the excitation the $\overrightarrow{B_1^+}$ field needs to be circular polarized with Larmor frequency to obtain a $\overrightarrow{B_1^+}$ that is perpendicular to $\vec{M}$ and $\overrightarrow{B_0}$ at any time. If the RF magnetic field is not ideally circular polarized, any RF field can be decomposed into a left and right hand circular polarized component, with the right hand polarized component B_1^+ being effective for excitation and the left hand polarized component B_1^- being effective for reception.

$$\overleftarrow{\mathrm{B}} = B_x\hat{x} + B_y\hat{y} + B_z\hat{z}$$

$$B_1^+ = \frac{B_x + \mathrm{j}B_y}{2} \qquad \textbf{(2-4)}$$

$$B_1^- = \frac{B_x - \mathrm{j}B_y}{2}$$

At clinical magnetic field strength a circular polarized field is commonly produced by a quadrature birdcage [22] RF coil design. To accomplish circular polarization at the higher resonance frequencies at UHF-MR for large regions of interest in the presence of interference effects is non-trivial and one major issue addressed in this thesis.

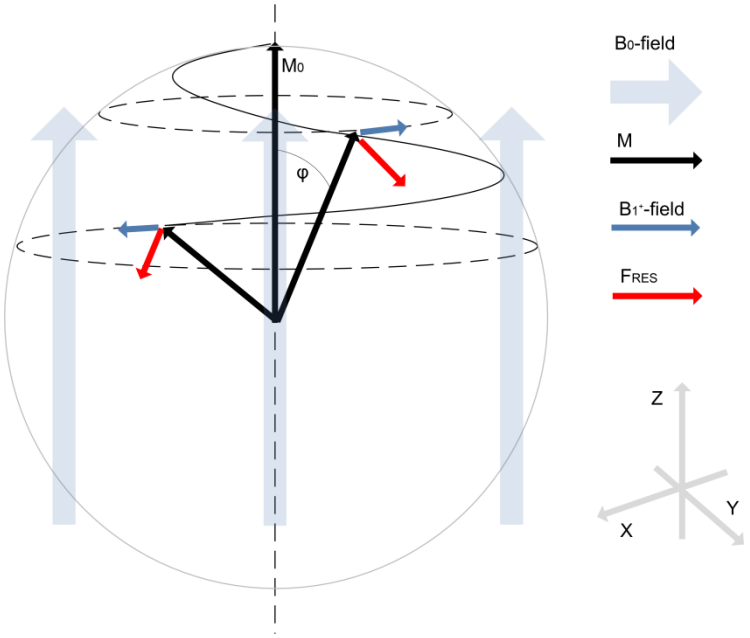

Figure 1: *Excitation of the magnetization vector by a circular polarized magnetic field* $\overrightarrow{\boldsymbol{B_1^+}}$. *A trajectory of an excitation process is depicted starting at the equilibrium magnetization* $\overrightarrow{\boldsymbol{M_0}}$ *with two exemplary states of* $\overrightarrow{\boldsymbol{B_1^+}}$, $\overrightarrow{\boldsymbol{M}}$ *and the resulting tilting force* $\overrightarrow{\boldsymbol{F_{res}}}$ *shown along the trajectory.*

2.1.2 Relaxation and Bloch equations

Relaxation to the equilibrium state is the result of two processes called spin-lattice relaxation and spin-spin relaxation. The spin-lattice relaxation describes the recovery of the magnetization into the longitudinal direction given by the static magnetic field and is characterized by the decay constant T_1. After the time T_1 the longitudinal magnetization regained $1 - \frac{1}{e}$ of its equilibrium value.

$$\mathrm{M}_z(\mathrm{t}) = \mathrm{M}_{z,0}(1 - e^{-t/T1}) \tag{2-5}$$

The spin-spin relaxation describes the decomposition of the excited transversal magnetization to its initial zero state. After $T_2$the transversal magnetization is decreased by factor $\frac{1}{e}$ of its maximum excited value.

$$\mathrm{M}_{x,y}(\mathrm{t}) = \mathrm{M}_{x,y,0}(e^{-t/T2}) \tag{2-6}$$

Felix Bloch introduced the equations (2-7) [23] that include both relaxation processes. They build the basis for the intuitive understanding of NMR und MRI and are commonly used to predict and simulate the spin relaxation process in the presents of tailored multidirectional, time varying magnetic fields.

$$\begin{aligned} \frac{\partial \mathrm{M}_x(\mathrm{t})}{\partial \mathrm{t}} &= \gamma(\mathrm{M}(\mathrm{t}) \times \mathrm{B}(\mathrm{t}))_x - \frac{\mathrm{M}_x(\mathrm{t})}{T_2} \\ \frac{\partial \mathrm{M}_y(\mathrm{t})}{\partial \mathrm{t}} &= \gamma(\mathrm{M}(\mathrm{t}) \times \mathrm{B}(\mathrm{t}))_y - \frac{\mathrm{M}_y(\mathrm{t})}{T_2} \\ \frac{\partial \mathrm{M}_z(\mathrm{t})}{\partial \mathrm{t}} &= \gamma(\mathrm{M}(\mathrm{t}) \times \mathrm{B}(\mathrm{t}))_z - \frac{\mathrm{M}_z(\mathrm{t}) - \mathrm{M}_0}{T_1} \end{aligned} \tag{2-7}$$

M(t) is the nuclear bulk magnetization of the sample as a function of time and B(t) is the overall magnetic field applied to the sample at the time t.

Additional dephasing of the transversal magnetization due to non-ideal magnetic field homogeneity, connected with equation (2-3), leads to the observation of a faster decay of the transversal magnetization, characterized by the time constant $T_2^* < T_2$. T_1, T_2 and T_2^* times vary with magnetic field strength and the sample material. Exploiting differences in T_1 and T_2^* times by reception of the NMR signal at a specific time slot during relaxation is a common way of generating contrast between different tissue types in MRI.

2.1.3 Signal and noise in a NMR experiment

The signal voltage induced in the RF coil directly after excitation of the magnetization M_0 into the transversal x-y plane can be expressed by equation (2-8) [24] with B_1^- denoting the left-hand polarized B-field on the RF coil, also called its receive sensitivity.

$$v_S = \sqrt{2}\omega M_{x,y,0} B_1^- \quad \textbf{(2-8)}$$

One inevitable noise source in every MR system is the thermal noise of the subject under investigation. The root mean square (RMS) voltage of a thermal noise source is given by equation (2-9) with the Boltzmann constant k_B, the subject's absolute temperature T, the receiver bandwidth Δf and the resistance of the subject R [24].

$$v_N = \sqrt{4 k_B T \Delta f R} \quad \textbf{(2-9)}$$

Substituting $\omega = -\gamma B_0$ and $M_0 = \chi B_0$ the intrinsic SNR = v_S/v_N might be expected to increase with the square of the B_0 field strength, but it is shown that the increase is significantly damped by the concurrent increase of the resistance R in the noise term at higher frequencies, resulting in a linear relation of SNR and B_0 [25]. The influence of sample volume V, the acquisition time T_{ac} and the receiver bandwidth BW on the SNR was studied in [24] and is given in equation (2-10). This proportionality can be used to balance SNR, spatial resolution and scan time within given technological and clinical boundary conditions.

$$\text{SNR} \propto V \sqrt{\frac{T_{ac}}{BW}} \quad \textbf{(2-10)}$$

2.2 Magnetic resonance imaging

Adding means of spatial selection for the received signal components leads from NMR to MRI. This is achieved by adding gradient coils to the main magnet that produce magnetic field gradients superimposed to the main magnetic field. This restricts the fulfilment of the resonance condition of equation (2-3) to a selected sub volume. In the following the magnetic fields necessary for an MRI experiment are introduced.

2.2.1 Static magnetic field

Clinical MR Systems are named by their static magnet field strength B_0, as this is a fixed parameter for a given system. For whole body human MR systems magnetic field strengths of 1T, 1.5T and 3T are clinically established and commonly achieved by superconducting coils. MR systems with magnetic field strengths of 7.0 T and above are called ultrahigh field

systems. Figure 2 depicts the magnetic field lines of a whole body magnet, which are aligned with the head-feet axis, commonly referred to as the z-axis.

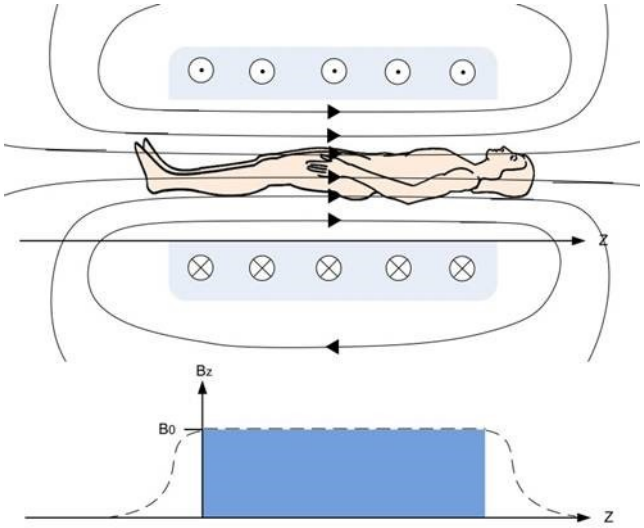

Figure 2: *Static magnetic field* $\mathbf{B_0}$ *of a whole-body MR system. In the middle of the bore, also called iso-center, the MRI imaging takes place.*

2.2.2 Spatial encoding gradients

To acquire 2D or 3D spatial resolved images gradient coils are inserted into the bore of the main magnet for all three directions of space. By adding gradient fields in the range of milli Tesla to the B_0 field the resonance condition becomes location dependent.

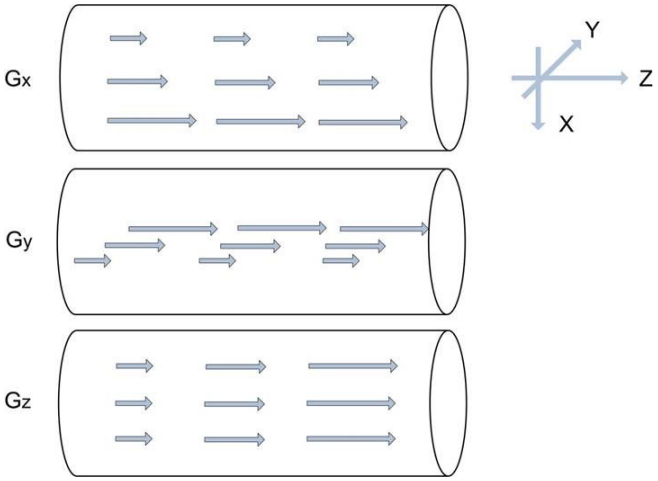

Figure 3: *Overstated depiction of the resulting main magnetic field in the presence of gradient fields in the three Cartesian coordinates.*

Considering a B field gradient exemplarily applied in z-direction during excitation leads to a slice selective excitation. The slice thickness depends on the gradient strength that translates in the bandwidth that allows for nuclear magnetic resonance.

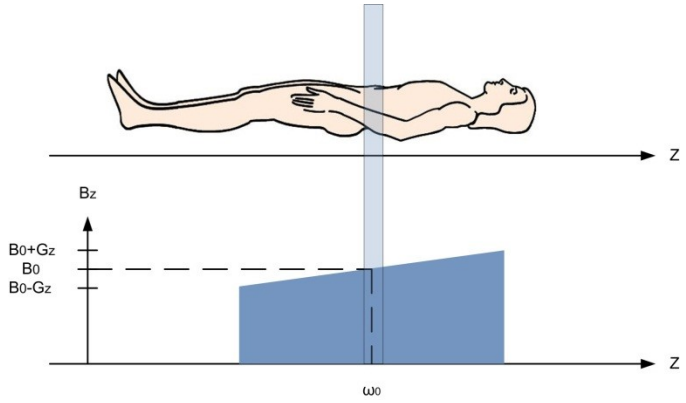

Figure 4: *Slice selection gradient in z-direction. The application of a gradient restricts the fulfillment of the resonance condition to a slice of given thickness defined by the gradient strength.*

During reception a so called readout gradient perpendicular to the slice selective gradient allows for frequency encoding in one direction. With the dependence $\omega = \frac{\partial \varphi}{\partial t}$ a frequency deviation induced by the gradient translates into a different phase accrual at the locations along the frequency encoding direction. Applying the Fourier transformation to the received frequency spectrum leads to a spatial resolved image in the frequency encoding direction. Yet the third direction cannot be resolved in a single acquisition. Applying a set of varying phase encoding gradients over a set of acquisitions phase information becomes available along the stacked measurements. Thus a two dimensional Fourier transform lead to a spatial resolved image in both directions.

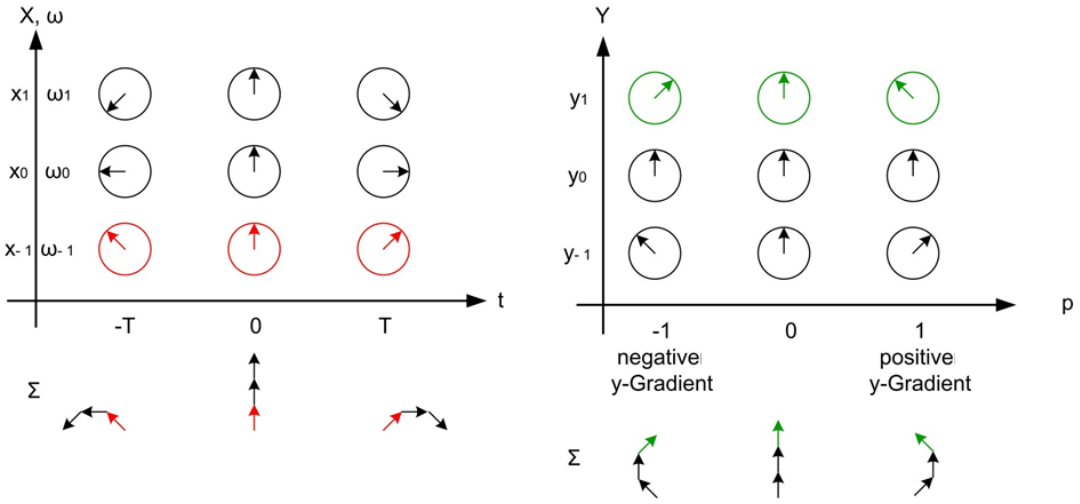

Figure 5: *Influence of the frequency and phase encoding gradients on the phase of the spins. In the frequency encoding case on the left the vertical axis shows three spins along the frequency encoding direction x and their phases over time t on the horizontal axis. On the right three spins along the phase encoding direction y and their phases over iterative measurements p is depicted. The only signal accessible by reception is the sum Σ in phase and amplitude.*

2.2.3 MR imaging techniques

A specific pattern of spatial encoding gradients, RF pulses and signal reception windows is called imaging sequence. A parameter set that defines the variables of the underlying sequence is called imaging protocol. There are several imaging techniques available serving different clinical applications and offering specific contrasts [26–29]. To introduce the basic principle a 2D spin echo sequence diagram [26] is shown in Figure 6. During the application of a 90° RF pulse a slice selective gradient limits the excitation to a specific slice. In the following the frequency-encoding gradients lead to de-phasing of the spins linked to their spatial position along the frequency-encoding direction. After half of the chosen time echo time (TE) a 180° pulse inverts the direction of the magnetization and thus the direction of de-phasing, generating an in phase state of the majority of the spins, called echo, after TE. Around TE the analog-to-digital converter (ADC) is activated and receives the echo with a specific frequency spectrum. Iterative measurements with alternation of the phase-encoding gradient generate the spatial information along the phase-encoding direction over the stack of measurements. Figure 7 shows an exemplary cardiac MR scan being calculated by 2D-FFT from the raw data.

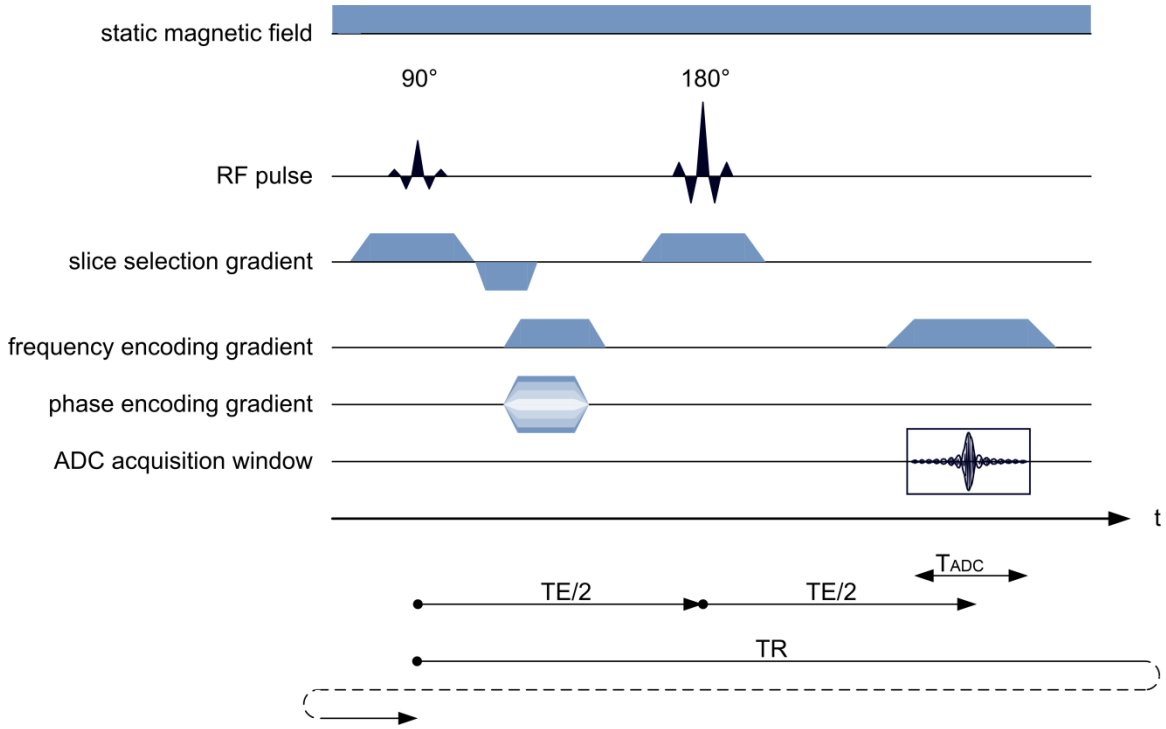

Figure 6: *Sequence of gradients and RF pulses to acquire a spin echo image. Depending on the size of the desired matrix this pattern has to be repeated for the number of pixels in the phase encoding direction.*

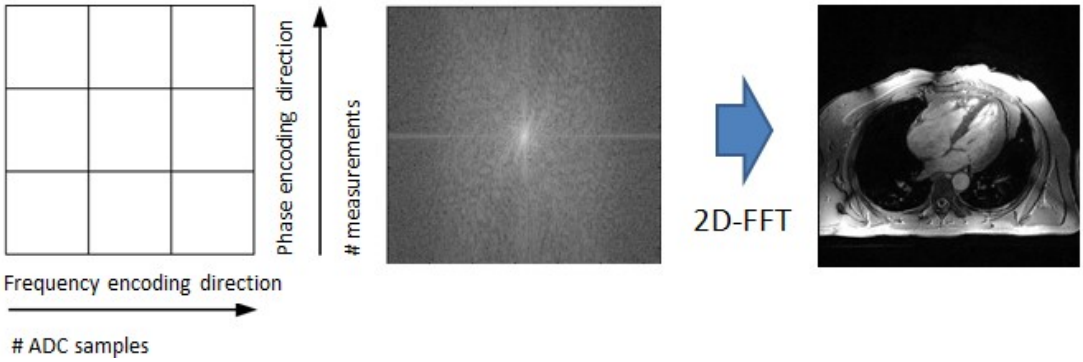

Figure 7: *On the right the structure of a raw data matrix of a MR scan is depicted. The number of lines in the first matrix dimension is given by the number of acquired ADC samples. The second dimension is given by the number of acquired phase encoding steps. In the middle exemplary data is shown. On the left the result is shown in the image domain after a two-dimensional Fourier transformation (2D-FFT).*

2.2.4 Parallel imaging and geometry factor

Acquisition of the raw data consumes considerable time dependent of the number of phase encoding samples and presents one major drawback of MRI. Several techniques were introduced to accelerate the image acquisition [18, 30–32]. Among them the methods of sensitivity encoding (SENSE) and Generalized Auto calibrating Partially Parallel Acquisitions (GRAPPA) are the most commonly used. These methods are based on under sampling in the

phase encoding direction with respect to the Nyquist-Shannon theorem [33]. The Nyquist-Shannon theorem states that the highest frequency occurring in the signal must be less than half of the sampling rate to allow for perfect reconstruction of the signal waveform from the sampled data points. In an under sampled dataset signal parts with higher frequency are falsely overlapped with signal components of half of their frequency. Image wise this results in folding artefacts. The additional data acquired with multiple coils in parallel can be utilized to correctly differentiate between this two signal components and remove the folding artefacts. For SENSE the basic idea is introduced in Figure 8. Todays' MR systems typically offer up to 32 independent receive channels.

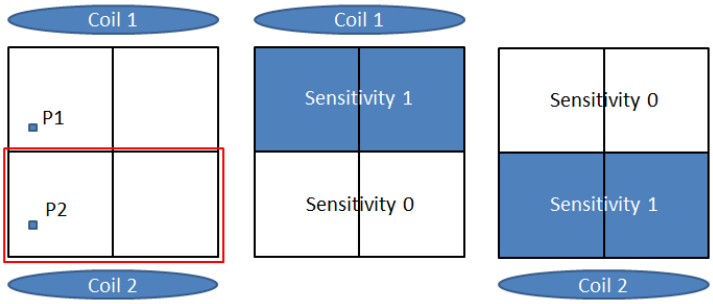

Figure 8: *SENSE reconstruction in the ideal case with orthogonal coil sensitivity profiles and in the absence of noise. A twofold accelerated image acquisition will result in the image data be folded into the reduced FOV depicted in red, with the image points P1 and P2 represented by the same pixel. The two datasets of the reduced FOV of the individual coils acquired in parallel weighted with the corresponding sensitivity profile of the coil elements allows for reconstruction of the unimpaired complete image. The theoretical upper bound for the acceleration factor is equal to the number of independent coil elements.*

One metric to evaluate the parallel imaging performance of multi-channel coil arrays is the geometry factor g. The degraded SNR_{deg} of a reconstructed under sampled dataset is given by equation (2-11) depending on the factor of under sampling R and the g factor. In case of orthogonal coil sensitivities the g factor is close to 1, thus the SNR is degraded solely by the square root of the factor of under sampling. If the coil sensitivities at overlapping pixels are similar the sensitivity encoding of the aliased pixels becomes inaccurate and introduces additional noise, characterized by an increasing g-factor.

$$\mathrm{SNR}_{deg} = \frac{\mathrm{SNR}_{full}}{g\sqrt{R}} \qquad \textbf{(2-11)}$$

3. Materials and methods

3.1 Basic radio frequency methodology

Excitation and reception of the MRI signal is accomplished with dedicated radio frequency technology. As the wavelength reaches the dimensions of the structures, wave propagation has to be taken into account. At 7.0 T the proton resonance frequency is 297 MHz. This frequency translates into a wavelength of approximately 13 cm in the human body and thus the physical models devised in the field of radio frequency technology apply. The essential model for the relation between time-varying currents, voltages, electrical and magnetic fields is given by the Maxwell equations [34]. Comprehensive explanations of RF technology can be found in [35,36]. In the following the most relevant basics for RF designs reported in this work are introduced.

3.1.1 Electromagnetic induction

For reception of the resulting magnetic moment of the sample or the subject as described in 2.1.1 the effect of electromagnetic induction in RF coils or antennas is used. The Maxwell-Faraday equation (3-1) respectively its integral form (3-2) connects the induced voltage V_{ind} in a closed conductor *c* in the presence of a time-varying magnetic field $\vec{B}$ perpendicular to the area A circumferenced by the conductor. The scalar product * connotes that only $\vec{B}$ field changes along the normal vector $\vec{A}$ contribute to the induced voltage.

$$\mathrm{rot}\,\vec{E} = -\frac{\partial \vec{B}}{\partial t} \tag{3-1}$$

$$V_{ind}(t) = \oint_c \vec{E}(t) * d\vec{r} = -\int_A \frac{\partial \vec{B}(t)}{\partial t} * d\vec{A} \tag{3-2}$$

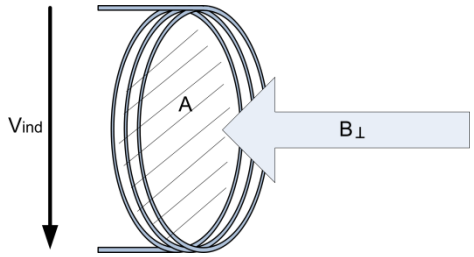

Figure 9: *Induced signal in a loop coil by a time varying orthogonal magnetic field penetration through the cross section of the conductor.*

3.1.2 Resonant circuits

An inductivity (L) and capacity (C) together with their parasitic resistances (R) are building a RLC resonant circuit. Resonant systems oscillate with an superelevated amplitude when excited at their resonance frequency. For the purpose of RF transmission and reception in MR this effect is facilitated to increase the transmission field strength and the receiver signal amplitude. A circuit diagram of a serial RLC circuit is shown in Figure 10. At the resonance frequency the imaginary part of the input impedance given in (3-3) decays to zero. This leads to the formula of the resonance frequency in (3-4). Regarding MR coils L is typically given by the geometry of the coil layout, R is the result of the losses of the coil geometry and the capacitors and C is adjusted to meet the desired resonance frequency.

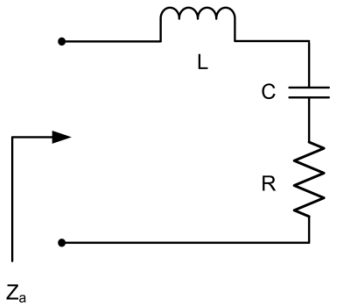

Figure 10: *RLC resonant circuit and real and imaginary part of the input impedance Z_a.*

$$Z_a = R + i\omega L + \frac{1}{i\omega C} \quad \textbf{(3-3)}$$

$$\omega_0 = \frac{1}{\sqrt{LC}} \quad \textbf{(3-4)}$$

3.1.3 Tuning and impedance matching

Tuning refers to the adjustment of the resonance frequency while impedance matching refers to the adjustment of input impedance of the circuit to match the characteristic impedance Z_0. The characteristic impedance for most RF systems serves as an industry standard and was historically chosen to $Z_0 = 50\,\Omega$ to balance voltages and currents in the radio frequency range. Interconnecting RF hardware with identical characteristic impedance leads to zero reflections at the interfaces in the ideal case. Therefor RF hardware of the MR system as well as custom built technology presented in this work is designed to match this value. A basic but common tune and match network is presented in Figure 11.

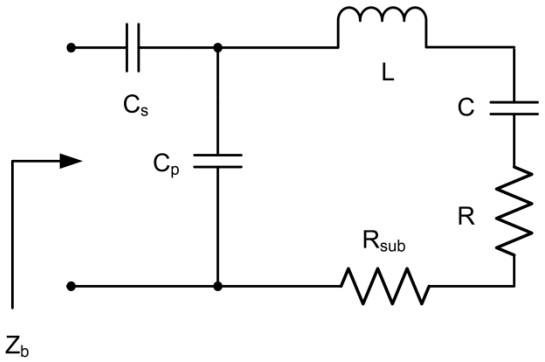

Figure 11: *RLC resonant circuit including a tuning capacitor C_p and a matching capacitor C_s. R is divided into R_{coil} and $R_{subject}$ to include both main loss mechanisms in MR RF coils. Z_b represents to input impedance of the complete circuit that should match Z_0 to avoid reflections of the applied RF signal.*

$$\mathrm{Z}_b(\omega_0) = \frac{\alpha + j\beta - j\omega_0 C_p(\alpha^2 + \beta^2)}{(\omega_0 C_p \alpha)^2 + (\omega_0 C_p \beta - 1)^2} + \frac{1}{j\omega_0 C_s} \tag{3-5}$$

Based on the measured or simulated value of the complex impedance at the feeding point $\mathrm{Z}_a(\omega_0) = \alpha + j\beta$ and the circuit diagram in Figure 11 the input impedance $\mathrm{Z}_b$can be derived (3-13). With the impedance and resonance condition $\mathrm{Z}_b(\omega_0) = \mathrm{Z}_0 = 50 + j0\ \Omega$ an analytical solution for the appropriate values for the tuning (3-14) and matching (3-15) capacitors can be calculated to reduce manual adjustment time.

$$C_p = \frac{2\omega_0\beta \pm \sqrt{(2\omega_0\beta)^2 - 4({\omega_0}^2\alpha^2 + {\omega_0}^2\beta^2)(1 - \frac{\alpha}{50})}}{2({\omega_0}^2\alpha^2 + {\omega_0}^2\beta^2)} \tag{3-6}$$

$$C_s = \frac{(\omega_0 C_p \alpha)^2 + (\omega_0 C_p \beta - 1)^2}{\omega_0\beta - {\omega_0}^2 C_p(\alpha^2 + \beta^2)} \tag{3-7}$$

3.1.4 Quality factor and quality-factor ratio

The quality factor (Q-factor) is a measure for the bandwidth of the resonance as well as for the superevelation of the amplitude. It is defined by 2π the ratio between the stored energy in the system and the dissipated energy per cycle. The bandwidth of the resonance is indirect proportional to the Q-factor and assuming low damping as common in RF coil and antenna design the amplitude at the resonance frequency V_{res} is approximately Q times the amplitude of the static excitation V_{stat}.

$$\mathrm{Q} = 2\pi \frac{\text{stored energy}}{dissipated\ energy\ per\ cycle} = \frac{\omega_{res}}{2\Delta\omega} \approx \frac{V_{res}}{V_{stat}} \tag{3-8}$$

Also the lossy behavior of each lumped reactive components as part of a resonance circuit can be characterized by its Q factor, in that case defined as the ratio of reactance over resistance, and be combined to the overall Q (3-12) [37].

$$\mathrm{Q}_L = \frac{\omega_0 L}{R_L} \qquad \mathrm{Q}_C = \frac{1}{\omega_0 C R_C} \qquad \mathrm{Q} = \frac{1}{\frac{1}{\mathrm{Q}_L} + \frac{1}{\mathrm{Q}_C}} \tag{3-9}$$

The ratio of the Q factor of the resonance circuit measured in free air and its value measured in the presence of the subject is used to indicate the coil quality. A high $\mathrm{Q}_U/\mathrm{Q}_L$ ratio indicates that most of the RF power is deposited in the subject under investigation as intended and not in the RF coil itself. A setup with coil losses equal to subject losses would result in a $\mathrm{Q}_U/\mathrm{Q}_L$ ratio of 2.

$$\frac{\mathrm{Q}_{unloaded}}{\mathrm{Q}_{loaded}} = \frac{\mathrm{R}_{subject} + \mathrm{R}_{coil}}{\mathrm{R}_{coil}} \tag{3-10}$$

As power deposition in the coil contributes to noise, while not leading to additional excitation, the SNR degradation can be estimated by equation (3-11) [38].

$$\mathrm{SNR} = \mathrm{SNR}_{intrinsic} \sqrt{1 - \frac{\mathrm{Q}_{unloaded}}{\mathrm{Q}_{loaded}}} \tag{3-11}$$

3.1.5 Balancing and sheath wave suppression

Most antennas are symmetrical structures without a defined ground. In opposition coaxial cables, commonly used to feed the signal to the antenna, have a grounded outer conductor and a signal routing inner conductor. That way the EM fields are encapsulated inside the coaxial cable and the RF signal has low interferences with surrounding parts and neighboring coaxial cables. To uphold this feature the signal to and from the antenna needs to be transformed with a balun (balanced-unbalanced transformer) or a sheath wave trap. This practically means preventing or damping the signal travelling on the outer conductor. A cheap and broadband solution is to wind the coaxial cable around a toroidal ferrite, but this is not feasible inside the magnetic field due to the ferromagnetism of the ferrite. A MR compatible solution is to use a parallel resonant circuit as a trap circuit. Theoretical the impedance of a parallel resonant circuit is infinity at its resonance frequency, preventing the signal to travel on the outer conductor. Figure 12 exemplarily shows the design used for the 32-channel cardiac array.

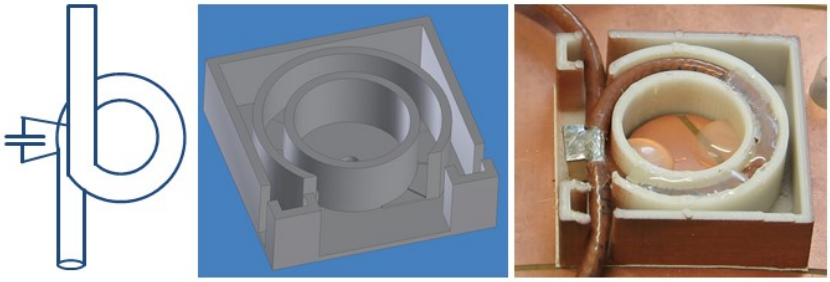

Figure 12: *Parallel resonant trap circuit to suppress sheath waves. The coaxial cable itself forms the inductor. Together with a chip capacitor it is tuned to the desired trap frequency.*

The positioning of cable traps exhibits some pitfalls. Generally it should be placed directly at the antenna to prevent the sheath waves at the origin. But the parallel resonant circuit design is prone to coupling to the antenna, as both elements are resonating at the same frequency. Thus the loop of the cable trap has to be shielded against the field of the antenna. On the other hand the part of the coaxial cable between antenna and cable trap needs to be electrically significantly shorter than $\frac{\lambda}{4}$ not to act as a resonating structure itself and leading to unpredictable resonance behavior of the antenna.

3.1.6 Radio frequency fields in human tissue

RF fields are highly dependent on the surrounding media i.e. experience variations when penetrating human tissue. Firstly the wavelength of RF fields is dependent on the permittivity ε and the permeability μ of the surrounding space (3-12). In free space $\mu_r = \varepsilon_r = 1$. With respect to field perturbations the influence of permeability can be neglected. In the microscopic scale permeability differences are used as a MR contrast mechanism, but as permeability is a measure for the magnetization a material obtains in the presence of an external magnetic field high permeability materials are not used in MR environments [39]. Nevertheless ε values can vary significantly.

$$\lambda = \frac{c_0}{f}\frac{1}{\sqrt{\mu_r \varepsilon_r}} \qquad \textbf{(3-12)}$$

At 7.0 T the proton resonance frequency is 297 MHz. This frequency exemplarily translates into a wavelength of approximately 13 cm in human heart. Secondly the absorption of RF fields is dependent on the conductivity. This affects the resulting penetration depth as well as tissue heating due to excessive RF absorption. Table 2 summarizes the material parameters for exemplary tissue types and the frequencies used in this work.

tissue	rel. permeability @ 297MHz	conductivity [S/m] @ 297MHz	rel. permeability @ 78MHz	conductivity [S/m] @ 78MHz
Bone	13.45	0.08	15.99	0.06
Muscle	58.24	0.77	69.13	0.70
cartilage	46.83	0.55	59.39	0.46
Fat	5.63	0.04	6.28	0.04
Blood	65.71	1.32	81.60	1.22

Table 2: *RF characteristics of selected human tissues at 297 MHz and 78 MHz* [40]*, corresponding to the resonance frequencies of proton and sodium imaging at 7.0 T.*

3.1.7 Radio frequency characterization and scattering parameters

Characterization of RF hardware is based on reflection and transmission measurements of RF voltage waves, as voltages and currents become time and space dependent. A set of n x n complex scattering parameters (S-Parameter) describes the RF characteristic of any given n-

port network. For a two-port network the definition is given in equation (3-13), (3-14) together with Figure 13.

$$S_{1,1} = \frac{a_1}{b_1}|_{a_2=0} \qquad S_{2,2} = \frac{a_2}{b_2}|_{a_1=0} \tag{3-13}$$

$$S_{2,1} = \frac{b_2}{a_1}|_{a_2=0} \qquad S_{1,2} = \frac{b_1}{a_2}|_{a_1=0} \tag{3-14}$$

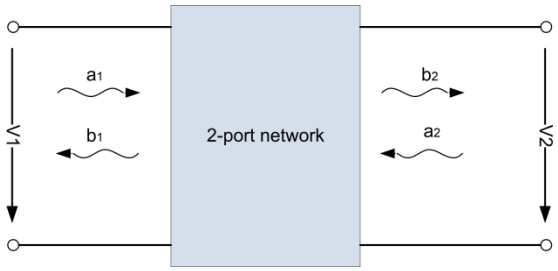

Figure 13: *Scattering parameter of a two-port network with incident voltage waves* $\boldsymbol{a_n}$ *and reflected voltage waves* $\boldsymbol{b_n}$ *.* $\boldsymbol{S_{1,1}}$ *is called input reflection parameter,* $\boldsymbol{S_{2,2}}$ *output reflection parameter,* $\boldsymbol{S_{2,1}}$ *forward transmission parameter and* $\boldsymbol{S_{1,2}}$ *reverse transmission parameter.*

The connection between voltage and current waves is given by the characteristic impedance $Z_0 = 50\,\Omega$.. S-Parameter are typically measured and given in dB scale.

$$S_{i,j\ dB} = 20\log\left(S_{i,j\ linear}\right) \qquad S_{i,j\ linear} = 10^{\frac{S_{i,j\ dB}}{20}} \tag{3-15}$$

With the use of a vector network analyzer the S-Parameters are determined automatically for chosen sampling points in a given frequency range. Throughout this work an eight channel vector network analyzer (ZVT 8; Rohde & Schwarz, Memmingen, Germany) was used which allows to simultaneously acquire a 8x8 S-Parameter Matrix. For the arrays of 16 and 32 elements iterative measurements were conducted to acquire the 16x16 and 32x32 S-Parameter matrices. Matching and tuning of an antenna array is characterized by its $S_{n,n}$values at the desired frequency. A value of $S_{1,1} = -20dB$ corresponds to 10% reflection of the incident voltage wave. This translates into a power reflection of 1%. The transmission coefficients $S_{m,n}$ characterize the coupling between the antennas. In passive circuits the reciprocity $S_{2,1} = S_{1,2}$ applies. Therefor the upper or lower triangular S-Parameter matrix fully characterizes a passive network like an antenna array.

3.2 Human ultrahigh field magnetic resonance system

In-vivo imaging of humans in an investigational UHF MR environment is subject to numerous boundary conditions ranging from technological availability over comprehensive patient safety evaluation to regulatory norms and ethic approvals. In the following these are summarized for the in-vivo studies presented in this work, followed by the promises and challenges of UHF MR for selected clinical applications tackled in this work.

3.2.1 The whole body human MR System

MR experiments were conducted on a 7.0 T whole body system (Magnetom, Siemens Healthcare, Erlangen, Germany). The open bore diameter was 60 cm with a length of 3 m. The system was equipped with an Avanto gradient system (Siemens Healthcare, Erlangen, Germany). The maximum slew rate was 200 mT/m/ms, the maximum gradient strength 45 mT/m. The system offered 32 independent receive channels. A single channel RF amplifier with a peak power of 8 kW at 297 MHz was used for ^{1}H imaging (Stolberg HF-Technik AG, Stolberg-Vicht, Germany). A single channel RF amplifier with a peak power of 1 kW at 78.9 MHz was used for ^{23}Na imaging (Stolberg HF-Technik AG, Stolberg-Vicht, Germany). A acoustic cardiac triggering device [41] (Easy Act, MRI.TOOLS GmbH, Berlin, Germany) was used for cardiac triggered imaging.

3.2.2 Radio frequency pathways of an MR system

On the MR system side the transmit path consists of a pulse generator, a digital-to-analog converter (DAC) and a power amplifier. For x-nuclei imaging further transmitters are needed to provide the corresponding frequencies. Each receive path comprises an amplifier and an analog-to-digital converter (ADC) [42]. A vendor defined RF coil interface makes all this paths available for a wide range of RF coils tailored for the different applications in clinical MRI and novel RF coil technology investigated in this work. The RF coil section of a transmit and receive RF coil typically consists of the coil or antenna elements itself and transmit-receive switches plus preamplifiers for every channel, as this parts need to be in close vicinity to the coil elements and adjusted to the resonance frequency of the desired nuclei.

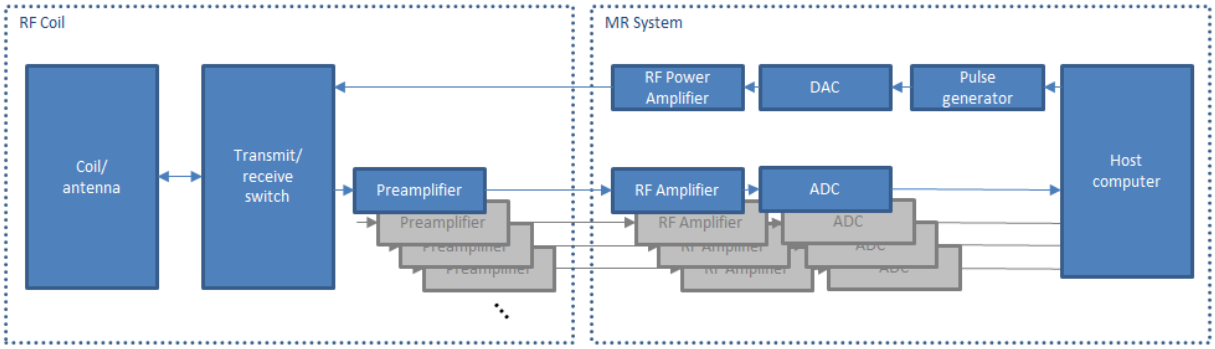

Figure 14: *Block diagram of the main parts of the RF chain of a MR system.*

To achieve a high signal to noise ratio, noise reduction is as important as signal enhancement. Therefore a low noise design of the parts in the RF receive pathway as well as the correct placing and order of the hardware between the RF elements and the MR system is crucial. Additional to the thermal noise of the subject under investigation the thermal noise of the coil resistance adds to the total noise. Unlike the body noise the coil noise contribution can be reduced by minimizing the resistance and reducing the temperature of the coil. Low ESR (equivalent series resistance) type capacitors (i.e. American Technical Ceramics Inc., Huntington Station, NY) are typically used together with a sufficient conductor cross section to reduce the resistance. For small RF coils cryogenic cooling is reported to increase the SNR significantly [43, 44]. For larger coils or antenna arrays for human MR applications this technology is currently not available. The noise behavior of a RF component can be characterized by the noise factor (F). It is defined as $F = \frac{SNR_{in}}{SNR_{out}}$. For a RF system of cascaded parts the overall noise figure is calculated by the Friis' formula [45], Eq (3-16).

$$F_{system} = F_1 + \frac{F_2 - 1}{G_1} + \frac{F_3 - 1}{G_1 G_2} + \cdots + \frac{F_n - 1}{G_1 G_2 .. G_{n-1}} \qquad \textbf{(3-16)}$$

F_n denotes the noise factor of the n-th stage and G_{n-1}denotes the linear power gain of the n-th stage . The noise factor of the system is therefore dominated by the parts in the early stages of amplification, as the influence of the subsequent parts is reduced by the gain the in the denominator. Therefore the main efforts are put into a low noise RF coil and a low noise preamplifier (LNA). To prevent additional noise as well as pick up of interferences before the LNA, the preamplifier is not part of the main MR system, but part of the RF coil as it is usually placed in close vicinity to the coil elements. Adding the noise figure to equation (2-10) leads to equation (3-17).

$$\mathrm{SNR} \propto \frac{V}{F}\sqrt{\frac{\mathrm{N}}{BW}} \tag{3-17}$$

3.2.3 Radio frequency coil interface

To connect the custom built hardware of RF coils and antennas to the commercial MRI system the common parts of all RF arrays presented in this work, namely the plugs to the commercial system, the preamplifiers and the transmit/receive switches were incorporated into multi-purpose interface boxes. While this approach arguably inserts additional connectors and cable length, especially in the sensitive part between the coil elements and the preamplifiers as emphasized in the previous section, it enables the research of a wide variety of design within a rational resource and time budget. Four identical eight channel interfaces were realized, offering connections for a maximum of 32 elements. TX/RX switches and low-noise preamplifiers were purchased from Stark Contrasts, Erlangen, Germany.

Another RF circuitry that is used with all presented RF arrays are RF power splitters to split the power of the single transmit output of the MR system into the number of transmit channels. Therefore a set of ten 1:4 power splitters and one 1:2 power splitter in lumped element Wilkinson design were realized. The Wilkinson power splitter relies on impedance transformation of n outputs to a single input, either by quarter wave impedance transformation or by its lumped element equivalent. The parallel combination of n branches need to be equal the characteristic impedance $Z_0 = 50\,\Omega$, thus each branch needs to exhibit an input impedance of nZ_0. The equation describing the impedance transformation of an quarter wave transformer is $\frac{Z_{in}}{Z_T} = \frac{Z_T}{Z_L}$. The characteristic impedance of the quarter wave transformers is therefor given by $Z_T = \sqrt{n}Z_0$. The equivalent lumped element values can be calculated by $Z_T = \omega_0 L = \frac{\omega_0}{C}$.

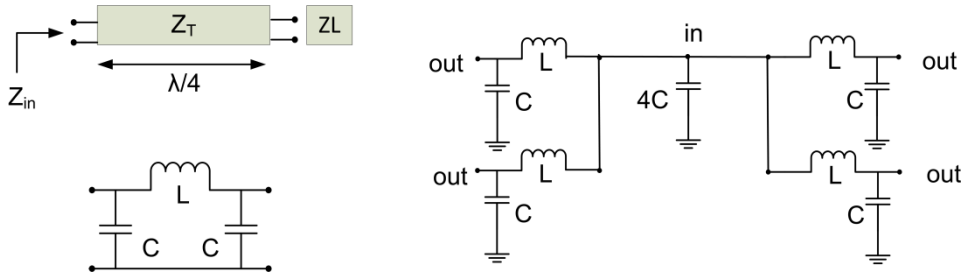

Figure 15: *Design of RF power splitters based on quarter wave transformers. In the upper left a transmission line of length* $\frac{\lambda}{4}$ *and characteristic impedance* $\mathbf{Z_T}$ *is shown. To meet space restrictions the equivalent circuit shown in the lower left is used for the practical realization. An exemplary composition of a 1:4 power splitter is shown on the right. The capacitors in the center can be combined into one lumped element, leading to the setup that was used for all power splitters realized in this work.*

3.3 Development of transceiver arrays for ultrahigh field MRI

Excitation (transmission, TX) and reception (RX) of the MRI signal is accomplished with dedicated radio frequency technology called RF coils or RF antennas. At 7.0 T the proton resonance frequency is 297 MHz and thus in the range of radio and television communication. The term RF coil implies a near field interaction with the subject while the term RF antenna implies wave propagation. Moving from clinical magnetic field strength to ultrahigh fields 7 Tesla is right at the transition of both regimes [46] and hence both terms are used equivalently hereinafter. As the frequency is the same for RX and TX an antenna that is used for both is called transceiver. “A group of antennas in which the relative phases of the respective signals feeding the antennas are varied in such a way that the effective radiation pattern of the array is reinforced in a desired direction and suppressed in undesired directions” is called phased array [47]. Although the term phased array was defined in communication technology regarding the shaping of the radiation pattern, thus the far field, this term is commonly used in MRI to describe arrays of coils or antennas to shape the resulting (near) field inside the subject.

3.3.1 Antenna design concepts

While loop coils are a accepted standard at clinical magnetic field strength, the investigation of an ever broadening spectrum of antenna concepts for ultrahigh field MRI is ongoing since UHF MRI Systems became available for research purposes. The concept of a loop antenna is to form a resonant circuit with a closed conductor loop and tune it to the desired resonance frequency by intermediate capacitors. The use of an RF shield is optional. The loop size and

shape is variable in a wide range. Dipole antennas are the most basic and commonly used antennas in communications technology. They consist of two symmetrical conducting legs. The length of the legs is given by the resonance frequency and strongly dependent on the surrounding media. For MRI applications at 7T the length of a half-wave dipole in free space is 0.5 m. This length is not suitable for most application in MRI and thus the surrounding media as well as meander structures and a capacitor at the feeding point can be facilitated to shorten the length. Another design parameter is the bandwidth (BW) of the dipole. It is dependent on the shape of the legs and bow-tie shaped dipoles are renowned for their larger BW [48] compared to rod-shaped dipoles. The largest BW for triangular legs was reported for an angle of 90° at the feeding point [49]. A third type of antennas used in MRI are stripline antennas. They are formed by a dipole antenna etched on one side of a PCB (printed circuit board) and a solid ground plane on the other side of the PCB. The length of the stripline antenna is given by the desired frequency. It can be shortened by end-capacitors, meander structures or a capacitor at the feeding point.

3.3.2 Antenna arrays in MRI

It was shown that signal voids in UHR MRI acquisitions can result from both transmit- and receive sensitivity profiles, even for a single element [50]. While in the transmit case adequate B_1^+shimming needs to be performed to avoid signal voids in the overall transmit field, in the receive case a sum-of-squares combination of multiple receive elements suppresses the influence of signal voids in single channels for the combined image. There are three main driving forces to use RF coil arrays in MRI. The first one is a gain in SNR when adapting the region of optimal SNR with the field of view of the antenna or loop coil, as introduced by [51]. For a loop element the region of optimal SNR is approximately in a depth of one loop diameter. As the body noise is proportional to the amount of tissue in the field of view of the antenna, large antennas or coil elements lead to increased reception of noise. This holds true as long as the main noise contribution originates from the sample while the additional coil elements add minor additional noise. This limits the size reduction of loop elements, compare Figure 41 in the results section 4.5.1. Furthermore the cross talk between the individual elements of the array needs to be small to avoid correlated noise reception [52]. During image composition the signals from several independent RF antennas sum up, while uncorrelated sample noise components diminishes. Both conditions were carefully evaluated during the design of RF arrays by measuring the Q-factor ratio as well as the noise correlation matrix. In the pioneering publication concerning receive RF arrays a 2.6 fold improvement of SNR in a

depth of 8 cm for a 30 cm long region of interest is reported when moving from a single 30x15 cm³ loop coil to a linear array of four 8 x 8 cm² loops [51]. The second reason for the use of receive arrays is to support parallel imaging techniques, as introduced in chapter 2.2.4. The applicable acceleration factor increases with the number of independent receive elements. The third reason for the use of antenna arrays are field inhomogeneities that arise at high field and ultrahigh field MRI with the wavelength of the RF signals reaching the dimension of the region of interest. A large number of independent transmit elements offers the degrees of freedom necessary to shape the resulting overall transmission field in a beneficial manner for the intended application.

3.3.3 Transmission field mapping

Transmission field (B_1^+) mapping is a imaging technique to measure the excitation field strength B_1^+ inside a phantom or a subject for a specific RF coil setup and by means of dedicated MRI sequences. Knowledge of the transmission field is vital for combining multiple independent channels to a beneficial overall field as well for validation of EM simulations. For the latter purpose absolute B_1^+ mapping was conducted using a Bloch-Siegert implementation [53]. The presence of an RF field with a frequency ω_{off} of some kHz off the nominal resonance frequency causes a change in the spins resonance frequency while not causing spin excitation. This effect is called Bloch-Siegert shift [54]. Applying an off-resonance RF pulse of duration T after the excitation and refocusing pulse will lead to a phase accrual dependent on the B_1^+ field strength.

$$\phi_{BS} = \int_0^T \frac{(\gamma\, B_1^+(t))^2}{2\omega_{off}(t)}\, dt \qquad \textbf{(3-18)}$$

Knowing the applied energy the phase images with different off-resonance frequencies can be post processed to an absolute B_1^+ map. As the Bloch-Siegert method also captures phases introduced by non-uniformities of the static magnetic field (B_0) B_0 mapping [55] was used to compensate for this error.

3.3.4 Transmission field shaping

Transmission field homogeneity and efficiency are major obstacles on the way of UHF MRI to clinical applications. Recognizing that in the early stages of UHR MRI [8, 9] numerous techniques and workflows were proposed and evaluated to overcome this issues [56–59]. All methods have in common that they rely on RF coils with multiple independent transmit

elements. The individual transmit fields of the elements are then composed to the resulting excitation field. Equation (3-19) describes the summation over the number of coil elements nc of the individual $B_{1,c}^{+}$ fields at the position $\vec{r}$ weighted by the complex transmit setting $x_c = \widehat{x_c} e^{i\theta}$ chosen for each coil element. For a discretized model of voxels the spatial position $\vec{r}$ can be substituted by the voxel number p of a total number of voxels np.

$$B_1^+(\vec{r}) = \sum_{c=1}^{nc} B_{1,c}^+(\vec{r}) \cdot x_c$$

$$B_1^+(p) = \sum_{c=1}^{nc} B_{1,c}^+(p) \cdot x_c \qquad \textbf{(3-19)}$$

However, to gain meaningful field maps of the individual elements is non-trivial itself. There are different ways to accomplish that, each with specific advantages and drawbacks [60]. The most direct way is B_1^+ mapping of the actual subject under investigation, as described in chapter 3.3.3. The advantage of this approach is that the influences of subject geometry, coil positioning and slice positioning are correctly captured in the B_1^+ map. The disadvantage is an additional scan time for each B_1^+ map, which can consume a significant part of the limited scan time for a large number of channels. Moreover there is no established procedure available for in-vivo CMR applications for the time being, although pioneering results within acceptable scan times were reported recently [61]. Another way is to facilitate simulations with human voxel models. As the EM field simulation is necessarily conducted for SAR evaluation, this data is readily accessible and delivers 3D maps of absolute field values. This approach is feasible for applications and subjects that fit to an existing human voxel model, while inevitable differences in subject geometry and positioning are not captured.

Given a set of individual transmission fields a optimization algorithm together with an application dependent merit function are used to calculate the optimal excitation amplitudes and phases for each channel. This optimization problem is an inverse problem, as the observable parameters are given and the model parameters have to be inferred from the observed values of the observable parameters [62]. In the case of B_1^+ shimming the relation between the model parameters and the observable parameters is given by the matrix $\overline{\overline{M}} \in \mathbb{C}^{nc\ x\ np}$, consisting of the individual B_1^+ contributions from every channel to every pixel. The vector $\vec{x} \in \mathbb{C}^{nc\ x\ 1}$describes the complex excitation amplitudes for every channel. The vector

$\overrightarrow{B_1^+} \in \mathbb{C}^{np\,x\,1}$ consists of the resulting excitation field for every voxel. The optimization problem is then given by the linear matrix equation (3-20).

$$\overrightarrow{B_1^+} = \overline{\overline{\mathrm{M}}} \cdot \vec{\mathrm{x}} \tag{3-20}$$

The straight forward way to solve this problem is to calculate the (pseudo-)inverse matrix of $\overline{\overline{\mathrm{M}}}$ as a least squares solution of the linear problem. Unfortunately this solution is suboptimal for most applications in MRI, as it equally optimizes the phases and the amplitudes to fit a given excitation field vector $\overrightarrow{B_1^+}$. In the case of magnitude imaging the phase of the resulting B_1^+ field is not of interest and the negligence of any phase constraint in the optimization gives rise to better performance in the amplitude optimization [63]. Rewriting equation (3-20) for magnitude optimization leads to the nonlinear equation (3-21).

$$\left|\overrightarrow{B_1^+}\right| = \left| \overline{\overline{\mathrm{M}}} \cdot \vec{\mathrm{x}}\right| \tag{3-21}$$

Optimization algorithms capable of solving multi-dimensional non-linear problems and reported for B1 shimming [63–66] are magnitude-least-squares [67], Levenberg-Marquardt [68] and simulated annealing [69]. Excitation field homogeneity and efficiency are the two most important optimization goals. Depending on the application or the imaging technique one or the other is more important and multiple phase and amplitude settings can be applied during a MRI scan [58].

3.3.5 Signal-to-noise scaled imaging

To assess SNR and parallel imaging performance in a multi-channel receive scenario SNR scaled imaging is a powerful tool. A commonly used manual way of approximating the SNR is to divide the mean signal value in a chosen region of interest with the standard deviation of the signal of a chosen region including only noise [70, 71]. This procedure gives a rough estimate of the SNR, but suffers from the variability of a chosen noise-only region. It is also not capable of exhibiting the spatial resolved noise behavior in a parallel imaging setup. Therefor the SNR values for parallel imaging evaluation in this work are acquired with a dedicated imaging technique to reconstruct MR images in SNR units [72]. This imaging technique uses a noise pre-scan without an excitation pulse to measure the noise. This data is also used to determine the noise correlation between different elements.

3.4 Electromagnetic field simulations

Electromagnetic field (EM) simulations are an increasingly powerful tool to foster the research in the field of RF technology. EM simulations offer insights into the performance of novel RF technology before the first hardware is built. That way the assessment of a wide range of designs as well as the optimization of different design parameters is feasible which saves time and resources. Furthermore EM simulations are the standard way to prove compliance with regulatory norms [73] concerning energy absorption and heating induced by RF field exposition. EM simulations are based on solving Maxwell's Equations on a discretized model of the actual design either in time or frequency domain. Yee cells [74] are used to define the electrical field components $\vec{E} = E_x \vec{x} + E_y \vec{y} + E_z \vec{z}$ and magnetic field components $\vec{H} = H_x \vec{x} + H_y \vec{y} + H_z \vec{z}$ in the three directions of space for an elementary volume element (voxel), see Figure 16. The propagation of a given excitation with given boundary conditions at the borders of the simulation domain is then calculated along the three dimensional grid of Yee cells for discrete time steps.

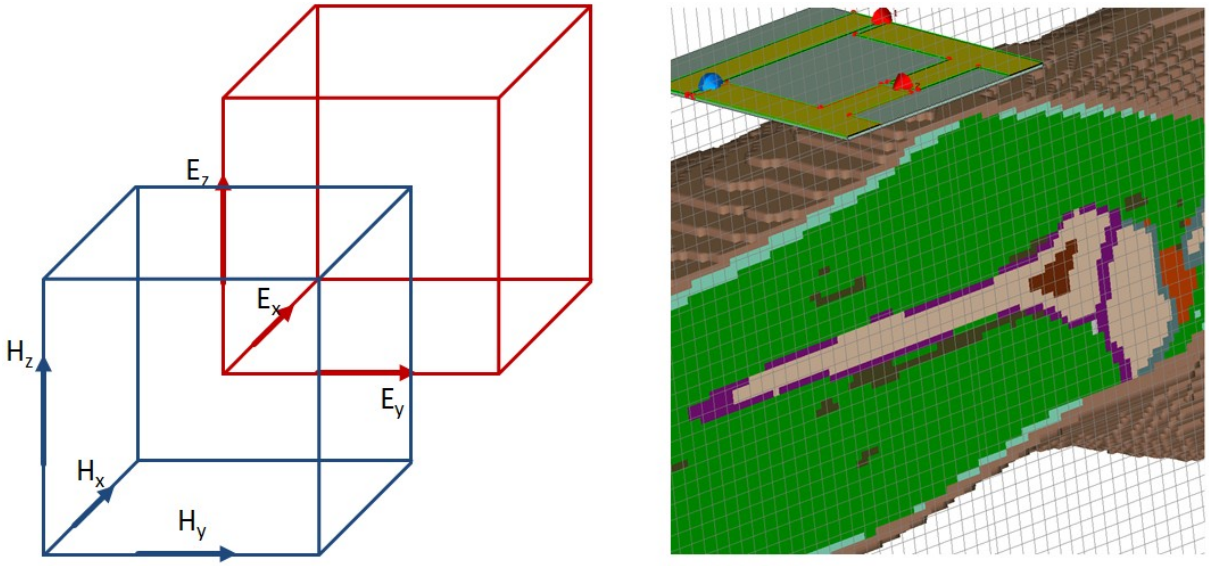

Figure 16: *On the left the discretization based on Yee cells is illustrated for one voxel with the field components defined on different legs of the grid. The grid for the electrical and magnetic field components are interleaved in space. On the right an exemplary part of the simulation domain is shown, including the grid lines, the discretized human voxel model and a copper loop element.*

The Finite-Difference Time-Domain (FDTD) Method [75] is solving the differential form of the Maxwell's equation, while the Finite Integration Technique (FIT) [76] is solving the integral form. The commercial software CST Studio Suite (CST Computer Simulation

Technology AG, Darmstadt, Germany) implementing the FIT method was used for EM simulations throughout this work. The generation of the discrete grid is generally automated in the software, nevertheless a large number of signal sources and small structures in an overall large model as it is the case for MRI RF arrays challenge the built-in mesh generation. Manual adjustments are necessary to assure a correct representation of the model in the discretized model while balancing accuracy and simulation time. The solver is terminated when the energy introduced by the excitation signal is absorbed in the model. In case of resonant structures with a high quality factor, see equation (3-8), the simulation time can be excessive. As for spin excitation the circular polarized component of the B field is decisive, it is calculated from the H field by equation (3-22).

$$B_1^+(\vec{r}) = \frac{H_x(\vec{r}) + jH_y(\vec{r})}{2\mu_0} \tag{3-22}$$

3.4.1 Numerical EMF simulation of multichannel arrays

The simulation of multichannel arrays challenges existing simulation software packages in terms of computational time, memory requirements and mesh generation. The antenna elements are resonant circuits with low losses. Therefore the energy is stored and dissipates very slowly, leading to extensive simulation times until the energy criterion is met. The number of independent signal sources scales with the number of elements, each of which has to be simulated separately. A way to remove the resonance behavior and additionally receive more freedom for post processing is to use circuit co-simulation [77]. The simulation is divided into two steps. In the first step the 3D field solution is simulated with plain, non-resonant antennas without tune and match capacitors. Subsequently the capacitors are added in a schematic including the simulated data block in a circuit simulator. This gives the freedom to choose and alter the capacitor values without re-simulation of the whole 3D problem. In a final step a field combination of the simulated 3D EM fields together with the chosen capacitors is performed.

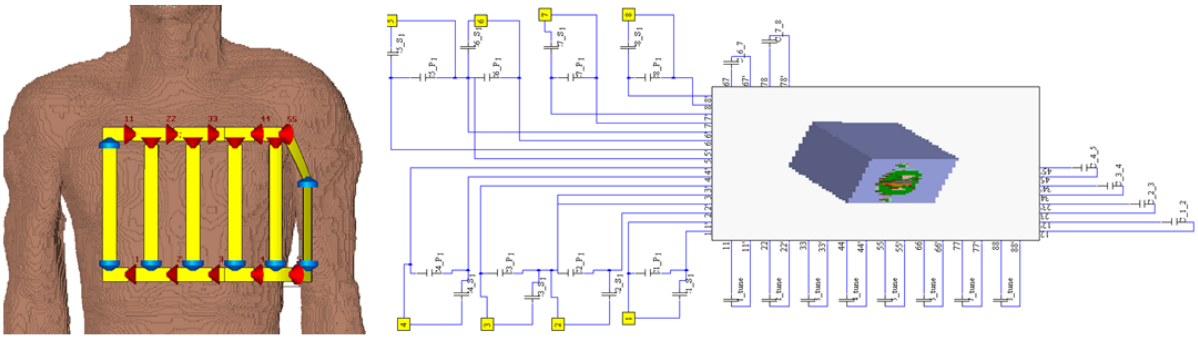

Figure 17: *The circuit co-simulation shown at the exemplary simulation setup of an eight channel array. On the left the 3D model with capacitors (blue cones) and signal ports (red cones) is shown. The ports are connected to capacitors for element decoupling, tuning and matching as depicted on the right in a circuit simulator. This process eliminates the resonant behavior of the 3D model of the antenna elements and introduces the freedom to change capacitor values without re-simulation of the 3D problem.*

3.4.2 Human voxel models

For the purposes of biomedical research a growing number of human models of both genders and different ages and body mass indexes (BMI) are available. The Virtual Family (ITI'S Foundation, Zurich, Switzerland) [78] currently consists of 10 models from 5 to 84 years. Each model is deduced from an existing human, discretized into 1mm³ voxels and each voxel assigned to one of 84 tissue types. In a separate user defined file the properties of this tissue types can be set. The dielectric properties of body tissues are frequency dependent, thus for the use in MR research the tissue parameters have to be adjusted to the frequency of the system. An online-database [40] allows accessing the dielectric properties of body tissues in the frequency range of 10 Hz to 100 GHz [79].

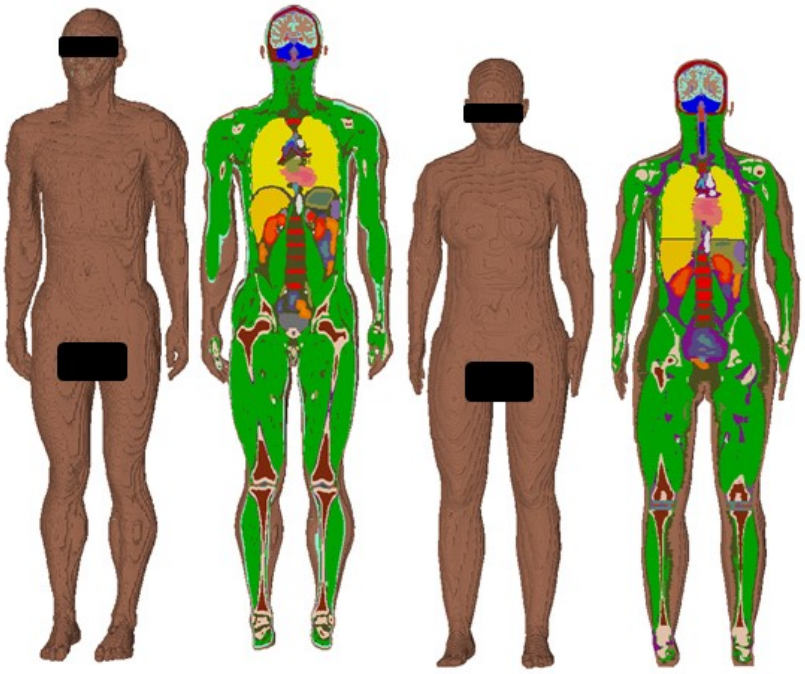

Figure 18: *Human voxel models Duke (male) and Ella (female) of the Virtual Family. Duke is a 34 year old male with a weight of 72.4 kg, a height of 1.77 m and a BMI of 23.1. Ella is a 26 year old female with a weight of 58.7 kg, a height of 1.63 m and a BMI of 22.0.*

3.4.3 Numerical simulation of the specific absorption rate

RF exposition of human tissue leads to dielectric heating, as the molecules attempt to align with the continuously alternating electric field. Based on the simulated electrical field distribution and the material matrices for density (ρ) and conductivity (σ) of the human voxel models the absorpt RF energy in each voxel can be calculated. The specific absorption rate (SAR) is defined in formula (3-23) and has the unit W/kg.

$$\mathrm{SAR} = \frac{\sigma \left|\vec{E}\right|^2}{2\rho} \tag{3-23}$$

In MRI SAR values based on simulated E-field distribution are serving as a surrogate for the temperature increase, as direct temperature supervision of the complete body is not yet practicable [80]. Disregarding the effects of thermal diffusion and blood perfusion as well as physiological thermoregulation that may moderate the temperature rise leads to equation (3-24).

$$\Delta \mathrm{T} = \frac{1}{c_i} \mathrm{SAR}\, t_{RF} \tag{3-24}$$

A SAR exposition of water (heat capacity ci = 4186 Ws/kg°Celsuis) with 10 W/kg over 6 minutes leads to a temperature increase of 0.86°celsuis. Regulatory norms [81] limit both the maximum temperature increase to 1°C and the SAR to the values surveyed in Table 3. The SAR values are given for an averaged SAR over volumes of 10 g of tissue. The averaging algorithms according to the IEEE standard [82] are implemented in the commercial simulation software.

	Head	Trunk	Extremities
Normal mode	10 W/kg	10 W/kg	20 W/kg
First level controlled mode	20 W/kg	20 W/kg	40 W/kg
Second level controlled mode	>20 W/kg	>20 W/kg	>40 W/kg

Table 3: *Local SAR limits defined by the International Electrotechnical Commission (IEC)* [81] *that apply for custom built RF coils in human MRI.*

3.5 Human ultrahigh field MRI and clinical applications

3.5.1 Ethics statement

For the in vivo studies, subjects were included after due approval by the local ethical committee (registration number DE/CA73/5550/09, Landesamt für Arbeitsschutz, Gesundheitsschutz und technische Sicherheit, Berlin, Germany). Informed written consent was obtained from each volunteer and patient prior to the study in compliance with the local institutional review board guidelines.

3.5.2 MR safety

Assuring subject or patient safety in an MR environment includes several topics [83,84]. Magnetically induced displacement forces by the static magnetic field, torques on moving conductive parts inside the static field, displacement forces induced by fast changing magnetic fields of the gradient system and heating or induced voltages due to the RF excitation. Moreover in patient handling the MR compatibility of implants, the potential increase of RF induced heating in the presence of implants as well as the potential malfunction of medical devices has to be taken into account. Regulatory norms [81] define

the limits for static magnetic field strength, field gradients, RF induced temperature increase and RF power deposition. The specific MR safety concern connected with RF transmit arrays is localized RF power deposition, which is covered by SAR limits in the regulatory norms. The evaluation of localized SAR is introduced in the EMF simulation chapter 3.4.3.

3.5.3 Cardiac magnetic resonance imaging

Cardiac diseases are the leading cause of mortality in the world [85, 86]. Cardiac MRI (CMR) plays an important role in today's clinical practice, as it offers a great variety of image contrasts to differentiate cardiac disorders [87, 88], i.e. allows for cardiac chamber quantification [70], wall motion analysis and analysis of myocardial perfusion [89]. For myocardial perfusion contrast agents are routinely used in clinical practice to enable MRI to perform comparable to nuclear imaging techniques [90]. UHR CMR holds the further promise to offer sufficient contrast without the use of contrast agent or translate the intrinsic SNR gain into enhanced temporal or spatial resolution [64, 91, 92]. A considerable number of reports explore the capabilities of UHF CMR [8, 70, 91, 93, 94]. Nevertheless CMR is considered as a highly challenging application for UHR MR. As the heart is located centrally in the upper torso, excitation field inhomogeneities leading to signal voids bear the potential to render the images non-diagnostic. Increased radio frequency absorption may limit the applicable excitation power necessary to excite deep-lying regions of the body. Image acquisition of the heart is time restricted by the cardiac cycle, respiratory motion and limited breath-hold times. Finally established cardiac triggering methods like the electrocardiogram (ECG) are not working properly inside a UHF magnet, therefore acoustic cardiac triggering is used. An MR stethoscope [41, 95] (MRI.TOOLs GmbH, Berlin, Germany) was used for cardiac gating to avoid motion artifacts induced by miss-synchronization which frequently occurs at 7.0 T when ECG gating is being used. Chapters 4.2 to 4.6 report on novel RF array designs for CMR using 8, 16 and 32 elements facilitating loop antennas as well as dipole antennas.

3.5.4 Cardiac anatomy and physiology

The human heart is located centrally in the upper torso with the apex of the heart pointing to the left side. Its function is to provide blood flow through the lungs and the body by a continuous cycle of contractions (systole) and relaxations (diastole) of the myocardium. The heart consists of two chambers, the right ventricle and the left ventricle with the corresponding left atrium and right atrium. Blood from the venous system of the body enters the right atrium with a low blood oxygenation level. The right ventricle circulates the blood in

the pulmonary circuit to get oxygenated in the lungs. The oxygenated blood enters the left atrium and the left ventricle circulates the blood into the systemic circuit trough the aorta into the vascular system of the body. The heart muscles itself are supplied with oxygenated blood by the coronary arteries. The systemic circuit presents a much higher resistance to the ventricle, thus the myocardium encompassing the left ventricle is more pronounced. During systole the right atrium is separated from the right ventricle by the mitral valve and the right atrium is separated from the left ventricle by the tricuspid valve. The papillary muscles support the vanes to withstand the pressure inside the ventricles during contraction. [96]

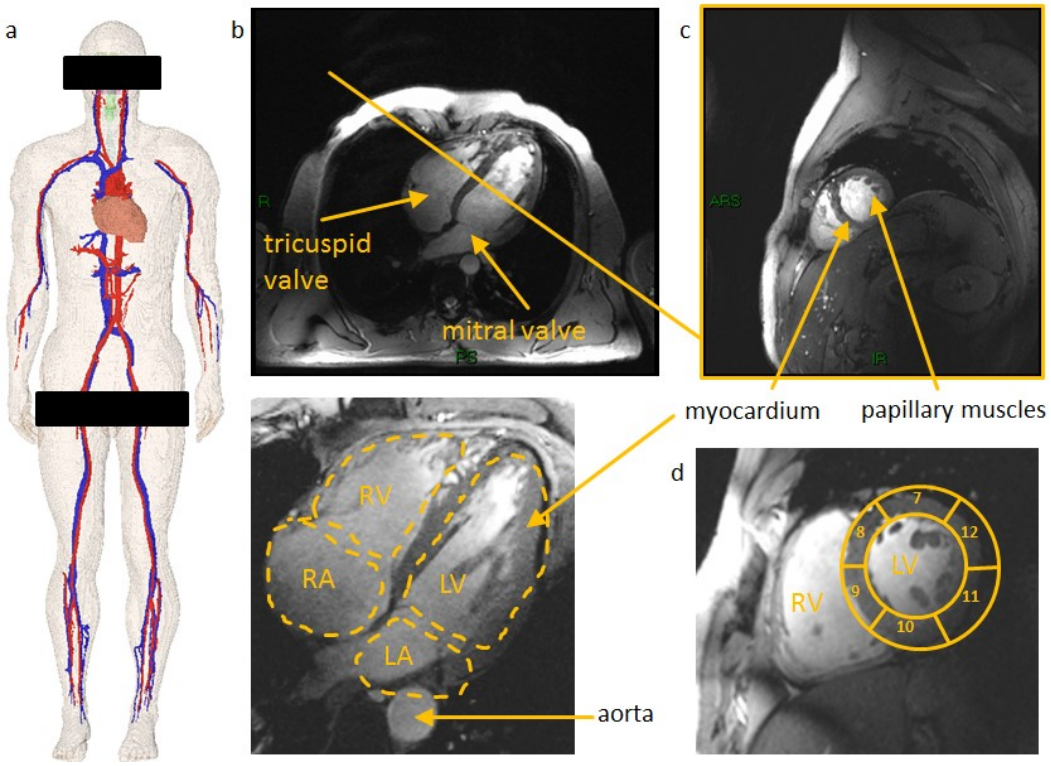

Figure 19: *Cardiac anatomy shown in the human voxel model Duke and in MR images.* ***(a)*** *Position of the heart and the main arteries (red) and veins (blue) of the human cardiovascular system. The heart, defined by its main axes, lies in a double oblique position in the upper torso.* ***(b)*** *The MR image of the human heart along the long axis shows the left ventricle (LV), left atrium (LA), right ventricle (RV), right atrium (RA) the, aorta and the tricuspid and mitral valves.* ***(c)*** *Perpendicular to the long axis slice a mid-ventricular short axis slice is shown, depicting the myocardium circumferencing the left ventricle as well as the papillary muscles, which prevent the mitral valve from moving into the right atrium during contraction.* ***(d)*** *Standardized myocardial segments* [97] *for a mid-ventricular short axis view used for analysis throughout this work.*

To name myocardial segments in a standardized way Cerqueira et.al. [97] proposed a 17-segment system, subdividing the myocardium of the left ventricle into three rings of, basal, mid-ventricular and apical segments plus the apex. For the basal ring the segments are

depicted in Figure 19 d and are used for signal intensity evaluation of the in-vivo results of this work.

Immediate knowledge about the cell viability of cardiac tissue regions affected by an ischemic event is a valuable information to support treatment decisions. Sodium (^{23}Na) MRI is a promising approach for non-invasively gaining better insights of (patho-) physiological processes and cellular metabolism and is widely applied in biomedical research applications [98]. Cardiovascular ^{23}Na-MRI has been shown to be suitable for the detection and assessment of acute and chronic heart disease due to increased sodium concentration after myocardial infarction [19, 99–102]. In healthy tissue the cell membrane maintains a intracellular sodium concentration of abour 16 mmol/L against an extracellular concentration is about 140 mmol/L [103]. In case of impaired cell membranes this gradient decreases and affected tissue can be detected by an increased signal in ^{23}Na-MRI. Admittedly, the bi-exponential decay of the ^{23}Na signal and its low sensitivity versus clinical ^{1}H-MRI together with long scan times deems ^{23}Na of the heart a challenge. ECG gated ^{23}Na MRI of the heart was already applied at magnetic field strengths of 1.5 T [104] and 3 T [105]. However, due to the low in vivo signal it is hard to achieve clinical acceptable image quality [106]. With the sensitivity gain intrinsic to ultrahigh fields and yet unhampered B_1^+ homogeneity due to the comparably low resonance frequency cardiac ^{23}Na-MRI is conceptually appealing for applications in UHF MRI.

3.5.5 Musculoskeletal magnetic resonance imaging

A number of publications have reported on the advances of musculoskeletal (MSK) MRI at ultrahigh fields [107–110]. The aim of increased field strength for MSK MRI at first place is the translation of the intrinsic SNR gain of UHF MRI into sub millimeter spatial resolution images. MSK MRI at clinical magnetic field strength of 1.5 T has to deal with partial volume effects that bear the potential to obliterate pathologies. Further refined UHF MR images are promising to extend the clinical abilities to profoundly access the morphology of articular cartilage and to detect superficial degenerative and posttraumatic cartilage lesions in an early state [111]. Although the benefits of UHF for MSK MRI are straight forward, the clinical research is impaired by the need of tailored RF antennas, safety evaluation and excitation settings for every single of the numerous applications, see Figure 20. Recent publications focus and report on some very specific RF coil designs [112,113]. The aim of this work is to translate the RF transceiver building block technology designed for body imaging to MSK

applications and underline the feasibility of a more flexible RF coil design, see chapter 4.8 and 4.9.

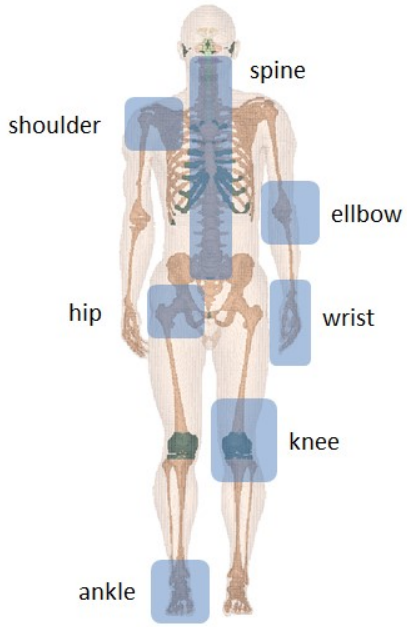

Figure 20: *Musculoskeletal applications for MR imaging shown on the human model Duke. The number of different joints presents a challenge for clinical UHF research, as tailored hardware needs to be developed and evaluated for every single application. Nevertheless most of the regions of interest are near the body surface, thus facing minor challenges concerning transmission field homogeneity, penetration depth and SAR constraints.*

3.5.6 Ophthalmic magnetic resonance imaging

Imaging of the human eye in today's clinical routine is based on several imaging modalities. Ultrasound techniques are an inexpensive way to assess intraocular tumors, but resolution declines with the depth of tissue penetration and tissue density [114, 115]. Optical techniques like optical coherence tomography provide a ultrahigh spatial resolution unmet by any other modality [116], but they require an unobstructed pathway for the light through the lens to the region of interest. CT provides a quick scan of the bone integrity and can localize suspected metallic pieces inside the orbita. MRI is the most time- and cost intensive methods and does not provide real-time imaging, nevertheless it offers high resolution images almost independent of the distance to the surface and tissue density of all intra- and extraorbital structures as well as the optical nerve without distortions [117]. Uveal melanoma is the most common malignant intraocular tumor in humans and its delineation and evaluation of scleral invasion and extrascleral extensions is of high importance for the treatment decision making [114, 118]. Anatomical imaging of the optic nerve bears clinical relevance for optic neuropathies in neuroinflammatory diseases and also for the differential diagnosis of

debilitating autoimmune or orphan diseases of the central nervous system that run the risk of visual impairment [119, 120]. The near-surface position of the eyes together with the need for high spatial resolution makes it an advantageous application for UHF MRI, as the small dimensions of the eye are not prone to excitation inhomogeneities. However susceptibility artefacts at the air-tissue interface of an opened eye can occur. Also the fixation of the eye for the time of image acquisition is challenging. Taking advantage of the coupled movement of both eyes in humans, fixating with one eye while imaging the other one in closed position is possible [121] and allows for artefact free images. On the technology side multichannel RF arrays supporting accelerated imaging are another way to mitigate motion artefacts due to extensive scan times. To assure the physical integrity of the eye of the subject with its limited temperature reception and regulation capabilities an extensive evaluation of RF absorption behavior is compulsory before conducting a UHF in-vivo study.

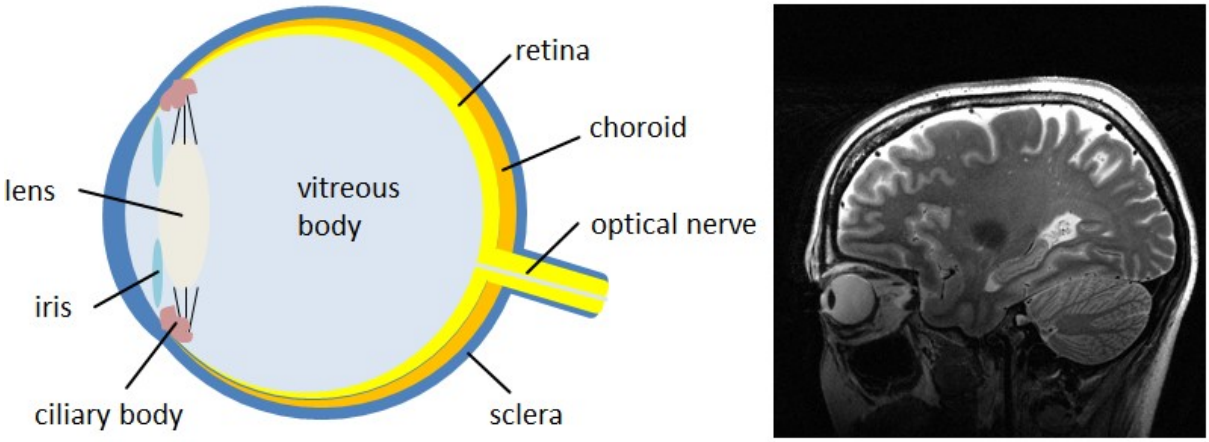

Figure 21: *On the left a schematic view of the human eye is introducing the different soft tissues. The MRI scan on the right depicts the size and position of the eye and the optical nerve inside the human head.*

4. Results

4.1 Optimized transmission filed shaping

For all RF transceiver array developments reported in this thesis transmission field shaping presented a pivotal task to enable homogeneous MR images for diagnostic image quality. To solve the non-linear optimization problem stated in equation (3-21) a MATLAB (MathWorks, Natick, MA) program was developed. The Levenberg-Marquart algorithm was incorporated in its implementation available in the commercially available Optimization Toolbox of MATLAB. In a single voxel the field contributions of the different transmit elements sum up with respect to the individually applied amplitudes and phases. The sum-of-squares (SOS) combination $B_{1,SOS}^{+}$ of the individual fields gives the theoretical optimum for every voxel, equivalent to the non-physical scenario of all field components in phase in every voxel.

$$B_{1,SOS}^{+}(p) = \sum_{c=1}^{nc} \left| B_{1,c}^{+}(p) \right| \tag{4-1}$$

Practically, as the phase and amplitude setting for the transmit elements apply to all voxels, this leads to a complex field pattern with either constructive or destructive interference in different voxels. The task of transmission field shaping, also commonly referred to as B_1^+ shimming, is therefore to find the optimum combination of the underlying individual fields and to balance homogeneity and efficiency both with respect to the application and the ROI.

For homogeneity optimization equation (4-2) was chosen as the merit function with $\|\cdot\|$ denoting the L2 norm of the vector and $\vec{1}$ denoting the unit vector. The median value, representing the optimization goal for every voxel, was updated in every iteration of the solving process. For computational efficiency the faster median function was used instead of calculating the mean. If the solver converges to a homogeneous solution the difference between both functions is negligible.

$$\vec{x}_{homo} = arg_{\vec{x}} \min_{\vec{x}} \left(\left\| \left| \overline{\overline{M}} \cdot \vec{x} \right| - median\left(\left| \overline{\overline{M}} \cdot \vec{x} \right| \right) \cdot \vec{1} \right\| \right) \tag{4-2}$$

For efficiency optimization (4-3) the mean value of all voxels inside the ROI was exchanged by the individual maximum for each voxel, given by the SOS vector.

$$\vec{x}_{eff} = arg_{\vec{x}} \min_{\vec{x}}\left(\left\| \left| \bar{\bar{\mathrm{M}}} \cdot \vec{\mathrm{x}} \right| - \overrightarrow{\mathrm{B}_{1,SOS}^{+}} \right\|\right) \tag{4-3}$$

Therefor the efficiency merit function will typically result in a higher mean excitation field value, compromising the overall homogeneity. To apply different amplitudes to different channels software defined RF attenuators or independent RF power amplifiers are necessary. The latter are called parallel transmit arrays, but only a minor number of systems featuring 2, 8 independent transmit channels are commercially available for investigational use for the time being. To not restrict the results obtained in this work to these systems and bearing in mind the up to 32 independent transmit channels facilitated in this work the transmit settings $\vec{\mathrm{x}}$ were restricted to phase differences, keeping the amplitude constant over all channels. Unlike amplitude differences phase differences can easily be introduced by phase shifting cables at negligible costs. With the vector $\vec{\theta}$ describing the transmit phase setting (PS) the merit functions (4-2) and (4-3) can therefore be rewritten in the form (4-4).

$$\begin{aligned} \vec{\theta}_{homo} &= arg_{\vec{\theta}} \min_{\vec{\theta}}\left(\left\| \left| \bar{\bar{\mathrm{M}}} \cdot e^{-i\vec{\theta}} \right| - median\left(\left| \bar{\bar{\mathrm{M}}} \cdot e^{-i\vec{\theta}} \right|\right) \cdot \vec{1} \right\|\right) \\ \vec{\theta}_{eff} &= arg_{\vec{\theta}} \min_{\vec{\theta}}\left(\left\| \left| \bar{\bar{\mathrm{M}}} \cdot e^{-i\vec{\theta}} \right| - \overrightarrow{\mathrm{B}_{1,SOS}^{+}} \right\|\right) \end{aligned} \tag{4-4}$$

Nonlinear problems may have a large number of local minima and nonlinear solvers are prone to stop at a local minimum instead of the global minimum. To prevent this the solver was started at a large number of random starting points and the solution exhibiting the smallest residuum is captured. Parallel computing was used to accelerate the optimization process. The number of random starting points was chosen empirically by comparing multiple optimization processes. To summarize the transmission field optimization Figure 22 shows the workflow in a block diagram.

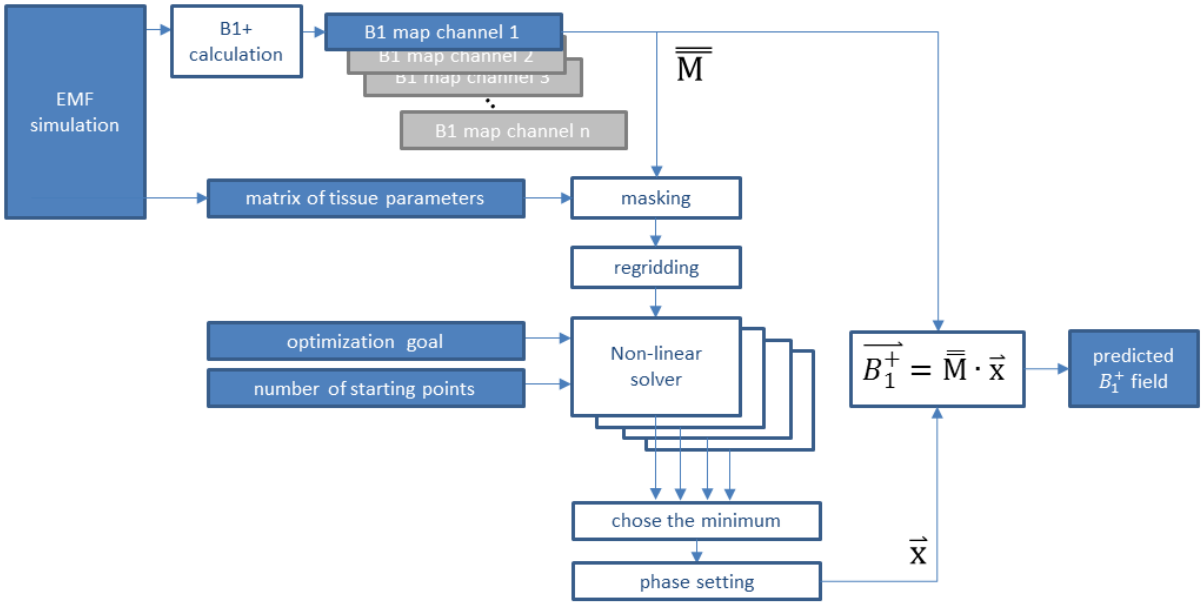

Figure 22: *Workflow of the proposed transmit field shaping based on simulated magnetic fields. The circular polarized field component is calculated from the B-fields for every channel. The material matrix is used to exclude non-tissue areas from the optimization region or limit the optimization to a specific organ. The simulated dataset has a variable grid with step sizes f down to 0.5mm. Regridding is performed to reduce the matrix size which reduces computational time and memory requirements. As the wavelength in tissue is approximately 12cm a moderately reduced resolution of 4mm isotropic is still appropriate to cover all interference effects.*

4.2 8-channel transceiver array for cardiac MRI

Cardiac Magnetic Resonance Imaging (CMR) at 7.0 Tesla is an area of ongoing vigorous research. Based on reported results of a four channel loop array successfully used for CMR [11] the objective of this study was to design a cardiac optimized eight channel transceiver surface coil array configuration that uses loop elements, and that provides image quality suitable for clinical use. An increased number of channels is promising to provide degrees of freedom for B_1^+ homogenization and parallel imaging capabilities. Another step towards enhanced transmit and receive capabilities is the tailoring of the RF coil geometry to the geometry and position of the human heart. For this purpose a lightweight, 8-element configuration which fits to the anterior chest is designed and evaluated. RF characteristics of the proposed array are presented in conjunction with EMF and SAR simulations. Its suitability and efficacy for 2D CINE acquisitions and left ventricular (LV) chamber assessment is examined in an initial volunteer study as a precursor to a broader clinical study

Parts of the work outlined in this chapter were published in a peer-reviewed journal [122].

4.2.1 Design considerations

An 8-element cardiac transceiver array with a resonance frequency of f=298 MHz was constructed. It comprises a posterior and an anterior section as shown in Figure 23. The anterior section was curved to conform to an average chest as demonstrated in Figure 24. Five loop elements were laid out to cover the center and the left side of the torso. The posterior section comprises three elements in a planar shape and was integrated into the patient table cushions.

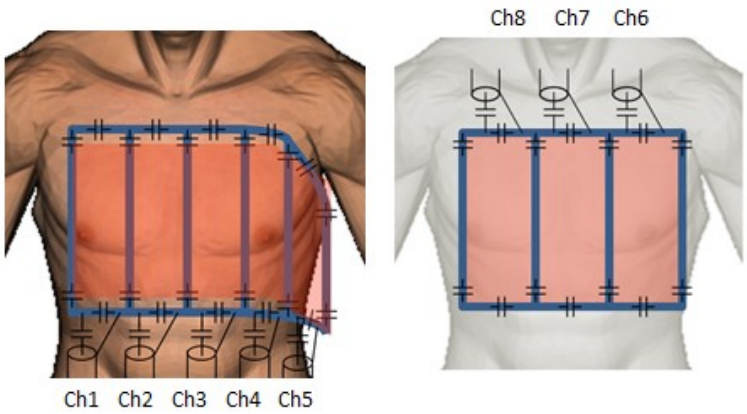

Figure 23: *Circuit layout of the anterior (left) and posterior (right) part of the eight channel cardiac array. The copper structure is depicted in blue, the RF shield in 2cm distance above the elements is shaded in red.*

The loop elements of the anterior section cover a surface area of 12 cm² using an element size of (6 x 20) cm². A surface area of 18 cm² was chosen for the posterior loop elements with an element size of (9 x 20) cm². The asymmetric design together with placing more and smaller elements at the chest versus the back is advantageous for cardiac imaging [123,124]. Larger elements in the posterior section utilize the higher penetration depth to reach the intended target region. The extension of the loop elements along the z-direction was set to 20 cm to cover the entire heart. The left-right extension was set to 30 cm for the set of five anterior elements and 29 cm for the set of 3 posterior elements to achieve whole heart coverage. Decoupling of adjacent coil elements was accomplished with a common conductor and a shared decoupling capacitor. This approach is beneficial since it uses a simple conductor design and provides less loss due to the absence of destructive currents in neighboring loops. The conductor width was set to 20 mm to reduce ohmic losses. A RF shield made of slotted copper foil to minimize eddy currents was placed above the array to reduce radiation losses. A distance of 2 cm between the loop elements and the shielding was used to balance field distribution and geometric constraints.

Figure 24: *Resulting RF coil hardware. On the right the array is placed on a mannequin. In the middle the anterior part is shown without the RF shield, on the right the posterior part respectively. The apparently shifted placement of the compartments is a results of the incorporation of the cable traps at different ends into the housings.*

For each loop element a cable trap was placed in the feeding cable with its position being in a distance of 1/12 of the wavelength along each cable. The cable traps were designed as a tuned parallel resonant circuit, consisting of a single loop of the cable and a capacitor, see Figure 12. This approach imposes large impedance to signals conducted on the shield of the coax cable for a resonance frequency of 298 MHz. The coil casing was designed with the computer aided design (CAD) tool Autodesk Inventor 2011 (Autodesk Inc., San Rafael, CA, USA) and printed with a 3D rapid prototyping system BST 1200 es (Dimension Inc., Eden Prairie, MN, USA) using ABS+ material. The casing was tailored to provide a minimum distance of 15 mm from any part of the loop structure to the human tissue. This helps to shift SAR hotspots due to strong electrical fields in the vicinity of the conductors away from the torso. The posterior section was designed to accommodate the weight of a human. The weight of the anterior part is 2.1 kg, the weight of the posterior part is 1.8 kg.

4.2.2 Electromagnetic field simulations

The EMF Simulations were conducted in CST Studio Suite 2010 as introduced in chapter 3.4. The simulation setup included an accurate model of the RF coil array and the human model Duke from the Virtual Family. A basic mesh resolution of 2 mm × 2 mm × 2 mm was set to assure a homogeneous mesh and to keep differences in step size small. For rapid tuning, matching and decoupling of the 8 channels, the corresponding capacitors were modeled as 50 Ω ports. The results of the 3D simulations were post processed using an RF circuit co-simulator (Design Studio, part of CST Studio Suite 2010) as described in [77]. The capacitor values were optimized with respect to the S-parameter simulation and provided a solid

starting point for the practical realization. For the final configuration including the phase setting used in in vivo measurements the SAR values were calculated.

4.2.3 Transmission field shaping

To reduce inhomogeneities in the B_1^+ field distribution across the heart the phase of each loop element was adjusted. The amplitudes were all set to one eighth of the input power. The B_1^+ field distribution based on the EMF simulations within the voxel model Duke of every single channel were extracted and used to tune the phases and to simulate the resulting field pattern. A Matlab graphical user interface (GUI) was used to empirically choose an appropriate phase setting for homogeneity across the heart. Hardware-wise the output of the RF amplifier was split into eight equal intensity signals by means of in-house built Wilkinson power dividers. Additional cable length corresponding to the desired phase shifts were incorporated between the power splitter and the interface box. The phase setting is surveyed in Table 4, the numbering of the channels is given in Figure 23.

channel	1	2	3	4	5	6	7	8
phase °	-45	0	-225	-228	-115	-9	-330	-294

Table 4: *Transmission phases used in the in-vivo study for homogeneous excitation with the eight channel transceiver array.*

4.2.4 Specific absorption rate evaluation

As a results of the SAR evaluation based on the EMF simulation the output of the RF power amplifier was limited to 30 W averaged over 6 minutes as stated in the regulatory norms [81]. The total mass of the voxel model was 70 kg and the exposed mass was estimated to be 26 kg, which leads to a partial body SAR limit of 7.0 W/kg, referring to the regulations given by the IEC [81]. For the RF phase settings used in the volunteer studies, the partial body SAR did not exceed 1.1 W/kg, which falls well in the limits for partial body SAR. Calculations of the local SAR (10 g average) indicate that local maxima occur on the body surface. As illustrated in Figure 25 these relative hotspots were found to be always below 13 W/kg, which corresponds to operation in the first level mode which defines a maximum local SAR of 20 W/kg. These SAR results can be understood as an estimation of a worst-case scenario for the chosen phase setting since RF power losses in the cables, the TX/RX switches and the RF components are not considered.

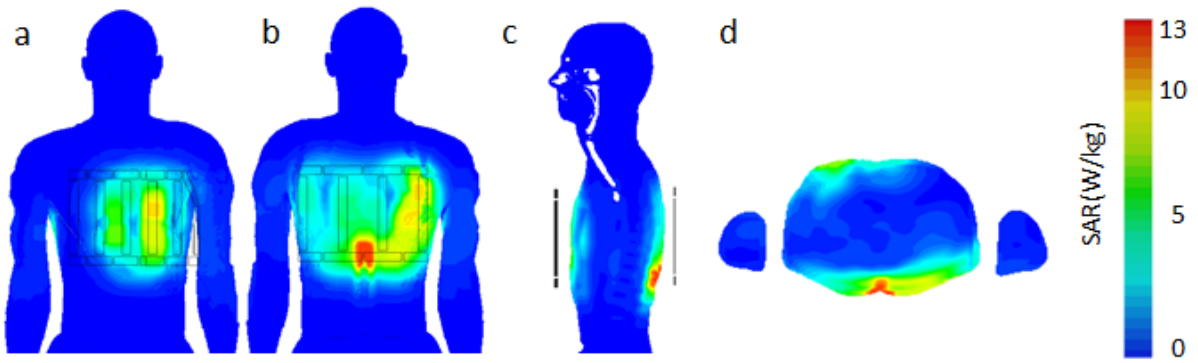

Figure 25: *Survey of the local SAR_{10g} exposition of the human model Duke when transmitting with the eight channel transceiver array with the phase setting set for the in-vivo study and 30W average RF power. The front surface **(a)**, the back surface **(b)** as well as a sagittal **(c)** and a transversal slice **(d)** intersecting the model at the maximum local SAR_{10g} are shown.*

4.2.5 Radio frequency characterization

Tuning, matching and decoupling were performed with the coil array being loaded by a subject. These settings were kept constant for all volunteers involved in the in vivo study. The s-parameters were measured with a Vector Network Analyzer (VNA) for 10 subjects. The reflection coefficients were below −14 dB and the transmission coefficients were below −11dB for all coil elements and volunteers. The decoupling between elements of the anterior and the posterior section was below −22 dB for all volunteers. The mean values of the scattering parameters derived from 10 volunteers are shown in Figure 26. The ratio of Q_U/Q_L (Q-factor unloaded over Q-factor loaded by a subject) averaged over all anterior elements was 6.45 ± 2.75. For the larger posterior elements this value was 11.4 ± 3.1. Noise correlation was measured in vivo by means of a noise prescan included in the imaging protocol [72] and averaged over 10 subjects. The resulting matrix is shown in Figure 26 and indicates that there is rather low noise correlation between the channels. For the anterior section a maximum correlation of 0.33 was observed. For the posterior section a maximum correlation of 0.28 was obtained. Both values were found for a pair of next-neighboring elements.

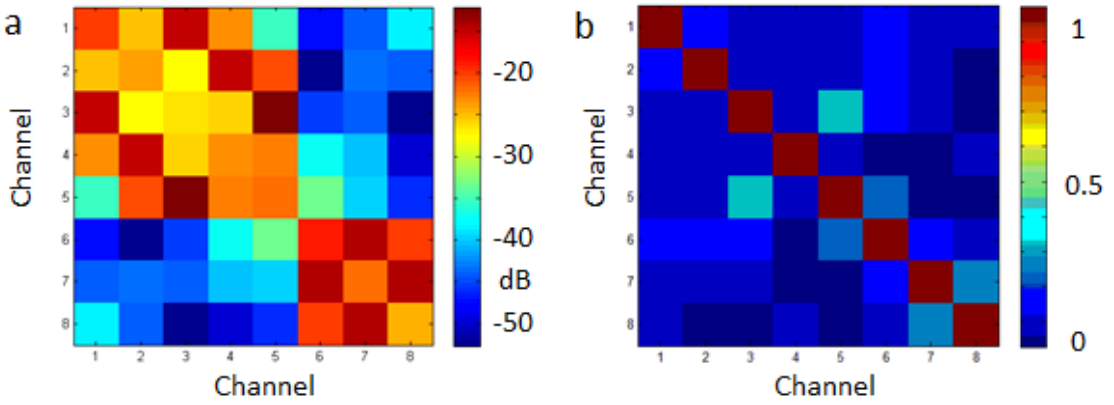

Figure 26: *RF characteristics of the eight channel transceiver array averaged over 10 subjects.* ***(a)*** *depicts the S-parameters determined by bench measurements and* ***(b)*** *the noise correlation matrix acquired by a noise pre scan during the in-vivo study.*

4.2.6 In-vivo study

In vivo cardiac imaging was performed using a retrospectively gated 2D CINE spoiled gradient echo (FLASH) technique (breath hold scan, slice thickness = 4 mm, slice gap = 2 mm, receiver bandwidth = 444 Hz/per pixel, FOV (360 mm × 326 mm), 30 cardiac phases, 6 segments, temporal resolution =33ms for a heart rate of 60 bpm). For an in-plane spatial resolution of 1.4 mm × 1.4) mm data acquisition matrix size was set to 256×232 elements (reconstruction matrix size 256 ×256 elements) using an echo time (TE) = 2.7ms and a repetition time (TR) = 5.6 ms. For an in-plane spatial resolution of 1.0 mm ×1.0 mm the data acquisition matrix size was set to 360×326 elements together with the use of a reconstruction matrix size of 512 × 512 elements, an echo time (TE) = 2.7 ms and a repetition time (TR) = 6.3 ms. For each subject two-chamber, three-chamber and four-chamber standard views of the heart were acquired. For cardiac chamber quantification a set of short axis views of the heart ranging from the atrioventricular ring to the apex were acquired to achieve coverage of the entire left ventricle. Image acquisition was confined to a single view/slice per end expiratory breath-hold. Neither subject specific B1-shimming nor re-adjustment of the coil was performed.

All subjects tolerated all examinations well without adverse events. Cardiac images derived from 2D CINE FLASH acquisitions using the 8-channel TX/RX coil array in conjunction with the phase setting stated above provided rather uniform image intensity as depicted in Figure 27 for long axis views of the heart and as demonstrated in Figure 28 for a set of short axis views of the heart.

Figure 27: *2D FLASH CINE images acquired with the proposed 8-channel TX/RX coil array with an in-plane resolution of 1.4 mm × 1.4 mm. A four chamber view* ***(a)****, a three chamber view* ***(b)*** *and a two chamber view* ***(c)*** *acquired at end-diastole are shown.*

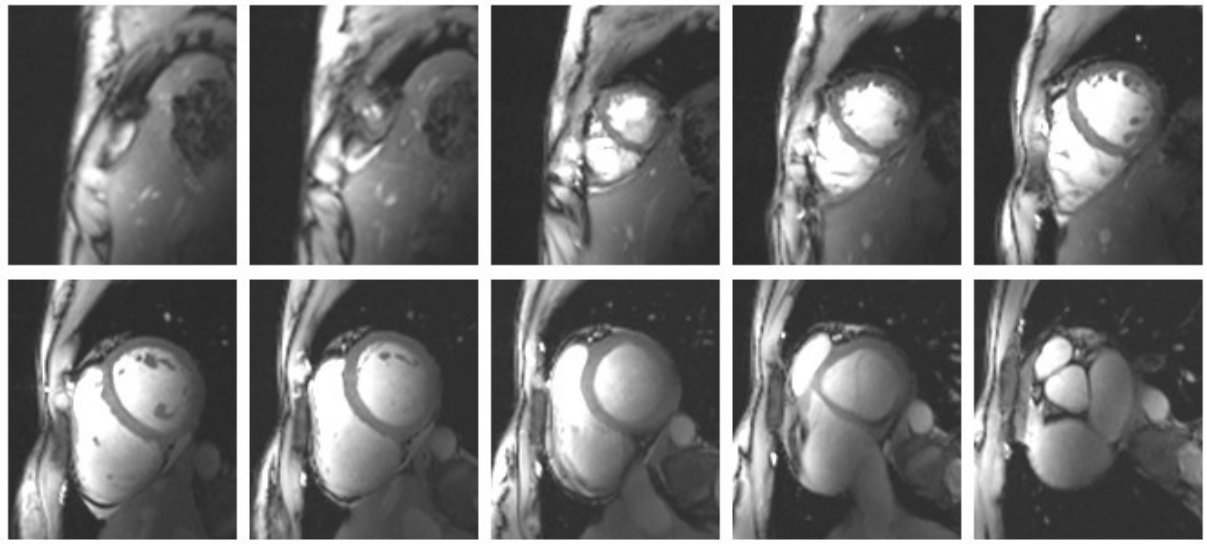

Figure 28: *Set of short axis views covering the entire heart from the apex to the atrioventricular ring. The proposed 8-channel TX/RX coil and a 2D CINE FLASH technique were used for data acquisitions. An in-plane resolution of 1 mm × 1 mm and a slice thickness of 4 mm were applied.*

The baseline SNR advantage at 7.0 T was put to use to acquire images with an in-plane resolution as low as 1 mm × 1 mm together with a slice thickness of 4mm, which is superior to the spatial resolution commonly used in current clinical practice [125]. SNR analysis was performed for a short-axis view in end diastole. For un-accelerated 2D CINE FLASH acquisitions the results indicate an average SNR of approximately 140 for the left ventricular blood pool. The average blood/myocardium contrast was found to be approximately 90 for un-accelerated 2D CINE FLASH acquisitions.

4.2.7 Parallel imaging performance

Parallel imaging was performed using GRAPPA [32] with reduction factors of R = 1, R = 2, R = 3, R = 4. For analysis of parallel imaging data off-line SENSE reconstruction was also applied [18]. For this purpose, full frequency domain data sets were decimated to eliminate all effects but under sampling. For SNR and g-factor assessment reconstructed images derived from 2D CINE FLASH acquisitions of mid-ventricular short-axis views in end diastole were scaled in SNR units and g-factor maps were calculated [72].

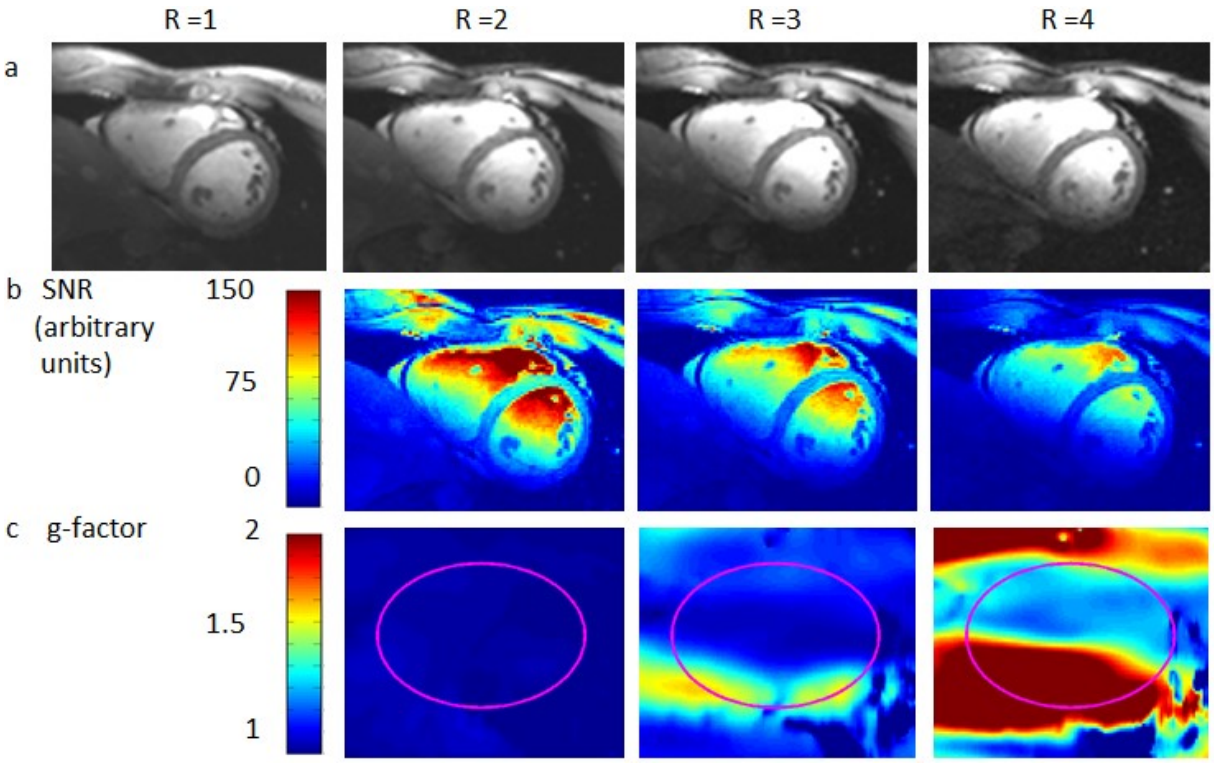

Figure 29: ***(a)*** *2D CINE FLASH images of a mid-ventricular short axis view at diastole (in-plane resolution 1 mm × 1 mm) using acceleration factors R = 1 (no acceleration), R = 2, and R=4 together with GRAPPA reconstruction.* ***(b)*** *Quantitative SNR maps of the data sets shown in* ***(a)****.* ***(c)*** *Derived g-factor-maps from data sets shown in* ***(a)****. The ROI of the heart is depicted in pink.*

For GRAPPA reconstruction the mean SNR across the myocardium was found to be 34 for R = 2, 26 for R = 3 and 17 for R = 4 as represented by the quantitative SNR maps shown in Fig. 5b. For GRAPPA reconstruction a mean blood/myocardium contrast of 65 for R = 2, 47 for R = 3 and 27 for R = 4 was observed. GRAPPA g-factors were calculated for a ROI covering the short axis view of the heart yielding mean g-factor values of g = 1.02 ± 0.01 for R = 2, g = 1.17±0.15 for R = 3 and g = 1.58±0.43 for R = 4 as illustrated in Fig. 5c.

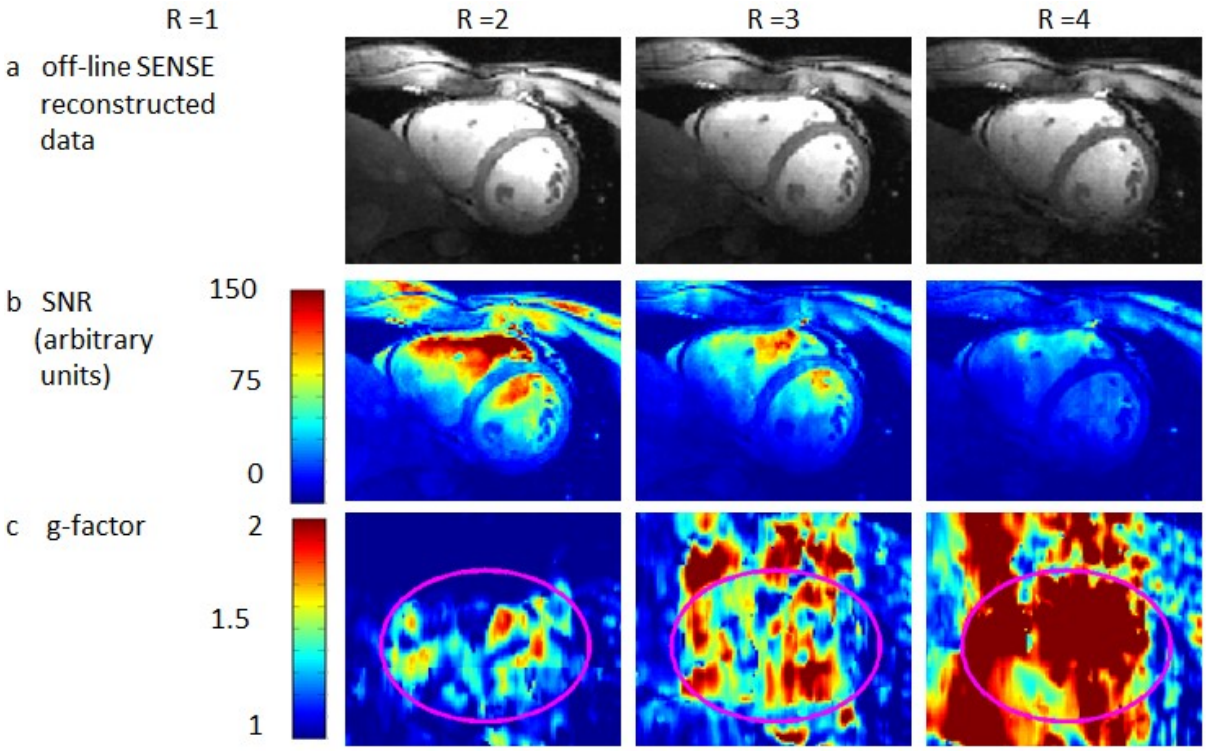

Figure 30: ***(a)*** *2D CINE FLASH images of a midventricular short axis view at diastole (in-plane resolution 1 mm × 1 mm) using decimation factors R = 2, R= 3, and R=4 together with off-line SENSE reconstruction.* ***(b)*** *Quantitative SNR maps of the data sets shown in* ***(a)****.* ***(c)*** *g-Factor-maps derived from data sets shown in* ***(d)****.*

For comparison SENSE reconstructed images are shown in Fig. 5d using the same net acceleration factors R = 2, R = 3 and R = 4 used for GRAPPA reconstruction. The quantitative SNR maps (Fig. 5e) revealed mean SNR across the myocardium of 26 for R = 2, 21 for R = 3, 12 for R = 4. For SENSE reconstruction a mean blood/myocardium contrast of 47 for R = 2, 30 for R = 3 and 14 for R = 4 was observed. The examination of SENSE g-factors for a ROI covering the short axis view of the heart yielded mean g-factor values of g = 1.26 ± 0.21 for R = 2, g = 1.51 ± 0.26 for R = 3 and g = 2.18±0.52 for R = 4 as illustrated in Fig. 5f

4.3 16-channel transceiver loop array for cardiac MRI

The results of the eight channel array showed a good image quality sufficient for clinical use. Nevertheless limitations in the degrees of freedom for transmit field homogeneity adjustment and parallel imaging capabilities were recognized. The basic loop design together with the shared conductor decoupling approach was analogously applied to a two-dimensional design. For head imaging the advantages of an element distribution in the head-feet direction for B1 efficiency was already reported [13].

Parts of the work based on the sixteen-channel transceiver array using loop elements were published in a peer-reviewed journal [126].

Following the design considerations of the eight-channel loop array resulted in an element size of (6 x 13) cm², a conductor width of 2 cm and a distance between the loop structure and the RF shield of 2 cm. The hardware results are surveyed in Figure 31, the in-vivo parallel imaging is shown in Figure 32.

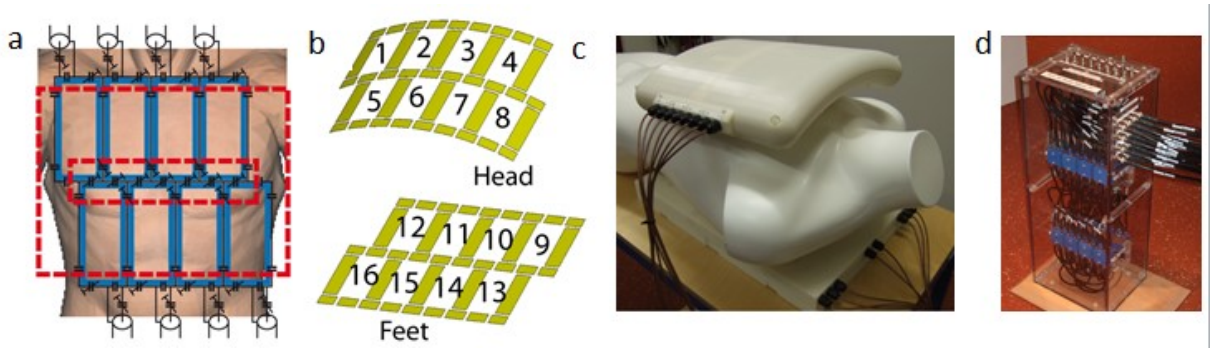

Figure 31: ***(a)*** *Loop conductor layout (blue) together with the outline of the RF shield (dotted in red) of the anterior part.* ***(b)*** *The numbering of the sixteen elements.* ***(c)*** *The complete array placed on a mannequin.* ***(d)*** *The butler-matrix used for power division into sixteen equal intensity signal and RF shimming based on circular polarized modes.*

In contrast to the eight-channel array the transmit phase settings were chosen in a circular polarized manner. By means of a 16 channel butler matrix [127] the signal is divided into sixteen equal intensity signals with phase increments of 360/16=22.5°. As the geometry of the array is not circular, an empirical determined phase shift of 80° was employed for transmit field homogeneity.

Channel	1	2	3	4	5	6	7	8
phase °	0	45	90	135	22.5	67.5	112.5	157.5
Channel	9	10	11	12	13	14	15	16
phase °	102	147	192	237	124.5	169.5	214.5	259.5

Table 5 *Transmission phases used in the in-vivo study for homogeneous excitation with the sixteen channel transceiver loop array.*

In vivo cardiac imaging was performed using a 2D CINE spoiled gradient echo (FLASH) sequence (breathhold scan, TE = 2.8 msec, TR = 5.4 msec, slice thickness 4 mm, in-plane resolution of (1.4 x 1.4) mm², receiver bandwidth 444 Hz/pixel, 30 phases per cardiac cycle, 8 views per segment).

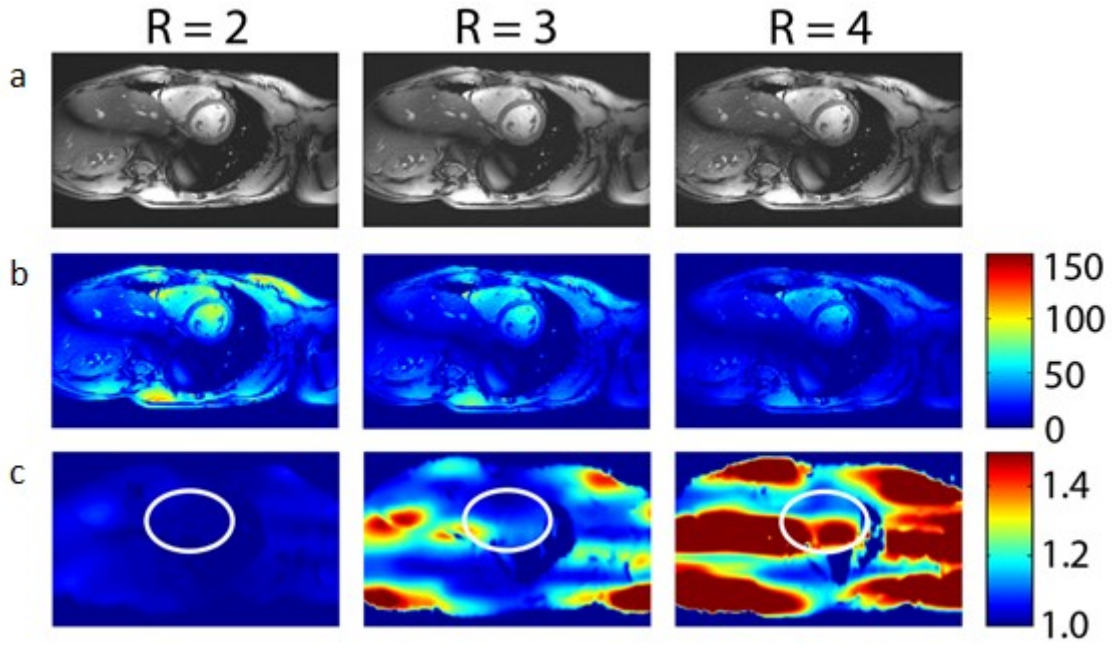

Figure 32: ***(a)*** *2D CINE FLASH images of a mid-ventricular short-axis view at diastole with an in-plane resolution of (1.4 x 1.4) mm² and a slice thickness of 4 mm. Parallel imaging using GRAPPA together with reduction factors of, R= 2, R = 3, and R = 4 was performed.* ***(b)*** *SNR maps derived from the acquisitions in* ***(a)****. For the left ventricular blood pool SNR values of 72 for R=2, 52 for R03 and 40 for R=4 were determined.* ***(c)*** *G-factor maps derived from the SNR datasets. For the elliptical ROI depicted in white mean g-factors of 1.1 for R=2, 1.57 for R=3 and 2.33 for R=4 were found.*

4.3.1 Assessment of the right ventricle of the human heart

Function and morphology of the right ventricle (RV) is of importance in the clinical assessment of cardiac disorders. The clinical standard is CMR at 1.5T using steady state free precession (SSFP) imaging. It has become the gold standard for RV chamber quantification and assessment of even small wall motion abnormalities. CMR at 7T is promising to overcome existing limitations in spatial resolution. Therefore the sixteen-channel array was used in a pre-clinical study by Knobelsdorff et.al. [128] to examine the feasibility of cine imaging at 7T for RV assessment. Nine healthy volunteers underwent CMR imaging at 7T and 1.5T with a voxel size of (1.2x1.2x6) mm3. SSFP cine imaging at 1.5T and fast gradient echo (FGRE) at 7.0 T were used. All scans provided diagnostic image quality. Overall image

quality and image contrast of transverse RV views were rated equally for SSFP at 1.5T and FGRE at 7T, while FGRE at 7T provided significantly lower image homogeneity compared to SSFP at 1.5T. The achieved image quality as well as the results for RV volumes, mass and function were comparable to SSFP at 1.5T. The study demonstrated the feasibility of RV assessment at 7T and forms a basis for further investigations if enhanced spatial resolutions is adding clinical benefit.

4.3.2 Comparison of 4, 8 and 16 channel loop coil arrays

Besides the pre-clinical RV study the eight and sixteen channel loop arrays together with a four channel loop array [11] were evaluated for CMR at 7.0T in terms of clinical image quality und parallel imaging capabilities by Winter et.al. [129]. 10 subjects (7 male, 3 female, BMI range 18.4-26.8, age 24-38 years) were included in the study. For the 8 and 16 channel array all image sets were rated to be diagnostic. While mean SNR values across the heart was found to be highest for the eight channel array, parallel imaging capabilities revealed the additional value of an increased number of channels. For a mid-ventricular short axis acquisition using GRAPPA acceleration the g-factors are summarized in Table 6.

array	R=2	R=3	R=4
4 channel	1.35±0.20	2.92±0.79	3.85±0.85
8 channel	1.19±0.13	2.08±0.39	3.41±0.35
16 channel	1.10±0.07	1.57±0.24	2.33±0.5

Table 6: *G-factor assessment using the 4, 8 and 16 channel loop arrays together with GRAPPA acceleration factors of 2, 3 and 4.*

4.4 16-channel transceiver dipole array for cardiac MRI

Recent publications introduced dipole antennas as an alternative approach to provide uniform B_1^+ field distribution and to improve transmit efficiency in the short wavelength regime for deeply located regions of interest [130, 131]. Moreover the transmit field pattern is reported to be more symmetric compared to loop antennas, which is regarded beneficial for transmission field shimming. Also from a theoretical point of view dipole antennas are a promising alternative at ultrahigh field MRI. Simulations of ideal current patterns [46] revealed that for

low magnetic field strength loop currents reassemble the ideal current pattern very well. At ultrahigh field strength above 7.0 T the ideal current pattern approaches the intrinsic curl-free current pattern of a dipole antenna. The magnetic field strength of 7.0 T is right at the intersection. Having realized the capabilities of two-dimensional arrays with the 16-channel loop array together with the different characteristics of radiative elements a 16-channel transceiver dipole array was built and its applicability for UHF-CMR was examined in a volunteer study.

Parts of the work based on the 16-channel dipole array were published in peer-reviewed conference proceedings [159] and journals [160].

For the dipole elements a building block with the dimensions (w, l, h) 75x155 x40 mm was used [131]. The box is filled with Deuterium oxide (D2O) (εr=81, σ=0.02S/m) to shorten the length of the dipole, while exhibiting low losses and negligible spin excitation at 297MHz. The Dipole structure is laid out in a Bowtie shape, as illustrated in Figure 33. Bow-tie shaped dipoles exhibit a more broadband resonance characteristic compared to rod-shaped dipoles [48], leading to reasonable resonance behavior in variable situations during in-vivo application. The 16 elements are placed in two rings around the upper torso, in close agreement to the simulation setup shown in Figure 33.

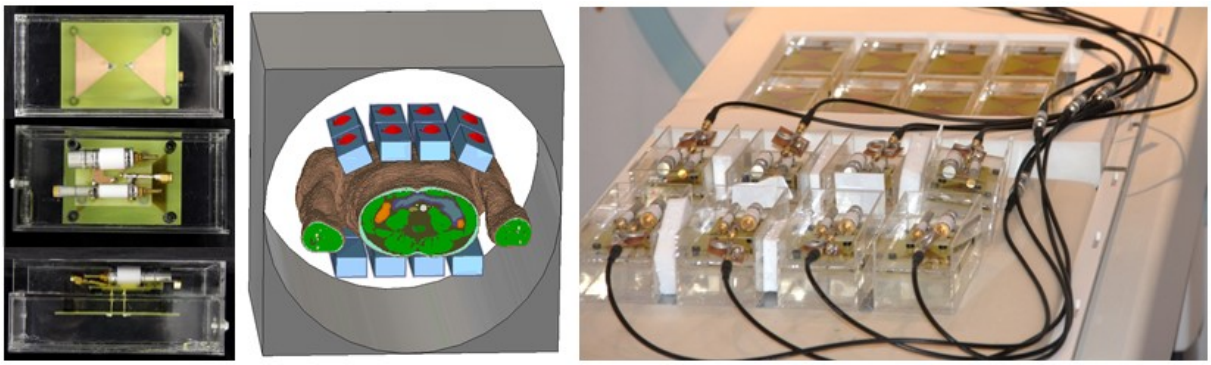

Figure 33: *Bottom, top and side view of a dipole building block, showing the water bolus, the bow-tie shaped legs of the dipole and the variable capacitors on top (left). The 16 elements in the simulation setup around the upper torso of the voxel model Duke (middle). The dipole array placed on the patient table (right). The posterior elements are incorporated in the patient table cushion, while the anterior elements are linked with fabric tape to closely fit to the upper torso.*

4.4.1 Characterization of RF performance

RF characteristics were measured for five subjects (4male, 1female; BMI 19 – 24) without subject-specific tuning and matching. Measured over all subjects and elements reflection coefficients of -19±7 dB were observed, coupling was always below -13 dB, proving the RF characteristics being sufficiently subject independent for the regarded BMI range.

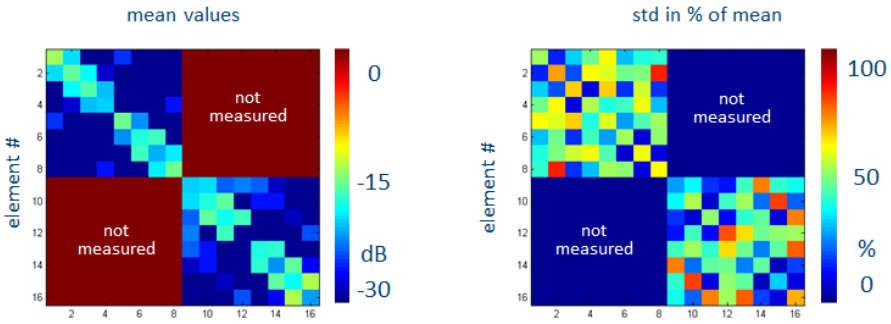

Figure 34: *Mean and standard deviation of the S-parameter matrix measured on five subjects. The results support the validity of the no-tune no-match strategy during the in-vivo study.*

4.4.2 EM simulations and transmit field shaping

Electro-magnetic field and SAR simulations were performed using CST Studio Suite 2012 together with the voxel models Duke and Ella. Based on the simulation of the voxel model Duke transmission field shaping was conducted. For this purpose the simulation results together with the material property matrices were extracted and interpolated to a isotropic resolution of 4 mm. The heart tissue pixels of the voxel model were used to mask the region and slices used for phase setting adjustments and B_1^+ optimization in MATLAB. The Matlab implementation of the Levenberg-Marquardt algorithm was used to solve the nonlinear optimization problem of computing the optimal phase setting for B_1^+ efficiency, based on simulated absolute B_1^+ maps. The merit function was chosen to minimize the pixel wise squared deviation from the sum of squares of the individual B_1^+ fields of the elements. With this numerical approach, the slice-by-slice (4mm slice thickness) B_1^+ transmission field performance of the dipole array was examined.

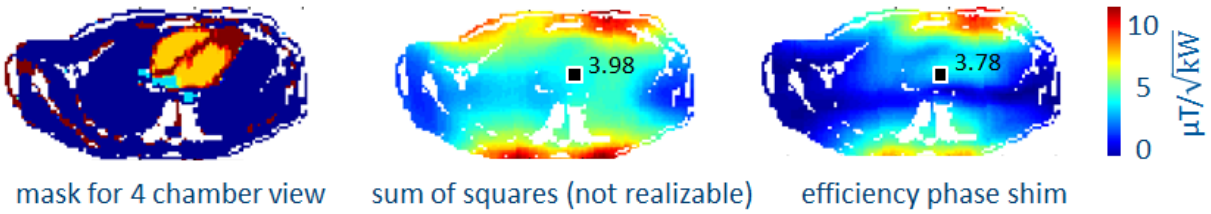

Figure 35: *Results of the $\boldsymbol{B_1^+}$ shimming using phase variation of the individual channels based on a slice through the simulation domain mimicking a four chamber view.* ***(a)*** *A clamped depiction of the slice through the density matrix serving as a mask for delineation of the pixels included in the optimization.****(b)****The sum of squares combination of the individual fields gives the pixel wise maximum achievable by phase variations. As a chosen phase setting applies to all pixels, this maximum is never reached in all pixels.* ***(c)****The $\boldsymbol{B_1^+}$ field results of the optimized phase setting used for the in-vivo study. For deep lying regions of the heart the field strength is close to this theoretical maximum.*

Channel	1	2	3	4	5	6	7	8
phase °	0	-23	-353	-328	-146	-177	-132	-89
Channel	9	10	11	12	13	14	15	16
phase °	-355	-7	-28	-8	-163	-179	-100	-92

Table 7: *Transmission phases used in the in-vivo study for homogeneous excitation with the sixteen channel transceiver dipole array.*

Slice-by-slice B_1^+ efficiency optimization for a stack of short axis views of the heart revealed a very smooth phase transition, with numerous phase settings being almost identical for a set of slices as demonstrated in Figure 36. This finding is in alignment with the results of the following in-vivo study, exhibiting homogeneous excitation of the whole heart with a single phase setting.

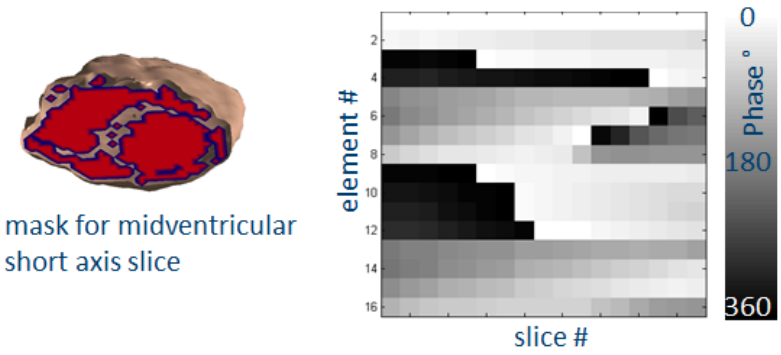

Figure 36: *Results of the slice by slice optimization of the transmit phases for efficiency. On the left an exemplary mid-ventricular slice used as a mask is depicted. In the same fashion slices covering the whole heart were optimized independently. On the right the phase results for every slice optimization and element are surveyed. Bearing in mind the phase wrap at 0°/360°, the phases show very smooth transitions when moving the region of optimization through the heart.*

For the phase setting used in the in-vivo study, see Table 7, SAR calculations were performed for both voxel models. Maximum projection plots of the localized absorption are shown in Figure 37. Maximum SAR_{10g} per input power of 0.25 1/kg for Duke and 0.31 1/kg for Ella were found. The higher value was used to calculate a permitted input power of 32 $Watt_{RMS}$ to conform with the regulatory norms concerning local SAR_{10g} in normal operation mode [81].

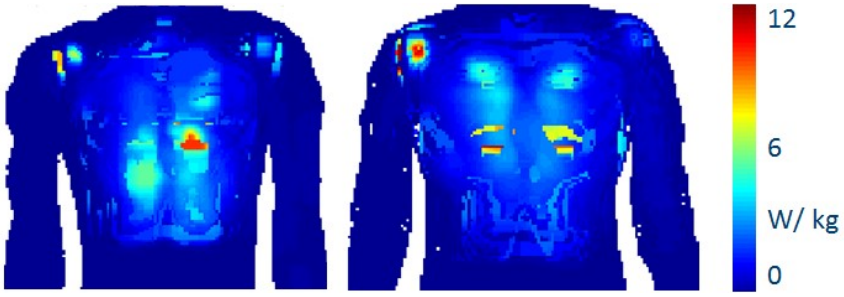

Figure 37: *Maximum projection plots of the local SAR_{10g} simulated with an accepted input Power of 40 $Watt_{RMS}$ for the male voxel model Duke (left) and the female voxel model Ella (right).*

4.4.3 In-vivo cardiac imaging

The amplifier output was split into 16 equal-intensity signals by means of home-built power splitters. Phase adjustments were implemented by phase-shifting coaxial cables. All 16 elements were connected to multipurpose transmit/receive switch boxes with integrated low-noise preamplifiers. Cardiac MR was performed in healthy subjects using single breath-hold 2D CINE FLASH in conjunction with retrospective acoustic cardiac gating without subject-

specific tuning and matching. For the in-vivo study a fixed phase setting (see Table 7) tailored for B_1^+ efficiency across a four chamber view was used.

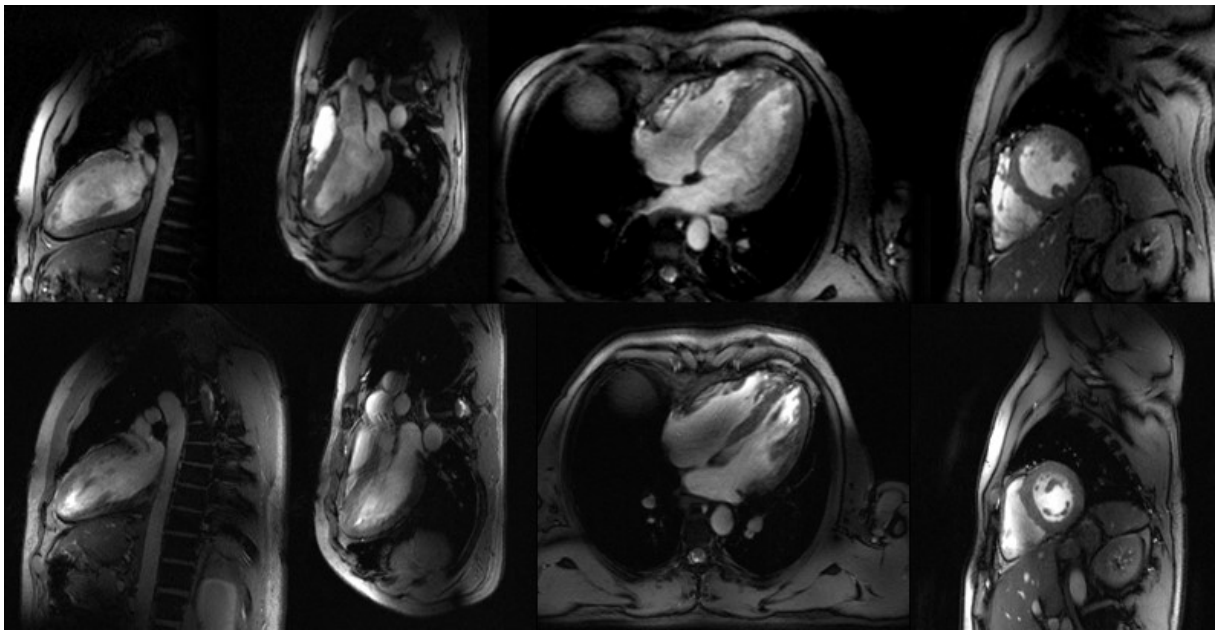

Figure 38: *Standard cardiac views covering the whole heart acquired for two volunteers (upper and lower row) using 2D CINE Flash imaging. From left to right: two-chamber view, three-chamber view, four chamber view and short axis view.*

The acquired standard views demonstrated uniform intensity across the entire heart - if not for the entire upper torso- with a high myocardium/blood contrast as illustrated in in Figure 38Figure 38: ***Standard cardiac views covering the whole heart acquired for two volunteers (upper and lower row) using 2D CINE Flash imaging. From left to right: two-chamber view, three-chamber view, four chamber view and short axis view.***. The overall image quality and the high spatial resolution of (1.4x1.4x4) mm^3 enabled the visualization of subtle anatomic structures. The deep lying lateral wall of the myocardium represents the major challenge when it comes to signal intensity. For a mid-ventricular short axis view the signal intensity curve around the myocardium is extracted, see Figure 39.

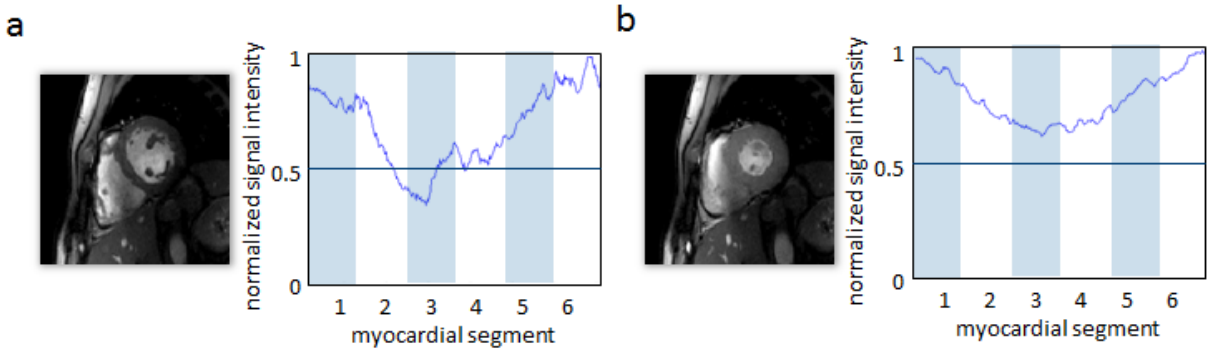

Figure 39: *Signal intensity evaluation of a mid-ventricular short axis view is diastole* ***(a)*** *and systole* ***(b)****. For diastole the signal of the lateral segment 3 was 0.34% of the septal segment. The standard deviation in percentage of the mean was 24%. For systole the lateral segment has 60% of the signal intensity of the septal segment and the standard deviation in percentage of the mean was found to be 14%.*

4.4.4 Facilitating dipole arrays for RF hyperthermia

The dipole building blocks facilitated for the 16-channel cardio array were initially proposed for a hybrid approach of RF hyperthermia guided by MR imaging [131]. A simulation study ranging from 64 MHz, the proton resonance frequency at 1.5 T, to 600MHz, the proton resonance frequency at 14.0 T was conducted to study the intended and focused RF heating inherent in any RF application to human tissue. While in MR imaging focused RF absorption is regarded as a potential safety hazard, it can be used for localized drug or contrast agent delivery [132,133] if controlled and adjusted properly. For prove of principle a phantom study at 7.0 T showed the validity of the simulated results.

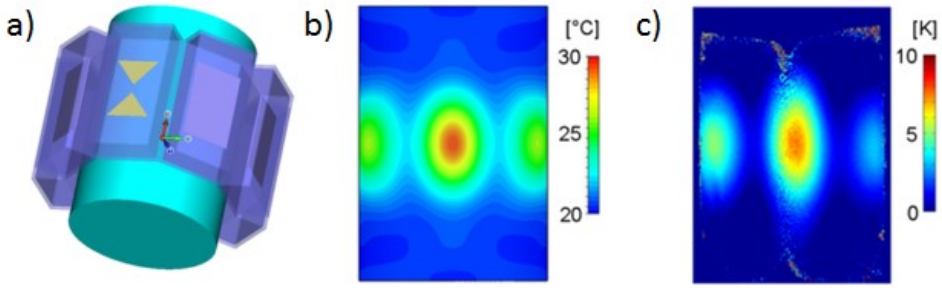

Figure 40: *Summary of the results of temperature distributions derived from EMF simulations using an 8 channel applicator together with a cylindrical phantom at a frequency of 298 MHz.* ***(a)*** *The RF heating setup consisting of eight dipole elements placed around a cylindrical phantom in the EMF simulation domain.* ***(b)*** *Results of the temperature simulation* ***(c)*** *Result of the temperature measurement in the phantom based on MR thermometry.*

4.5 Modular RF transceiver building block for ultrahigh field MRI

The results of the eight and sixteen channel arrays for CMR support the expected improvements in parallel imaging capabilities and enhanced transmission field homogeneity adjustments with an increased number of transceiver channels. Straight forward up scaling of the number of elements in the head-feet direction in the principle design of the sixteen channel loop array is not possible, as every loop elements asks for an independent feeding point. Practical observations during the in-vivo studies of the eight- and sixteen channel arrays also revealed suboptimal filling and inconsistent loading conditions of the elements due to the rigid casings of the complete anterior and posterior parts on different body geometries. Both problems can be overcome by introducing a modular concept consisting of several modules comprising four loop elements each. With the realization of a set of eight modules cardiac imaging using 32 channels, spine imaging using 16 channels and shoulder imaging using 12 channels was conducted in in-vivo pilot studies.

Parts of the work based on modular RF transceiver building blocks outlined in the following chapters 4.5 – 4.9 were published in peer-reviewed journals [64] and peer-reviewed conference proceedings [134–136].

4.5.1 Building block design considerations and realization

The modular design is proposed to assemble multichannel transceiver arrays with the key requirement that building blocks geometrically fit next to each other in two dimensions. Each module comprises 4 independent transceiver loop elements arranged in a 2×2 array. Loop elements were designed in a rectangular shape to apply the decoupling scheme successfully used in the eight and sixteen channel arrays. Adjacent elements inside a building block share a common conductor with an adjustable capacitor for decoupling as highlighted in Figure 42b. Arranging the rows in an interleaved fashion instead of a rectangular design allows for an additional shared capacitor between element two and three. This approach facilitates adjustable decoupling of three out of the four elements of the building block. Element 1 and 4 are decoupled by maximizing the distance between these elements. For this purpose the rows are shifted by approximately one loop diameter as far as the basic interleaved design allows. Inter-module coupling is suppressed by a distance of 3 cm between neighboring loop structures which was accomplished by the geometry of the coil casings, Figure 42c. The dimensions of the individual elements were chosen with respect to the anatomic coverage of the upper torso and the maximum number of 32 receive channels of a state of the art MR

system. Electromagnetic simulations as well as preliminary workbench tests were conducted to estimate how dense the loop elements can be reasonably packed with respect to coil sensitivity, quality factor and element decoupling. Figure 41surveys the results of a bench test. Rectangular loops with different sizes were evaluated regarding their q-factor ratio, as introduced in chapter 3.1.4, when placed centrally on the human upper torso.

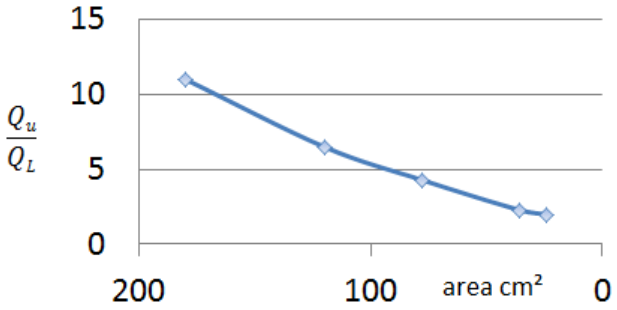

loop size cm	area cm²	Qunloaded/ Qloaded	SNR Degradation
6x4	24	2.0	30 %
6x6	36	2.2	25 %
6x13	78	4.3	12 %
6x20	120	6.5	8 %
9x20	180	11	4 %

Figure 41: *Influence of the loop size on SNR degradation. When coil losses start to dominate over sample losses, the SNR gain inherent to multi-element reception is diminished by the SNR degradation of the single elements too small in size.*

Limiting the SNR degradation to 25% and aiming at a complete, but not exaggerated coverage of the upper torso a loop size of (6 x 6) cm² was chosen as illustrated in Figure 42a. Previously reported transceiver loop arrays use 2 cm conductor width [11,122,126] to reduce ohmic losses. Here we use loop elements which are substantially smaller. Consequently a conductor width of 1 cm was chosen to balance the competing constraints of the conductor width and the loop area.

For patient safety reasons and to avoid excessive local SAR induced by E-fields in the vicinity of the conductors, the casing assures a minimum distance of 1.5 cm between the conductive loop structures and any border of the casing. For the same reason, the coaxial feeding cables are covered by a 5 mm thick foam tube. An RF shield was made of slotted copper foil to mitigate eddy currents induced by fast changing gradient fields. The shape of the RF shield follows the basic contour of the conducting structure of a four element building block. The RF shield was placed at a distance of 2 cm above the conductors. This distance was chosen to reduce radiation losses of the array without increasing the total height of the coil casing geometry beyond what is clinically acceptable and without impairing the field distribution of the loop elements.

The structure shown in Figure 42a was etched from 16 µm copper on 0.5 mm FR4 substrate. The conductor thickness was chosen to more than four times the skin depth of 3.8 µm for copper at 297 MHz (28). Non-magnetic ceramic capacitors (American Technical Ceramics Inc., Huntington Station, NY, USA) and non-magnetic trim capacitors (Voltronics Inc., Denville, NJ, USA) were used for tuning, matching and subdividing the loops in short sections with regard to the wavelength. The locations of the capacitors were given by the principal decoupling scheme or were placed to maintain symmetry over all elements. Chip capacitors with a capacitance of 22 pF were used. Variable capacitors were used for all shared capacitors and tune/match capacitors. For convenience and future maintenance they were not replaced after initial tuning and matching.

Unbalanced currents on the coaxial cables were suppressed by one cable trap per channel. These were incorporated in the casing above the RF shield, see Figure 42c. The parallel resonant trap circuit is formed by a capacitor and a two-turn solenoid inductor of the feeding coaxial cable itself (18). The coil casing as well as the support structure for the RF shield were made from ABS+ material using a rapid prototyping system (BST 1200es, Dimension Inc., Eden Prairie, MN, USA). The coil casing is designed to accommodate and fix all components of the building block and also implements the curvature with a radius of 17.5 cm for the modules intended for anterior use. The design was developed with the CAD software Autodesk Inventor 2010 (Autodesk Inc., San Rafael, CA, USA). The tailored casing design resulted in lightweight modules of less than 400 g weight per module.

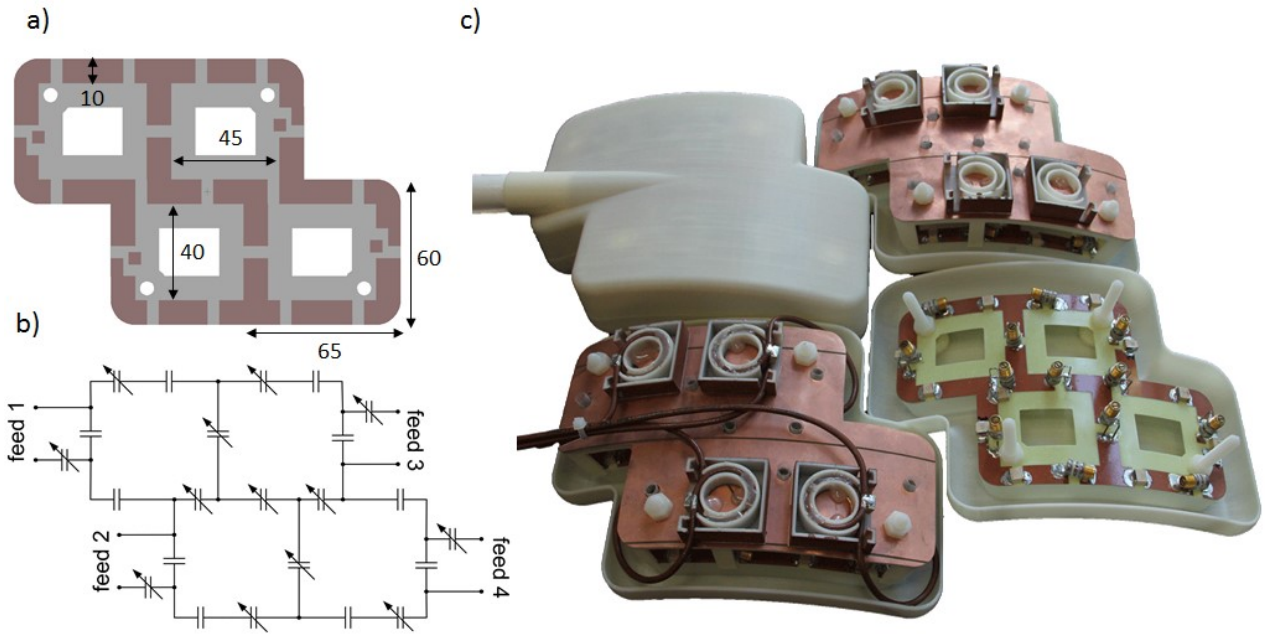

Figure 42: *Design and realization of one module comprising four loop elements.* ***(a)*** *Technical drawing used for fabrication of the printed circuit board (PCB) with the conducting copper structure. Dimensions are given in mm.* ***(b)*** *Placement of the capacitors and signal feeding points. The capacitors highlighted in red are adjustable to fine-tune the decoupling of the neighboring elements.* ***(c)*** *The hardware realization of a module in different stages of construction. The casing provides the support structure for the PCB. Another support structure fixes the RF shield in place. On top of the RF shield, shielded from the loop elements, the cable traps are placed. Finally a Lid encapsulates the module and leads the connection cables through a foam tube of a length of one meter.*

4.5.2 EMF simulations and validation

A phantom setup consisting of one curved building block placed on a cylindrical phantom was used to validate the coil model of the EM field simulations. For this purpose, the cylindrical phantom (radius = 90 mm, length = 250 mm) was filled with a dielectric gel (εr = 57.8, σ = 0.78 S/ m). Absolute B_1^+ distributions of the individual coil elements derived from the EMF simulations were compared to maps of absolute B_1^+ values derived from measurements. For the transversal slices depicted in Figure 43 RF transmission field mapping was conducted using a Bloch-Siegert implementation (32) (TR = 100 ms, Fermi pulse, off-center frequency: 4 kHz, scan time: 13 s). The sequence employed double gradient echo acquisitions with echo times TE1 = 8 ms and TE2 = 11 ms to enable B_0 mapping (33). Volume selective second order B_0 shimming was performed. B_1^+ mapping was done offline using Bloch simulations in Matlab (MathWorks, Natick, MA, USA) considering B_0 nonuniformities. All absolute values were normalized to the root mean square value of the input power at the feeding point of the loop structure. The resolution of the measured maps was adapted by interpolation to match the

resolution of the measured B_1^+ maps. For the pixel-by-pixel difference maps presented in Figure 43 d regions with measured values of less than 5 µT/sqrt(kW) were omitted.

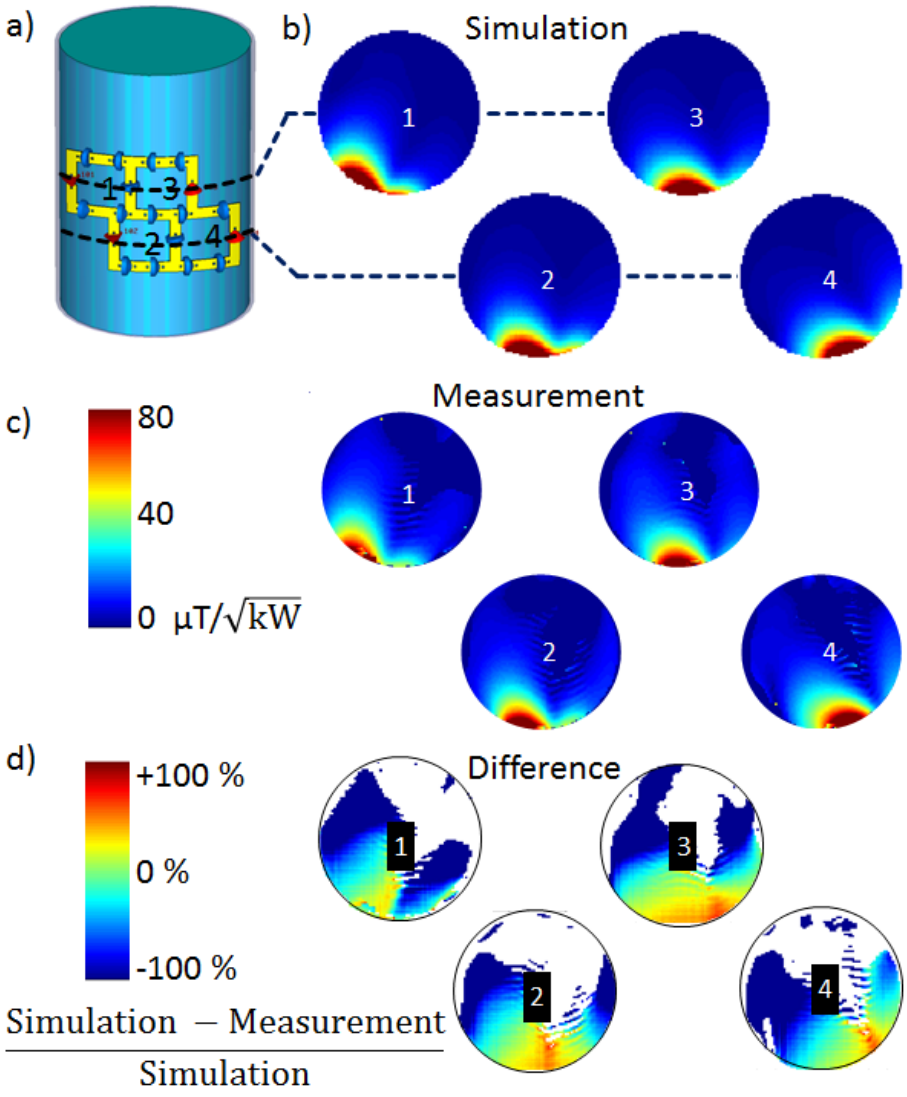

Figure 43: *Comparison of simulated and measured transmission fields using a cylindrical phantom setup* [64]. ***(a)*** *Simulation model of the setup used for validation. RF shield and casing are not shown but are included in the simulation. The experimental setup was arranged analogously to the virtual setup.* ***(b)*** *Simulated B1þ distribution (absolute values) of four channels that form one curved building block. For* $\boldsymbol{B_1^+}$ *evaluation, transversal slices through the cylindrical phantom were positioned in alignment with the center of the loop elements.* ***(c)*** *Absolute transmission fields derived from* $\boldsymbol{B_1^+}$ *mapping of the experimental setup.* ***(d)*** *Pixel-by-pixel difference maps in percentage of the simulated results. The results demonstrate the qualitative and quantitative agreement between the numerical simulations and the measurements.*

The transmission fields obtained from EM simulations of individual coil elements placed on the virtual cylindrical phantom were found to be in good quantitative and qualitative agreement with the B_1^+ fields derived from B_1^+ mapping in phantom experiments as illustrated

in Figure 43 for a building block. The absolute differences for a circular ROI covering the axial view of the phantom were (-2.5 ± 4.6) µT for element 1, (0.16 ± 5.5) µT for element 2, (0.2 ± 7.6) µT for element 3 and (-1.7 ± 4.5) µT for element 4. Percental difference maps are presented in Figure 3d, which demonstrate the validity of the coil model and support the credibility of the SAR simulations. For a circular ROI covering the axial view of the phantom the mean B_1^+ value of the simulation was found to be -32 % compared to the measurement for element 1, -1 % for element 2, +1 % for element 3 and -20 % for element 4. Mean B_1^+ values derived from regions defined by the 80 % isoline of B_1^+ (max,simulations) were found to be +5 % compared to the phantom experiments for element 1, +27 % for element 2, +40 % for element 3 and +19 % for element 4. Thus the simulation shows higher B_1^+ in the vicinity of the elements, whereas the measurements exhibit relatively higher B_1^+ in deeper lying regions of the phantom.

4.6 Modular 32-channel transceiver array for cardiac MRI

Transceiver arrays for cardiac imaging ask for a layout that closely conforms to the upper torso while not impairing patient comfort and respiration. To constitute the proposed cardiac array of 32 independent transmit- and receive channels four planar building block modules were combined to form the posterior coil section. Four modestly bent modules were used to form the anterior coil section as depicted in Figure 44b-e. The curvature radius is 17.5 cm. The anterior modules are fixed by fabric hook-and-loop fasteners added to elastic strips. This approach provides a flexible connection between building blocks that allows the four modules to tilt at the building block interfaces while closely fitting to any upper torso geometry regardless of gender or BMI, as can be appreciated in Figure 44e. The posterior modules were integrated into the patient table cushion so that no extra free magnet bore space was consumed by the posterior section.

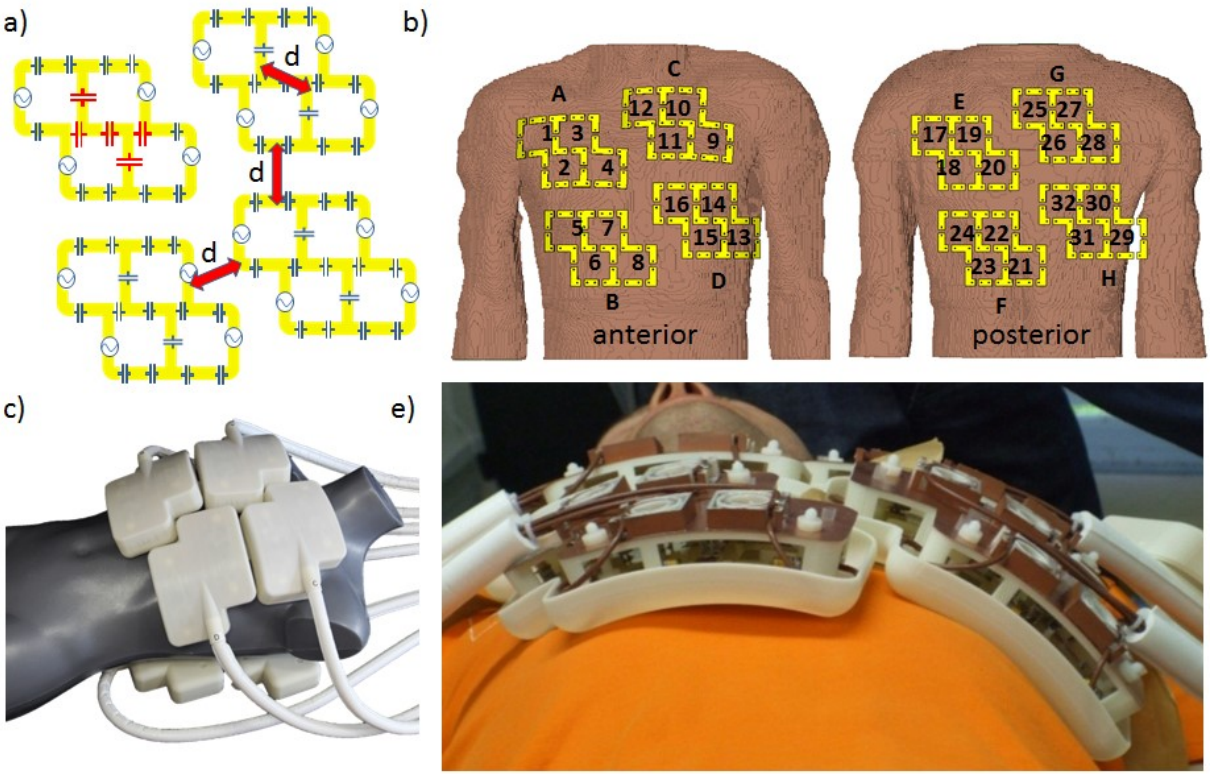

Figure 44: *Constitution of a 32 channel cardiac array based on four 4 channel transceiver modules* [64]. ***(a)*** *Basic loop structure and capacitor placement for the anterior section of the array. The applied decoupling schemes are emphasized in red. Neighboring elements are decoupled by a shared capacitor. All other elements are decoupled by a distance d.* ***(b)*** *The element nomenclature (numbers 1–32) and the block nomenclature (letters A-H) used throughout the 32channel study.* ***(c)*** *The complete cardiac array placed on a mannequin.* ***(e)*** *The elements closely fitting to the upper torso of a volunteer.*

The modules are lightweight (m < 400 g per module) and conform to a broad range of upper torso geometries. Any localized mechanical pressure is averted due to flexible module intersections. This leads to well perceived, gender-independent patient comfort and easy handling of the 32 local transceiver channels. With a height of 47 mm the building blocks consume minor space in the effective magnet bore which enables CMR of subjects covering an ample BMI range.

4.6.1 EM simulation and transmission field shaping

EM and SAR simulations were performed using CST Studio Suite 2011 (CST AG, Darmstadt, Germany) together with human voxel models Duke (BMI: 23.1) and Ella (BMI: 22) . For the EM simulations the building blocks were modeled with the RF shield and the entire casing. This enabled the emulation of the in-vivo situation by using oblique building block positions tailored to the shape of the human voxel model's upper torso. This approach assures correct

distances between building blocks and between the conductor structure and the voxel model. The simulations included the RF shield of the gradient coils. The voxel models were truncated at the neck and at the hips as displayed in Figure 44 b, allowing for a high resolution mesh in the target region. The double-oblique placement of the large number of curved loop elements challenged the mesh generation and required a mesh resolution of 1 mm isotropic in these areas. The voxel model was meshed with a resolution of 2 mm isotropic. Decoupling capacitors were incorporated in the EMF simulations and were adjusted iteratively. The feeding points of the elements were modeled as 50 Ω ports. Final field results were accomplished incorporating lumped tuning and matching capacitors in the built-in circuit simulator of CST Studio Suite (CST Design Studio), following the workflow proposed in [77]. The capacitor values were optimized with respect to the S-parameter simulation and were used as a starting point for the practical realization. For the final configuration and phase settings used in in vivo measurements the SAR values were calculated. The input power was adjusted to meet the regulations of the IEC guideline IEC 60601-2-33 Ed.3 [81].

For RF shimming the B_1^+ fields of all individual elements were extracted from the EMF simulations for slices representing the four chamber view of the voxel model's heart. Post processing applying the superposition principle was performed in Matlab to optimize and evaluate the transmit field homogeneity for three phase settings. The region of the heart was deduced from the material dataset of the voxel model. Based on this region of interest, the Matlab implementation of the Levenberg Marquardt algorithm [68] incorporated in the Optimization Toolbox (MathWorks, Natick, MA) was used to calculate excitation settings to homogenize the resulting B_1^+ field. For comparison a circular polarized (CP) like mode is used. The CP mode refers to a phase setting with each channel driven by a phase corresponding to its angular position relative to the body center in the transversal plane. As the degrees of freedom grow exponentially with the number of channels, the nonlinear solver needed to go through a reasonable large number of starting points to reproducibly find the global minimum. The merit function for the RF shimming was dynamically updated to a constant field strength equal to the median value of the intermediate result. The emphasis was put on phase shimming, which can be realized by introducing phase cables into the transmit path supplied by a single channel RF power amplifier. The applicable range of body geometries and BMI's for this simulation and hardware based B_1^+ calibration concept is centered around the predefined human voxel model used for optimization. Taking the availability of a large range of voxel models into account the full range of human subjects can be covered through the approach used in this study.

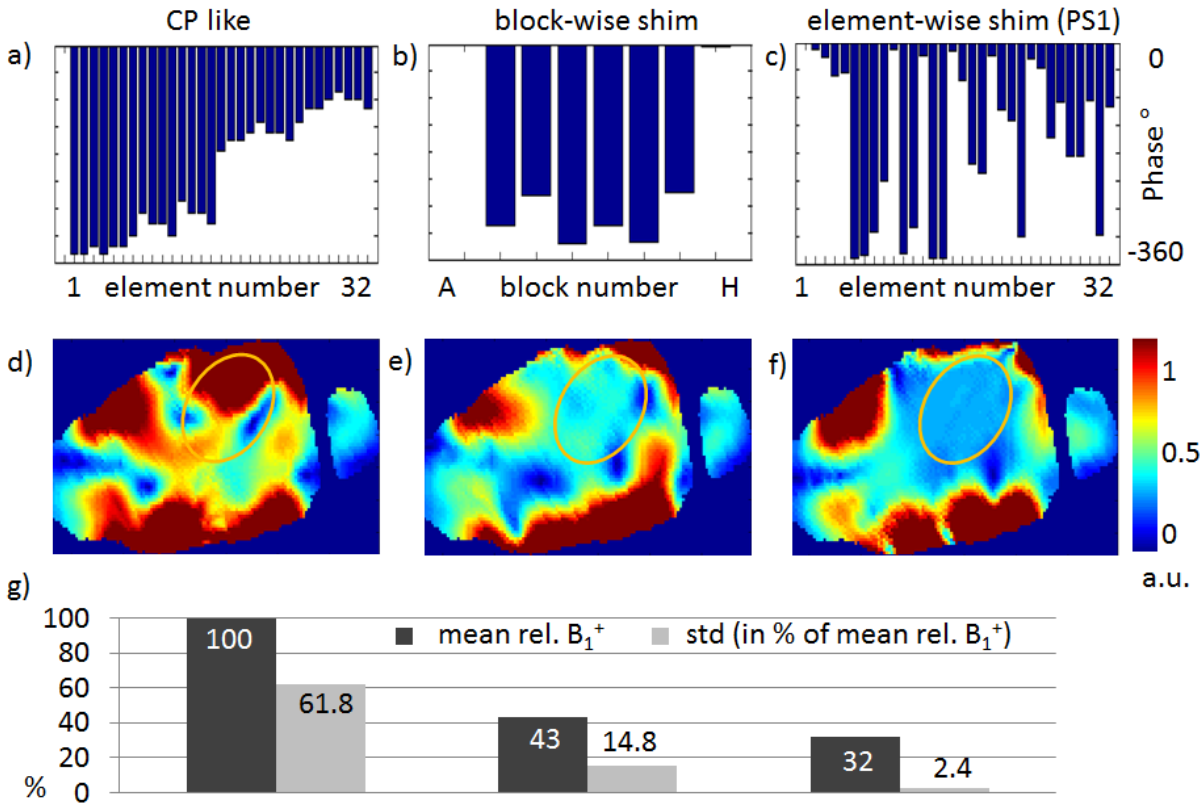

Figure 45: *Summary of the results obtained from the transmission field shaping based on simulations for a multi-oblique plane mimicking a four-chamber view* [64]. ***(a–c)*** *Phase settings for RF shimming. Left: CP mode. Middle: Block wise optimized phase setting. Right: Element wise optimized phase setting PS1. Channel-by-channel phase values used for the element-wise phase setting regimes are surveyed in Table 1.* ***(d–f)*** *Corresponding B_1^+ field distributions for the three phase setting modes. The element wise phase setting approach provided the most uniform B_1^+ fields across the heart. This performance comes at the cost of B_1^+ efficiency degradation versus the CP-like and the block wise phase shimming mode.* ***(g)*** *Statistics of the B_1^+ field inside the ROI mimicking a four-chamber view.*

Channel	1	2	3	4	5	6	7	8
phase °	0	-10	-24	-54	-48	-351	-347	-308
Channel	9	10	11	12	13	14	15	16
phase °	-225	-12	-2444	-300	-22	-351	-350	-14
Channel	9	10	11	12	13	14	15	16
phase °	-62	-192	-214	-21	-109	-127	-315	-27
Channel	9	10	11	12	13	14	15	16
phase °	-40	-154	-98	-186	-185	-94	-314	-105

Table 8: *Transmission phases used in the in-vivo study for homogeneous excitation with the 32 channel transceiver loop array.*

The phase settings derived from the optimization algorithm used for RF shimming are displayed in Figure 45b-c and numbers for PS1 used in in-vivo study are given in Table 8. The non-linear algorithm was empirically found to provide reproducible convergence for 1000 randomly chosen starting points. The CP like mode has a high mean B_1^+ value but suffers from signal voids inside the region of the heart marked by the orange ellipse in Figure 45d f. A module-wise phase optimized setting (Figure 45b), where all four loop elements of a building block exhibit the same phase, revealed an improvement in B_1^+ homogeneity at the expense of the B_1^+ efficiency which manifests itself in a reduced mean B_1^+ value as demonstrated in Figure 45g. The block-wise phase setting, which is virtually equivalent to an 8 channel transmit and 32 channel receive coil regime also showed focal signal reduction in the peripheral sections of the region covering the heart as illustrated in Figure 45e. The use of an element-wise phase adjustment PS1 (Figure 45c) improved the B_1^+ uniformity substantially as demonstrated in Figure 45f. For this phase setting mode the standard deviation of B_1^+ was found to be approximately 3% of the mean B_1^+ versus 60% obtained for the CP like mode. This improvement in the transmission field uniformity came at the cost of the B_1^+ efficiency which was approximately 30 % for the element-wise phase adjustment mode versus the CP like mode. The phase setting PS1 derived from the simulations for the four chamber view was implemented in hardware to support fast and comfortable application during the in-vivo examinations.

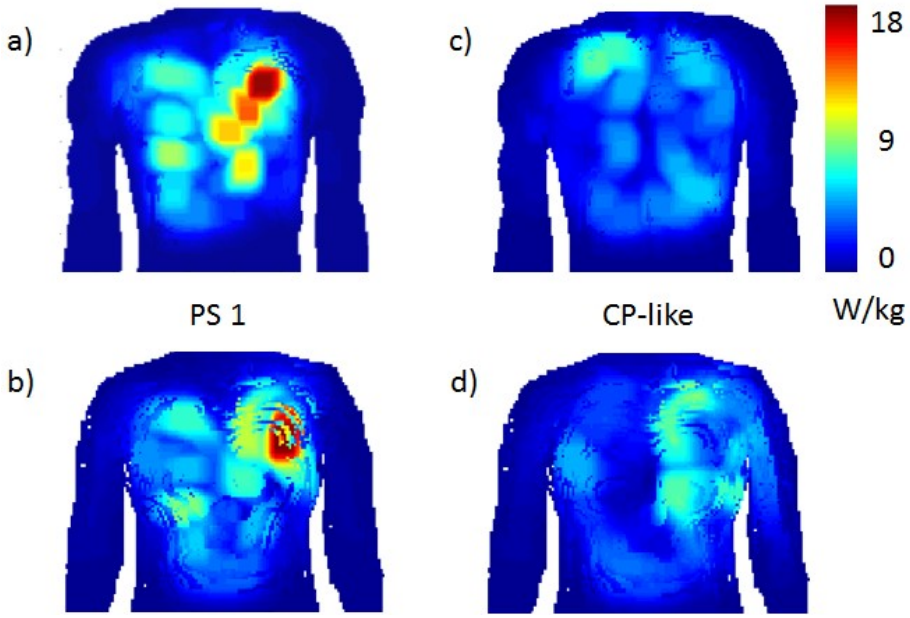

Figure 46: *SAR results derived from EM simulations of the 32-channel TX/RX cardiac array applying an input power of 20 W_{RMS}. Maximum projection plots of the local 10 g averaged SAR distribution for the male human voxel model Duke* ***(a)*** *and for the female human voxel model Ella* ***(b)*** *based on the phase setting PS1 used for in-vivo imaging. Analoguesly the maximum projection plots of the local 10 g averaged SAR distribution based on a CP-like phase settings for the male human voxel model Duke* ***(c)*** *and for the female human voxel model Ella* ***(d)*** *are shown for comparison.*

SAR values, derived from the EM simulations incorporating a male and a female voxel model were well below the limits permitted by the IEC guidelines [81] as outlined in Figure 46 for an average accepted input power of 20 W. All phase settings used in the in-vivo study were evaluated with both human voxel models, including a circular polarized mode and a phase setting (PS1) resulting from the optimization algorithm used for RF shimming. PS1 exhibited more pronounced local SAR hotspots with maximum values of 18.6 W/kg for Duke and 18.1 W/kg for Ella. For the circular polarized mode the maximum values were 8.3 W/kg for Duke and 9.0 W/kg for Ella, showing the strong influence of the phase setting on the resulting SAR value. Comparing the results of the independent simulations for both human voxel models, the distribution of the local 10 g averaged SAR values correlate very well. This indicates a reliable SAR estimation for all subjects included in the in-vivo study. The value of 0.93 1/kg SAR normalized to 1W input power was used to determine the SAR limit for all in-vivo measurements. The first and second level controlled mode given by the IEC guidelines [81]were not used in the in-vivo applications which limits the maximum local 10 g SAR to 10 W/kg and thus preserves a safety margin of factor 2.

4.6.2 Radio frequency interface and characterization

The amplifier output was split into 32 equal-amplitude signals by means of home-built power splitters compiled to a splitting cascade from 1:2, 2:8 and 8:32. For this purpose Wilkinson power splitters 1:2 and 1:4 were used in lumped element design that feature equal intensity and zero phase outputs. Phase adjustments of coil sections, individual building block modules and per single channel were implemented by phase-shifting coaxial cables incorporated in the appropriate position in the power splitting network. All 32 elements were connected to the RF system using multipurpose interface boxes with transmit/receive switches and integrated low-noise preamplifiers as introduced in chapter 3.2.3. Compatibility of the proposed coil array with a single channel system, an eight channel or ultimately with a 32 channel parallel transmission system is enabled by feeding RF into the corresponding stage of the splitting network.

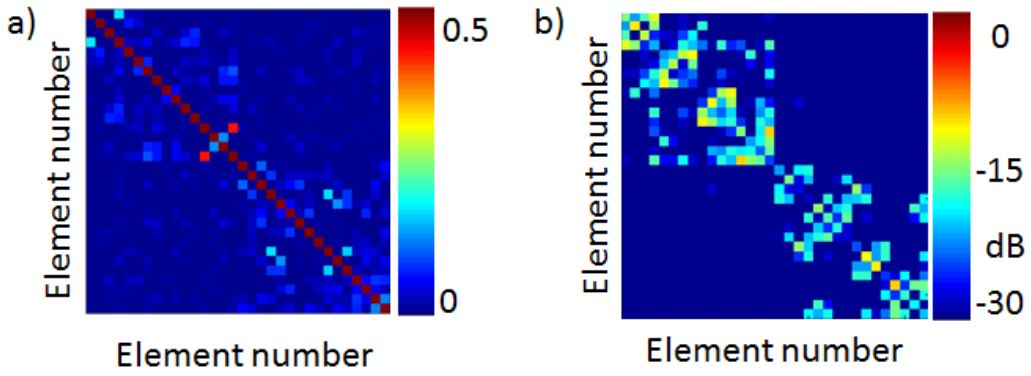

Figure 47: *Results of the RF characterisation of the 32-channel TX/RX cardiac array* ***(a)*** *Measured noise correlation matrix averaged over all subjects.* ***(b)*** *S-parameter matrix of an exemplary subject.*

The loop elements were found to have an average QU/ QL of 2.14. Exemplary values for the four loops of module A are 87, 135, 75, 61 for the unloaded case and 37, 50, 48, 32 for the loaded situation. Reflection coefficients of (21 ± 7) dB were observed. Noise correlation was 0.46 or well below for all elements and subjects as shown in Figure 47a. Element coupling was below -20 dB for any neighboring elements inside one module, i.e.A1 and A2, below -10 dB for any next-neighboring elements inside one module, i.e. A1 and A4 and below -16 dB for any neighboring elements of different modules, i.e. A4 and C11. A complete S-Parameter matrix is given in Figure 47b. The Wilkinson power splitter 1:2 introduced 0.19 dB of loss. The Wilkinson power splitters 1:4 introduced 0.53 dB of loss per stage and have a phase deviation of less than ± 5 deg. Phase cables were manufactured with less than ± 2° phase deviation. Overall losses from the system RF output to the individual coil connectors were

determined to be -3.9 dB, which were considered for the input power calculation. The overall variance for the phase adjustment was found to be less than ± 12°.

4.6.3 In-vivo cardiac imaging

The pilot study for in-vivo cardiac MR imaging included eight healthy subjects (5 male, 3 female; age: 23 - 48; BMI: 23.4 ± 2.4, heart rate: 69 ± 13 bpm). Standard cardiac views including short axis, two chamber and four chamber views were acquired using single breath-hold 2D CINE FLASH imaging. The imaging protocol was adjusted to the following parameters. TE = 3.3 ms, TR = 6.7 ms, views per segment = 6, bandwidth = 446 Hz/pixel, hamming weighted sinc RF pulse (amplitude = 218 V, duration = 1 ms, bandwidth-time product = 2.0), matrix size = 320 x 264, in-plane spatial resolution = (1.1 x 1.1) mm², slice thickness = 2.5 mm, acquisition time = 24 heartbeats. For retrospective gating [95] an MR-stethoscope (EasyACT, MRI.TOOLS GmbH, Berlin, Germany) was used to resolve the heartbeat into 25 cardiac phases. The high spatial resolution images were compared to images acquired with a spatial resolution commonly used in a standardized clinical CMR protocol [125]. The spatial resolution was altered from an in-plane resolution of (1.8 x 1.8) mm² (slice thickness = 6 mm, matrix size = 160 x 176) over an in-plane resolution of (1.4 x 1.4) mm² (slice thickness = 4 mm, matrix size = 232 x 256) to an in-plane resolution of (1.1 x 1.1) mm² (slice thickness = 2.5 mm, matrix size = 306 x 336) while keeping all other imaging parameters constant. The signal intensity profile along a circular trajectory inside the myocardium was analyzed for a mid-ventricular short axis views at end-diastole. The result was labeled using the common segmentation of the myocardium [97].

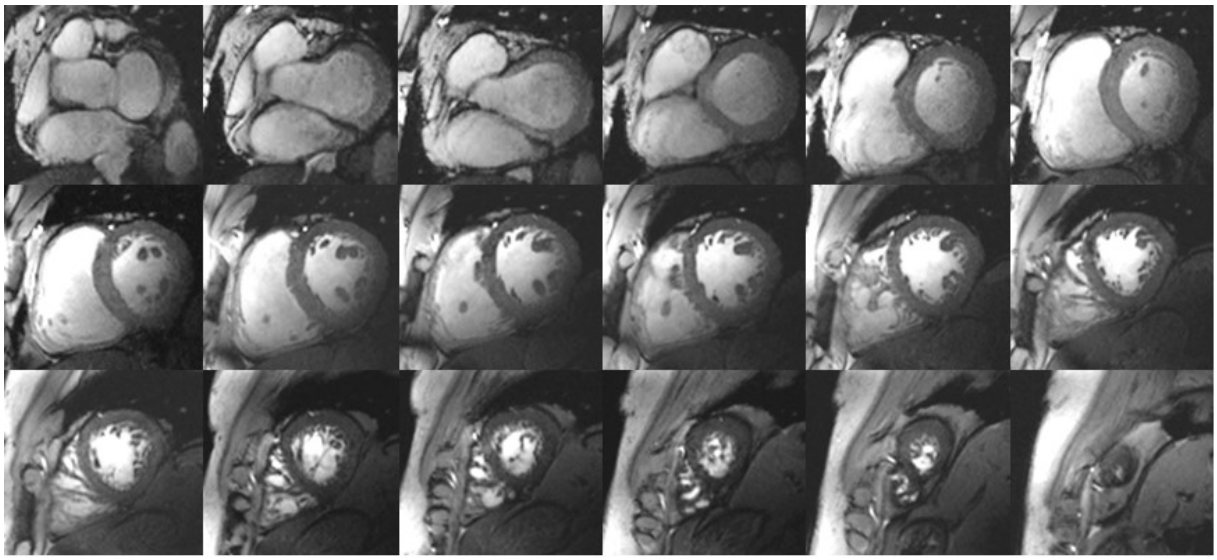

Figure 48: *A stack of short axis views covering the whole heart from the atrium to the apex. The images are derived from 2D CINE FLASH imaging with an in plane spatial resolution of (1.1 x 1.1) mm² and a slice thickness of 2.5 mm. All slices exhibit reasonable constrast without major signal voids.*

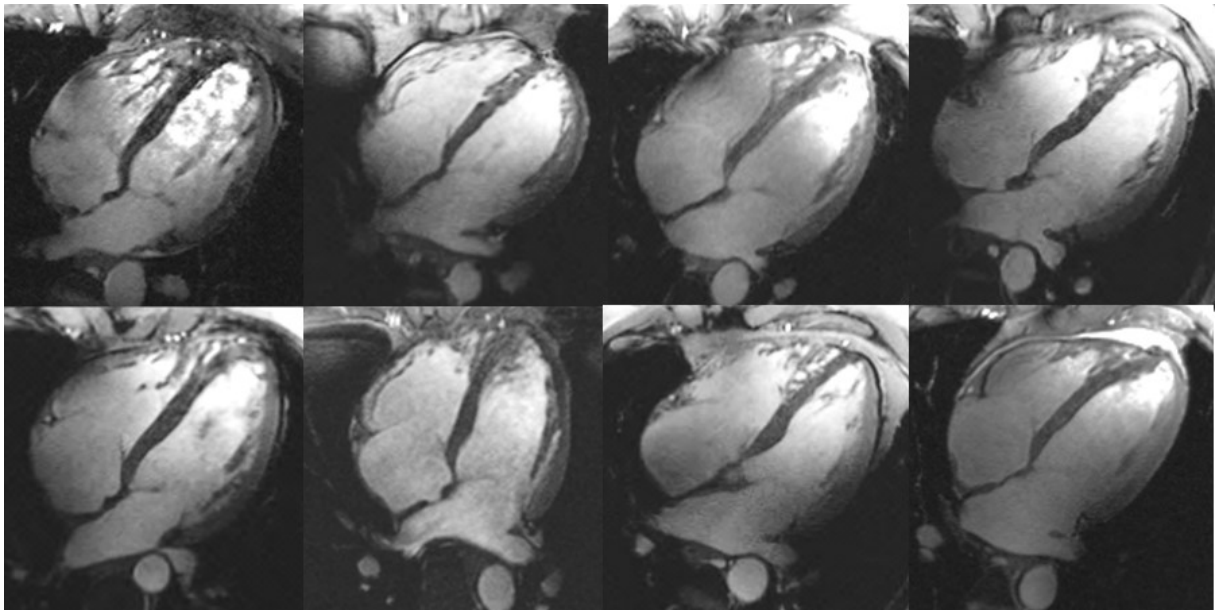

Figure 49: *Four chamber views of all eight subjects included in the study derived from 2D CINE FLASH imaging with an in plane spatial resolution of (1.1 x 1.1) mm² and a slice thickness of 2.5 mm. All images show reasobale constrast throughout the heart without major signal voids, underlining the reproducibility of the results over subjects of a limited BMI range and different gender.*

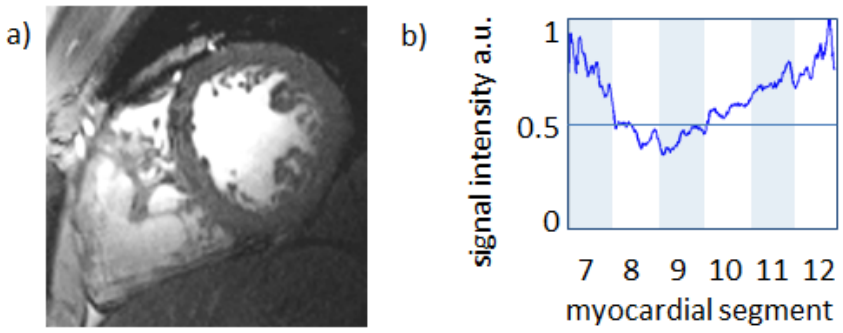

Figure 50: *Signal intensity evaluation of an exemplary mid-ventricular short axis view in end-diastole (in plane spatial resolution (1.1 x 1.1) mm² slice thickness 2.5 mm). The signal intensity was taken from a circular line following the myocardium. Lateral parts of the myocardium show an minimum signal intensity of 40% compared to the maxinum signal parts.*

2D CINE FLASH imaging using phase setting PS1 exhibited rather uniform intensity distribution over the entire heart as depicted in Figure 48 which shows a stack of short axis views covering the heart from the apex to the base. Also the image quality over all subjects included in our feasibility study was rather robust as demonstrated in Figure 49. Figure 50 gives a measure for the signal intesity vatiations along the myocardium in the short axis view. The signal intensity distribution revealed a standard deviation in percentage of the mean value over the myocardium of 24 %. These results exhibit an improvement to previously reported results for loop arrays using 4,8 and 16 transceiver channels [129]. Figure 51 illustrates the impact of the spatial resolution on the delineation of subtle anatomical details of the heart. Compared to the clinical standard the voxel volume was reduced by a factor of six, enabling the visualization of the compact layer of the free right ventricular wall and the remaining trabecular layer as well as the mitral and tricuspid valves together with their papillary muscles and trabeculae.

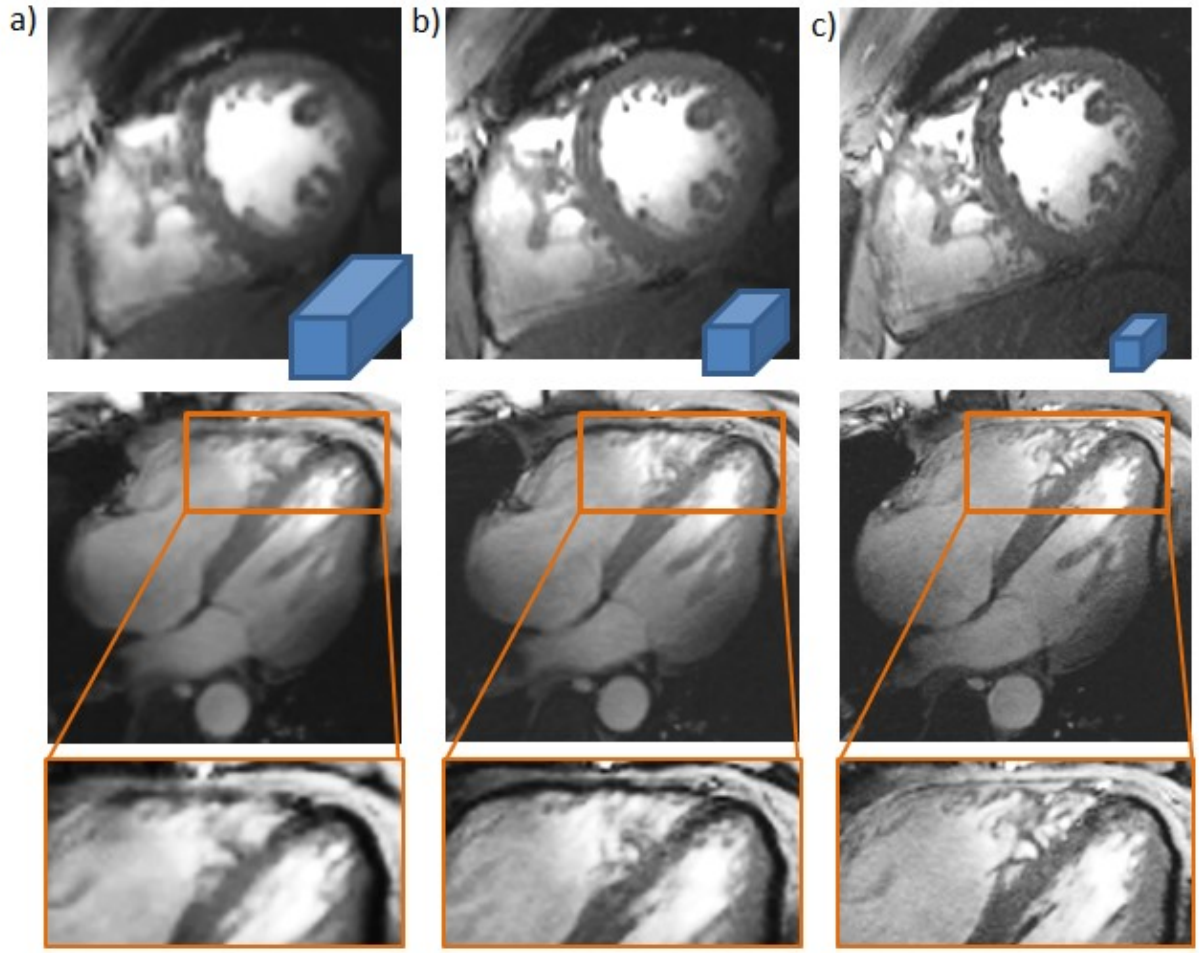

Figure 51: *Comparison of different voxel sizes in 2D CINE FLASH imaging (GRAPPA reduction factor 2, transmission phase setting PS1). The magnified voxels in blue show the relative change in voxel size.* ***(a)*** *Standardized clinical protocol with in-plane resolution of (1.8 x 1.8) mm² and 6 mm slice thickness.* ***(b)*** *In-plane resolution of (1.4 x 1.4) mm² and a slice thickness of 4 mm.* ***(c)*** *In-plane resolution of (1.1 x 1.1) mm² together with a slice thickness of 2.5 mm. These results illustrate that spatial resolution enhancements by of a factor of six versus standardized protocols used in current clinical practice improve the delineation of subtle anatomical details, as can be percived in the zoomed views of the ventricular trabeculaes in the bottom line of the figure.*

4.6.4 Parallel imaging performance

In the following the evaluation of the parallel imaging performance of the array is presented. GRAPPA (39) was used with reduction factors of up to R=6. SNR and g-factor assessment was conducted for end-diastolic four chamber views and short axis views of the heart based on SNR scaled imaging [72]. Contrast-to-noise-ratio (CNR) values were estimated by subtraction of the SNR values of the myocardium from the SNR values of the left ventricular

blood pool. SNR assessment is based on the high spatial resolution of (1.1 x 1.1 x 2.5) mm³ used for 2D CINE imaging.

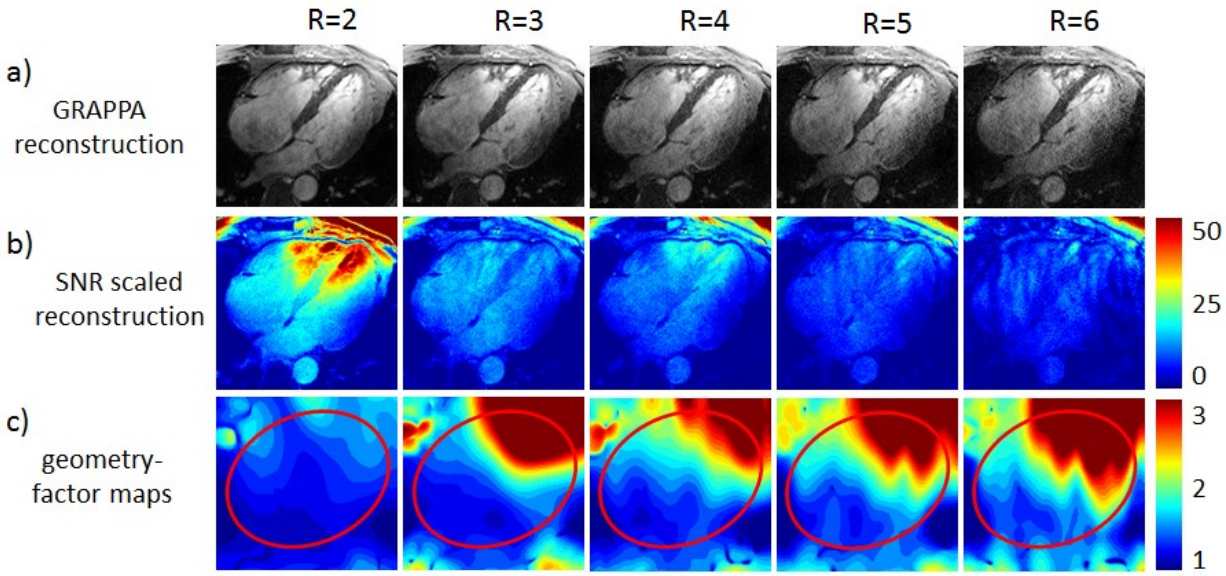

Figure 52: *Parallel imaging performance for an four chamber long axis view of the heart.* ***(a)*** *GRAPPA-reconstructed images derived from 2D FLASH CINE imaging. One-dimensional reduction factors of R=2 to 6 were used in the left-right direction.* ***(b)*** *Images scaled in SNR units for all reduction factors.* ***(c)*** *G-factor maps deduced from the SNR scaled images. The ROI depicted in red was used for statistics.*

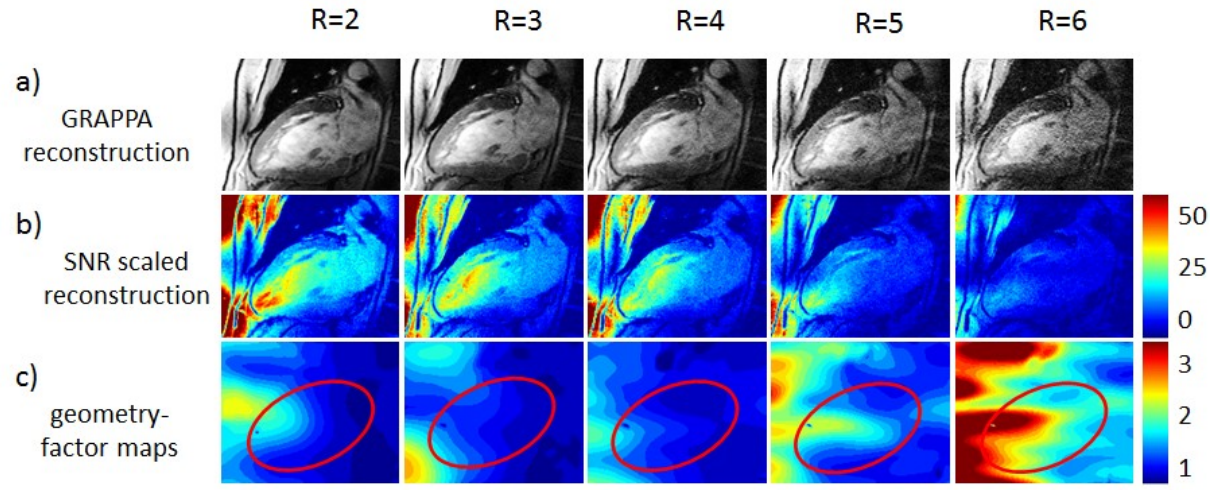

Figure 53: *Parallel imaging performance for a two chamber long axis view of the heart.* ***(a)*** *GRAPPA-reconstructed images derived from 2D FLASH CINE imaging. One-dimensional reduction factors of R=2 to 6 were used in the head-feet direction.* ***(b)*** *Images scaled in SNR units for all reduction factors.* ***(c)*** *G-factor maps deduced from the SNR scaled images. The ROI depicted in red was used for statistics.*

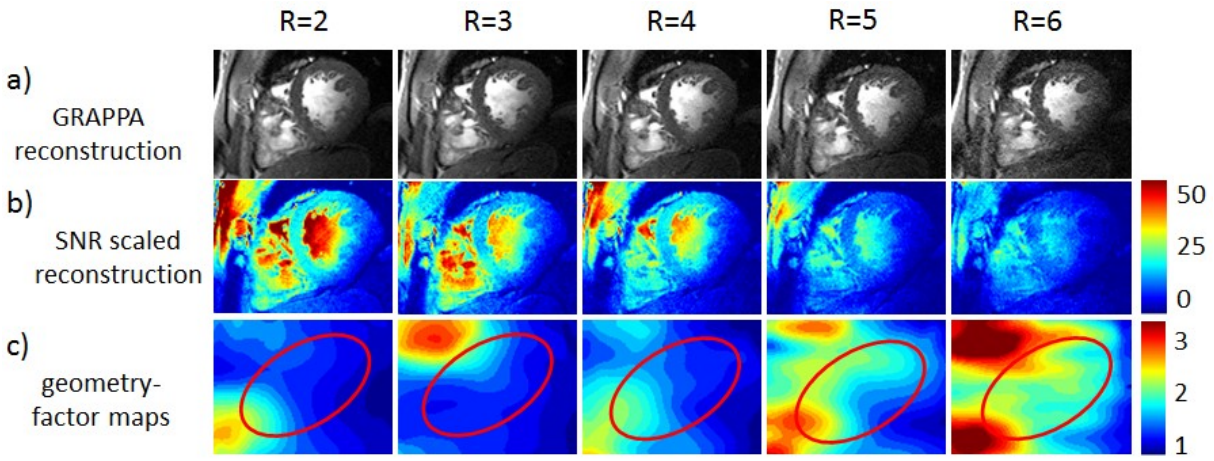

Figure 54: *Parallel imaging performance for a mid-ventricular short axis view of the heart.* ***(a)*** *GRAPPA-reconstructed images derived from 2D FLASH CINE imaging. One-dimensional reduction factors of R=2 to 6 were used in the head-feet direction.* ***(b)*** *Images scaled in SNR units for all reduction factors.* ***(c)*** *G-factor maps deduced from the SNR scaled images. The ROI depicted in red was used for statistics.*

Parallel imaging using GRAPPA accelerated 2D CINE FLASH imaging provided excellent image quality for reduction factors up to R = 4. Results together with SNR maps are depicted in Figure 52 for a four chamber view, in Figure 53 for a two chamber long axis view and in Figure 54 for a mid-ventricular short axis view of the heart. For the latter views the phase encoding direction was placed perpendicular to that used for the four chamber view to demonstrate the parallel imaging capabilities along the main axes of the two-dimensional coil array. Mean geometry factors for a ROI covering the heart together with the mean SNR and CNR values are surveyed in Table 9. The mean g-factor in the region of the heart remained below 2.0 for an acceleration factor of R = 4 for a four chamber view and for an acceleration factor of R = 5 for a two chamber and a long axis view of the heart. Noise amplification associated with one-dimensional parallel imaging increased severely at R=6.

	view	phase encoding direction	R = 2	R = 3	R = 4	R = 5	R = 6
mean SNR	4CV	A-P	18 ±10	15 ± 7	12 ± 6	9 ± 4	8 ± 3
		L-R	20 ±10	12 ± 3	11 ± 4	9 ± 3	8 ± 3
	2CV	H-F	17 ± 8	15 ± 8	14 ± 7	10 ± 5	7 ± 3
	SAX	H-F	23 ±12	20 ±10	17 ± 9	12 ± 6	11 ± 5
CNR	4CV	A-P	5	6	3	3	2
		L-R	6	4	3	2	3
	2CV	H-F	9	10	8	4	2
	SAX	H-F	19	12	10	7	4
mean g-factor	4CV	A-P	1.4	1.3	1.6	1.7	1.9
		L-R	1.3	1.9	1.7	2.0	2.2
	2CV	H-F	1.2	1.2	1.2	1.5	2.0
	SAX	H-F	1.3	1.4	1.4	1.8	2.1

Table 9: *SNR, CNR and g-factor results from the parallel imaging evaluation of the 32 channel transceiver array. GRAPPA accelerated imaging up to factor R=6 was evaluated for four chamber views (4CV), two-chamber views (2CV) and short axis views (SAX). The phase encoding direction of anterior-posterior (A-P), head-feet (H-F) and left right (L-R) were used. The statistics were evaluated inside a ROI encompassing the whole heart in the respective slice.*

4.6.5 Comparison with 3.0 T MR imaging

A signal gradient in the 7.0 T images from the areas close to the surface to deep lying regions can be observed. The following comparison with cardiac MRI performed at a clinical 3.0 T system (Verio, Siemens, Erlangen, Germany) adds numbers to quantify and compare this impression. The body coil incorporated in the clinical 3.0 T system was used for excitation.

For reception a commercially available local 32 channel array was used (In Vivo Corporation, Gainsville, Fl, USA). 2D FLASH CINE imaging was performed at 3 T and 7.0 T using the spatial resolutions of (1.8 x 1.8 x 6) mm³, (1.4 x 1.4 x 4) mm³ and (1.1 x 1.1 x 2.5) mm³. For 2D FLASH imaging at 3.0 T imaging parameters comparable to the 7.0 T pilot study were used (TE = 2.5 ms, TR = 5.5 ms, views per segment = 7, bandwidth = 401 Hz/ pixel, flip angle = 12°). GRAPPA acceleration with a reduction factor of R=2 was used.

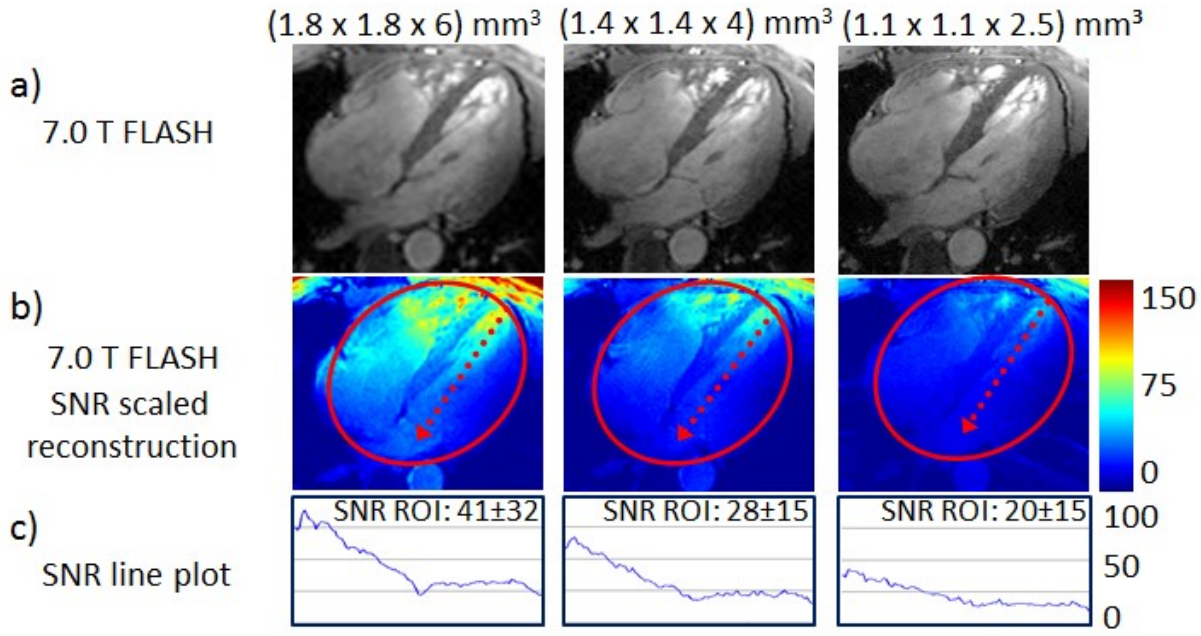

Figure 55: *2D FLASH CINE imaging conducted at 7.0T.* ***(a)*** *Images acquired with different spatial resolutions.* ***(b)*** *Corresponding SNR maps The ROI for statistics and the line for evaluation are depicted in RED.* ***(c)*** *Line plot of the SNR along the line depicted in b. A SNR gradient is observed from the vicinity of the coil to deep lying regions of the heart.*

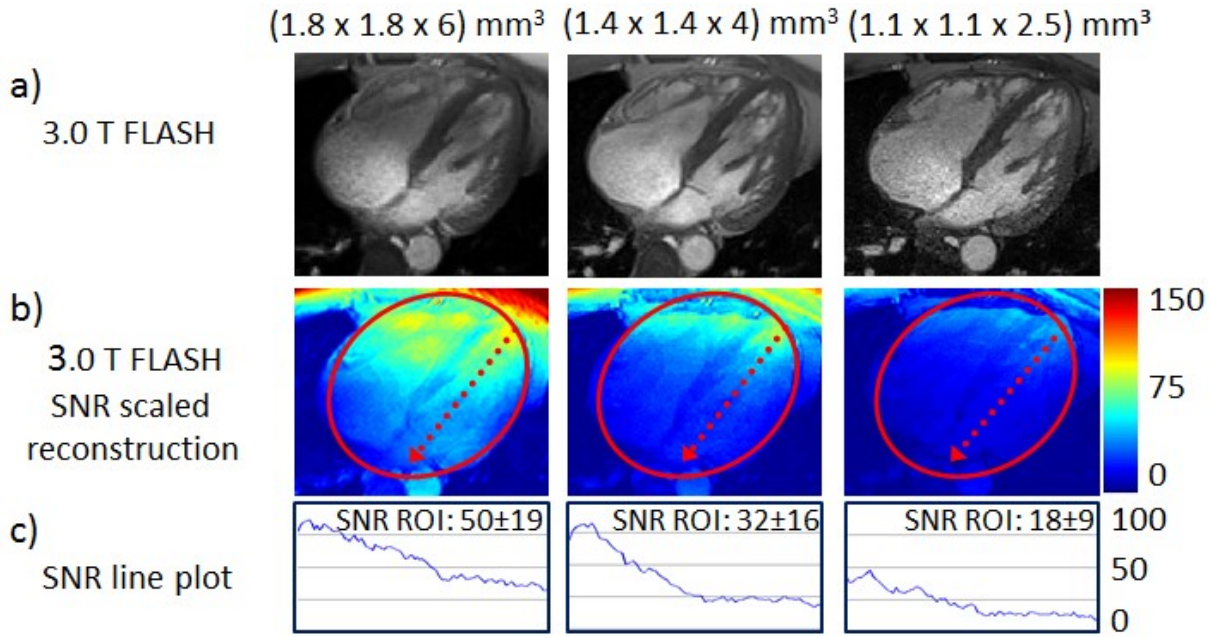

Figure 56: *2D FLASH CINE imaging conducted at 3.0T. For the purpose of comparison the same subject as at 7.0T , Figure 55 was used.* ***(a)*** *Images acquired with different spatial resolutions.* ***(b)*** *Corresponding SNR maps The ROI for statistics and the line for evaluation are depicted in RED.* ***(c)*** *Line plot of the SNR along the line depicted in b. A similarly strong SNR gradient as in the 7.0T acquisitions was observed. Additionally the noise in the high resolution image at 3.0 T becomes clearly visible in the image itself.*

Figure 55 and Figure 56compare the results derived from 2D CINE FLASH imaging at 7.0 T with lower magnetic field strengths. For this purpose 2D CINE FLASH imaging was conducted at 3.0 T using a four chamber view of the heart. The SNR gradient along a line drawn from the apex through the center of the mitral valve showed similar behavior at 7.0 T and 3.0 T.

4.7 Modular 32-channel transceiver array for abdominal imaging

The 32 channel setup presented for cardiac imaging is conceptually equally suited for imaging of other regions of the abdomen, i.e. the liver or the kidneys. Nevertheless the safety evaluation must be repeated for every chosen placement and incorporating the actual RF transmission setting in use. Transmission field shaping may be refined by focusing on the desired region of interest. In the following feasibility study the transmit setting of Table 8 was not altered. EMF and SAR simulations were repeated as described in chapter 4.6.1 with a lower abdominal position of the modules. A maximum value of 1.46 1/kg SAR normalized to 1 W input power was observed. The increased value compared to the simulation with module placement for cardiac imaging of 157% underlines the necessity for simulating altered RF

array placements at UHF. High resolution contrast agent free in-vivo imaging was conducted using a gradient echo sequence (TR/TE 21/3.08 ms, slice thickness 2.5 mm, matrix size 800 x 1024, bandwidth 380 Hz/pixel) with an in-plane resolution of (0,4 x 0.4) mm² for the coronal plane and (0.3 x 0.3) mm² for the transversal plane. The in-vivo images of Figure 57 exhibits a homogenious signal distribution throughout the lung, while offering a head-feet coverage of the abdomen of 35cm.

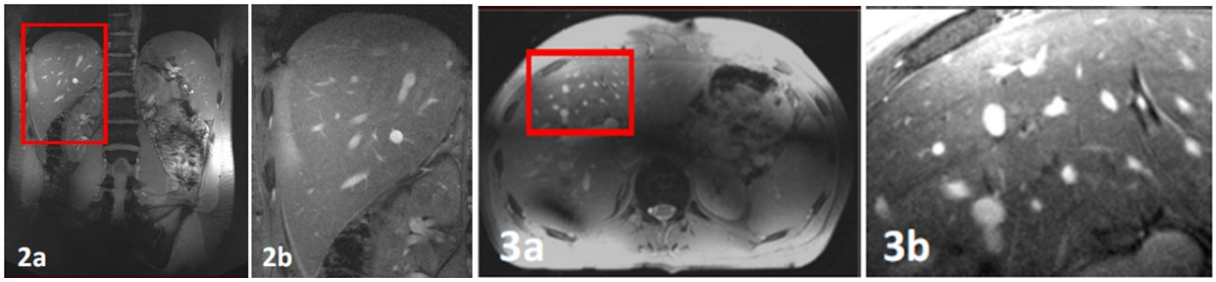

Figure 57: *Results of abdominal imaging using the 32 channel array and a T1 weighted 2D gradient echo sequence.* ***(a)*** *Coronal central abdominal slice with an enlarged depiction of the liver.* ***(b)*** *A Transversal slice throughout the liver. A high contrast between vessels and parenchyma is achieved without the use of contrast agent.*

4.8 Modular 16-channel transceiver array for spine imaging

Spine imaging is a very promising UHF MRI application to study the subtle anatomical structures of the vertebrae and the related nerves. The SNR benefits of UHF MRI can be turned into improved spatial resolution, while penetration depth issues are not prominent due to the near-surface position of the spine. To support spine imaging the four planar modules were aligned in a linear fashion to cover major parts of the human spine. Figure 58 shows the placement on a mannequin as well as the complete setup incorporated into one section of the patient table cushion.

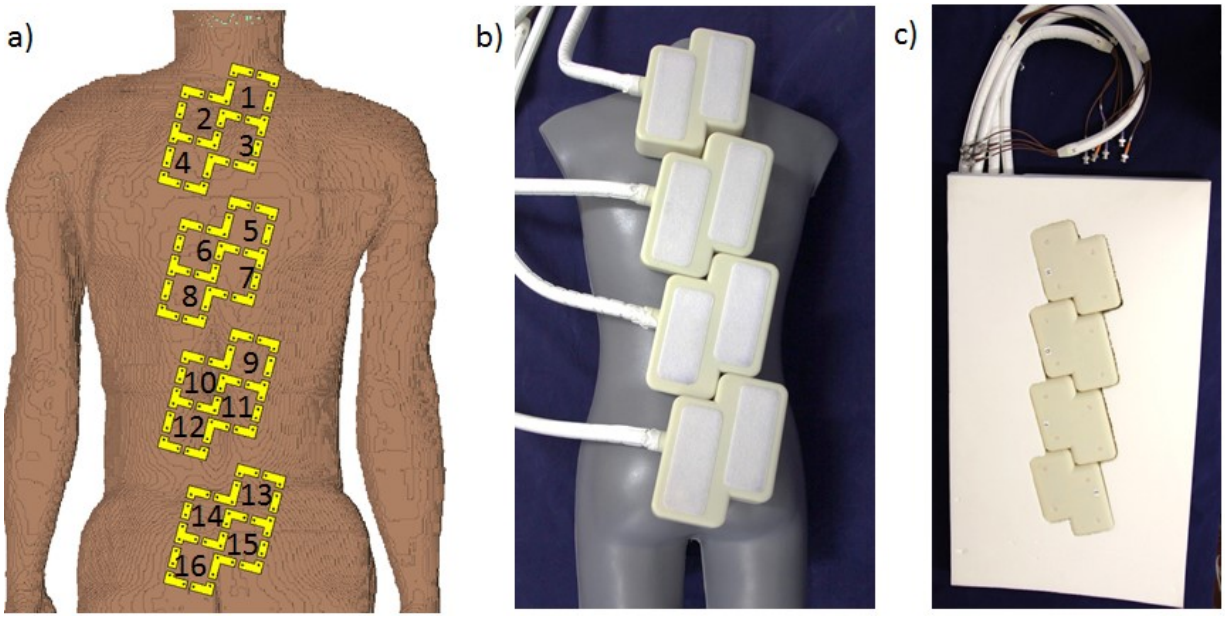

Figure 58: ***(a)*** *Loop structure and numbering for the 16 channel transceiver array compiled of four planar modules along the spine .****(b)****Picture of the modules on a mannequin.* ***(c)*** *Picture of the modules incorporated into one part of the patient table cushion.*

Based on the simulation model of the building block developed for the 32 channel cardiac array the SAR distribution inside the voxel model Duke was simulated for a transmission field setting used in the in-vivo study. The setting in Table 10 was chosen based on the reported results of an eight channel spine array [137], which showed good transmit field distribution for a 180 degree phase shift between elements placed along the left and the right side of the spine.

Channel	1	2	3	4	5	6	7	8
phase °	0	180	0	180	0	180	0	180
Channel	9	10	11	12	13	14	15	16
phase °	0	180	0	180	0	180	0	180

Table 10: *Transmission phases used in the in-vivo study for homogeneous excitation with the sixteen channel spine setup. The phase setting was chosen based on the reported results of an eight channel spine array* [137].

The EMF and SAR simulation yielded a maximum value of 1.471/kg local SAR_{10g}. Considering the hardware losses along the signal transmit path of 3.18 dB this value translated into a maximum allowed input power of 7.0 W_{RMS} to stay within the legal guidelines [81]. RF characterization based on S-parameter measurements was performed to assess the effect of the altered placement of the modules along the spine without retuning of

the modules of the 32-channel cardiac array. The maximum projection of four independent measurements on human subjects indicate a rather stable performance of the impedance match as well as the decoupling, as depicted in Figure 59 b. The worst case reflection coefficient was found to be -9 dB, the worst case decoupling was found to be -12 dB.

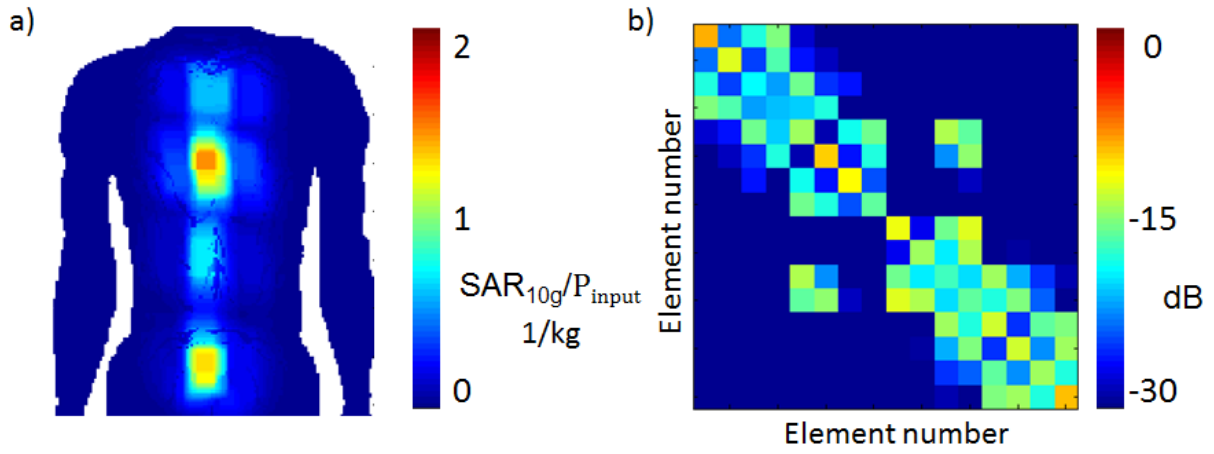

Figure 59: ***(a)*** *SAR results of the EMF simulation based on the voxel model duke. The maximum projection plot of the local 10 g averaged SAR distribution exhibits a maximum of 1.471/kg.* ***(b)*** *Maximum projection of the S-parameters measured for four subjects at 297 MHz.*

Having proven the SAR and RF parameters of the new arrangement of the modules meeting the given legal and technological boundary conditions, in-vivo imaging in healthy subjects was performed performance using T1 and T2 weighted sequences. Figure 60 a, b demonstrate the extended FOV provided by the proposed array, allowing to image major parts of the spine without altering the coil position. Figure 60 c shows an exemplary image acquired with a Turbo Spin Echo (TSE) sequence, which offers high contrast in the spinal canal. Finally a high resolution image of the vertebra is shown in Figure 60 d with a voxel size of (0.13x0.13x1) mm^3. These results are meant to serve as a precursor for a broader clinical study to assess the benefits for clinical assessment and treatment decision by depicting subtle anatomical structures of the facet joint as well as the encompassing nerves in the presented image quality.

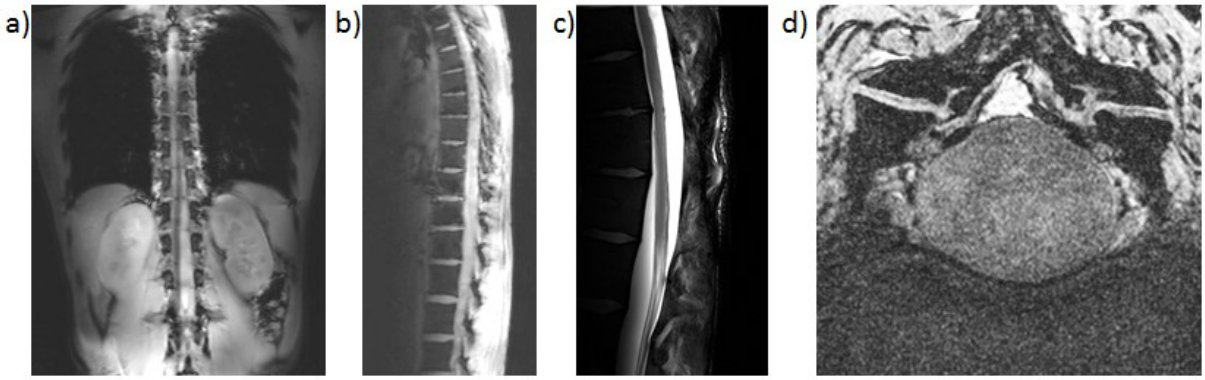

Figure 60: *GRE imaging (TE/TR 3.36/7.5 ms) used for localization and demonstrating the coverage of the proposed array in a coronal* ***(a)*** *and sagittal* ***(b)*** *view.* ***(c)*** *Sagittal TSE image of the thoracic spine (voxel size (0.27x0.27x3)mm³, averages 3, TE/TR 91/4860 ms, TA 7:46min).* ***(d)*** *3D GRE image depicting the transverse processes, the capsule of the facet joint (black arrow) and the medial ramus of the posterior division of the spinal nerve (white arrow) (voxel size (0.13x0.13x1) mm³, NA=2, TE/TR 4/3312 ms, TA 2:44min).*

4.9 Modular 12-channel transceiver array for shoulder imaging

Investigating the applicability of the four-channel modules for musculoskeletal MRI at UHF the shoulder joint is another promising target region. The complex anatomy of the shoulder joint can benefit from the increased resolution, while its opaque position makes it rather immune against RF inhomogenieties and issues connected with the reduced penetration depth at higher frequencies. Figure 61 introduces the compilation of a 12-channel shoulder array for 7.0 T consisting of three modules together with the channel numbering and the intended placement on a mannequin. The RF characteristics as well as the SAR performance were investigated for the intended placement before an initial in-vivo subject study.

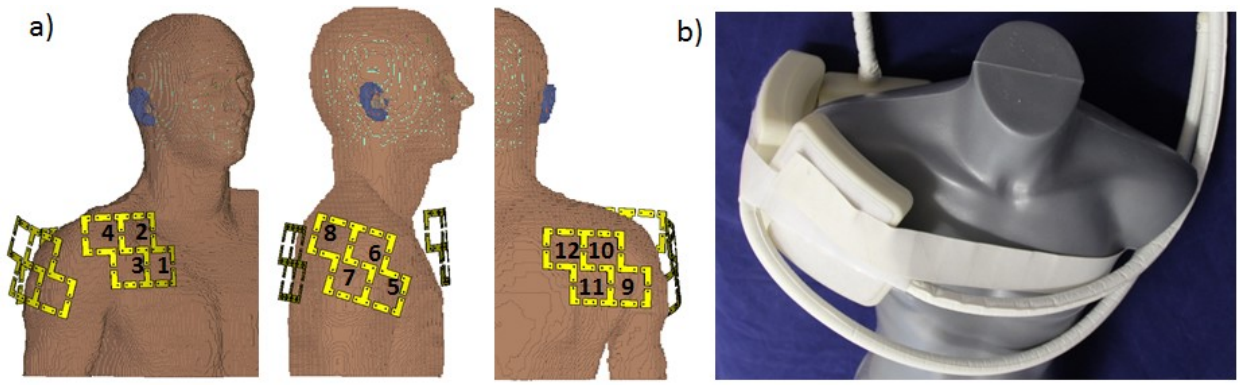

Figure 61: ***(a)*** *Loop structure and numbering for the 12 channel transceiver array compiled of two curved and one planar element in a U-shape around the shoulder.* ***(b)*** *Picture of the modules on a mannequin. The modules are hold in place by flexible hook and loop fastener.*

Conducting EMF simulations using the principle setup and workflow as presented for the 32-channel cardiac array, the modules were evaluated on the voxel model Duke, exemplarily on the right shoulder as used in the pilot in-vivo study. For transmission the modules were driven by a phase corresponding to their angular position to the shoulder joint in the transversal plane, while the phases of the elements inside of one module were the same, as documented in Table 11. Application of the array to the left shoulder can be done analogously, but asks for an adapted transmission phase setting to uphold the geometrical CP mode for the mirrored module placement. The SAR simulation for the setup used in the in-vivo study revealed a maximum local SAR_{10g} of 1.52 1/kg, located at the surface, as depicted in Figure 62a. Together with measured hardware losses in the RF power signal chain of -3.18 dB and the limit of 10W/kg given by the legal guideline [81] the maximum permitted signal power was set to 7.5 W_{RMS}. The RF bench measurements of the array conducted on four healthy subjects revealed an acceptable RF performance without retuning the elements of the 32channel cardiac array. A worst case reflection coefficient of -9.5 dB and a worst case decoupling of -9.3 dB were observed, see Figure 62b.

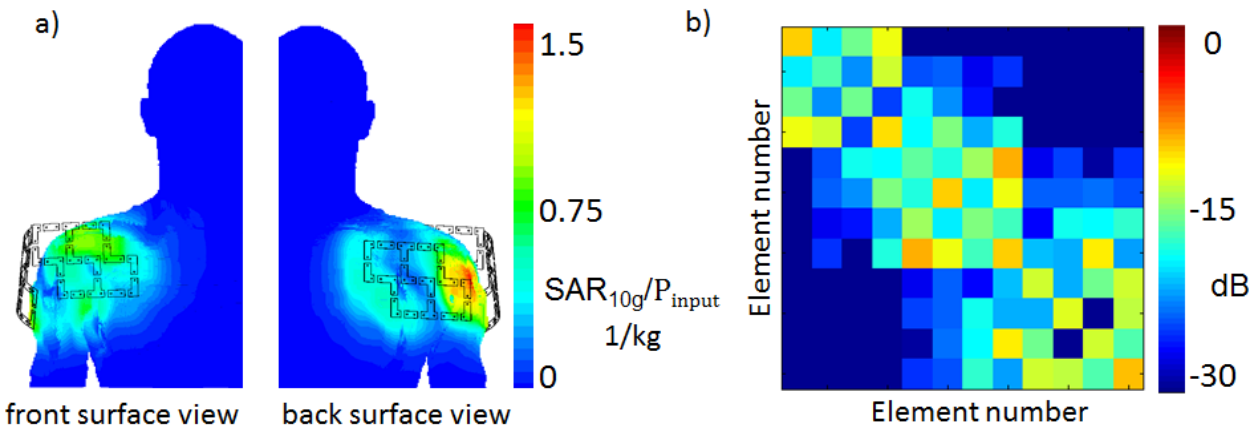

Figure 62: ***(a)*** *SAR results derived from EM simulations of the 12-channel TX/RX shoulder array. Surface plots for the front and back are shown for the local 10 g averaged SAR distribution for the male human voxel model Duke. A maximum value of 1.52 1/kg was found, which determined the applicable transmit power.* ***(b)*** *Maximum projection of the S-parameters measured on four subjects at 297 MHz.*

Channel	1	2	3	4	5	6	7	8
phase °	-180	-180	-180	-180	-270	-270	-270	-270
Channel	9	10	11	12				
phase °	0	0	0	0				

Table 11: *Transmission phases used in the in-vivo study for homogeneous excitation with the 12 channel shoulder setup. Due to the limited size of the shoulder the phase setting was chosen to reassemble a module-wise circular polarized transmission scheme.*

In-vivo imaging was conducted on healthy subjects within clinical acceptable scan times. Figure 63a shows a transversal image of the shoulder joint acquired with four-fold GRAPPPA accelerated parallel imaging. Within a scan time of 1:47 min a spatial resolution of (0.3x0.3x1.5)mm³ was achieved without notable noise amplification. B_1^+ mapping revealed a homogeneous transmission field distribution across the shoulder joint with increased values at the surface areas in the vicinity of the coil elements. The mean value inside the ROI of the zoomed view in Figure 63a was found to be 7 $\frac{\mu T}{\sqrt{kW}}$. This initial result together with the results of the spine application add further evidence that the modular approach is a volatile way of providing RF array technology for multiple musculoskeletal applications. The necessary changes restrict to the adjustment of the placement, the transmit setting and the power limits based on simulations. With that, major technological hurdles in the setup of clinical studies at 7.0 T are removed and valuable time and resources for entirely new coil designs can be saved.

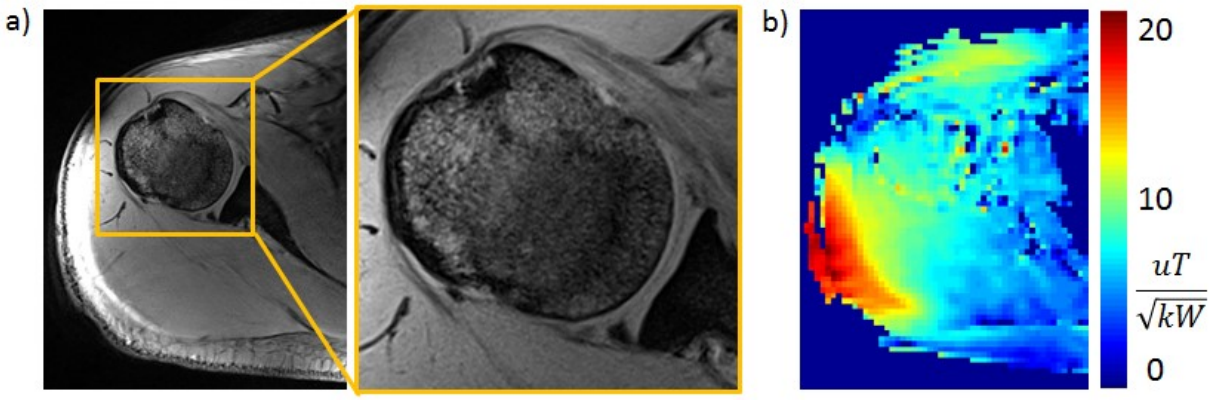

Figure 63: ***(a)*** *Transversal slice through the shoulder joint acquired with a T1 weighted vibe sequence using parallel imaging with a GRAPPA reduction factor of 4((0.3x0.3x1.5)mm³, TE/TR: 4.04/11.5 ms, TA 1:47min, matrix size 640x 640).* ***(b)*** *Absolute* $\boldsymbol{B_1^+}$ *map of the transversal slice depicted in a). The strong transmission field strength at the surface is inevitable for local transmit arrays. Nevertheless the transmission field map exhibits a sufficient penetration depth together with a homogeneous excitation throughout the shoulder joint.*

4.10 Ophthalmic imaging using a six-channel transceiver array

In vivo imaging of the spatial arrangement of eye segments and their masses is an emerging MRI application and ultimately aims at performing MR image-based biometry. Eye MRI

requires high spatial resolution over a small field of view (FOV). Again, the intrinsic SNR gain of 7.0 T that can be translated into an increased spatial resolution is the driving force to tackle the technological challenges at UHF. For this purpose, a six-element transceiver eye coil array (f=298 MHz) which uses loop elements is developed and applied in a healthy subject study as well as in a patient study. Our EMF simulations and experimental results indicate that the use of multiple surface coil transceiver loop elements yields an excellent SNR for eye imaging, affords uniform signal intensity across the eyes, and facilitates the depiction of anatomical details of the eye.

Parts of the work related to the orbita array outlined in this chapter were published in a peer reviewed journal [138]. Major parts of the EMF simulations were conducted during the bachelor thesis of Max Muhle [139], the construction of the array was conducted during the bachelor thesis of Michael Schwerter [140]. Further clinical studies were based on the orbita array [117,141].

4.10.1 Design considerations

A symmetric design is used to cover each eye with three planar transceiver loop elements (Figure 64 a). The three loop elements are angled (element 1 vs. element 2: 151° and element 2 vs. element 3: 161°) to conform to the anterior head as shown in Figure 64 b. The width of the rectangular elements was set to 36 mm (elements 1 and 2) and 45 mm (element 3). An element height of 71 mm and a conductor width of 10 mm was used (Figure 64 a). Adjacent elements share a common conductor with a trimmer capacitor (Voltronics, MD, USA) for decoupling (Figure 64 b). Next neighbor decoupling was achieved using coaxial cables for connection and two trimmer capacitors for decoupling. All other elements were decoupled by distance.

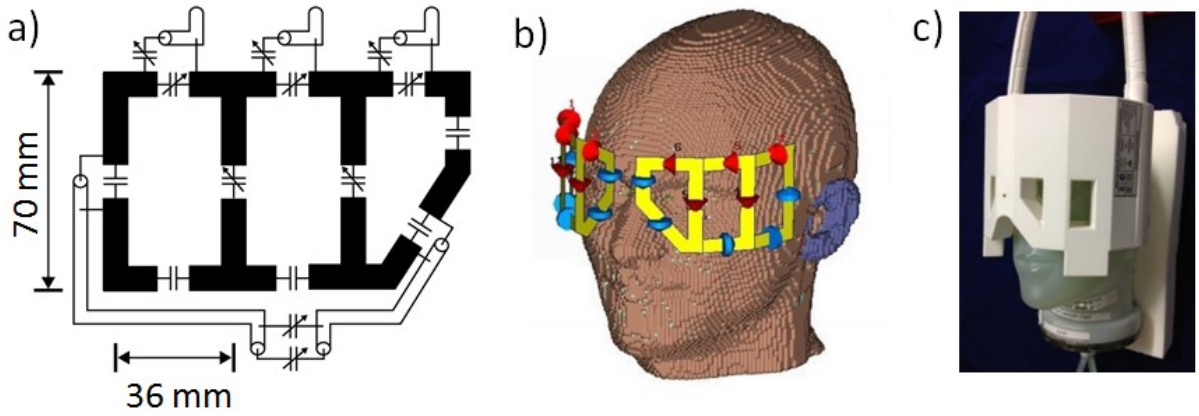

Figure 64: ***a)*** *Technical drawing of one half of the orbita array* [140]. ***b)*** *Simulation model of the complete array shown on the forehead of the human voxel mdel Duke* [139]. ***c)*** *Final hardware placed on a head-shaped phantom.*

Figure 64 c depicts the final orbita RF transceiver array. The RF coil is light weight with a weight of m = 804 g and conforms to a broad range of head geometries.

4.10.2 EMF simulation and RF characterization

EMF and specific absorption rate (SAR) simulations were performed using CST Studio Suite 2011 (CST AG, Darmstadt, Germany) in conjunction with the voxel models Ella and Duke from the Virtual Family [2].

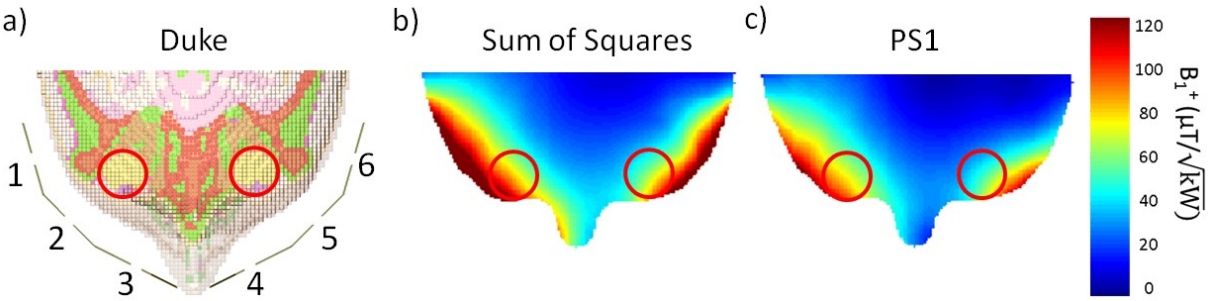

Figure 65: *RF Shimming result based on simulated individual field contributions of the six transceiver channels.* ***(a)*** *Schematic view of the element position with respect to the eyes of the human voxel model Duke.* ***(b)*** *The sum of square combination of the individual fields displaying a pixel-wise constructive interference as the upper bound for any RF shimming.* ***(c)*** *Resulting* $\boldsymbol{B_1^+}$ *field of the optimized phase setting (PS1).*

The optimized phase setting that was found by the optimization is summarized in Table 12. The resulting transmit field can be seen in Figure 65 c. Hardware-wise the phase adjustment of each channel was accomplished by phase-shifting coaxial cables added to the power splitting network. SAR values derived from the EMF simulations using calculated phase

settings optimized for B_1^+ uniformity were well below the limits permitted by the IEC guidelines [81] for an average input power of 1 W over 6 minutes as illustrated in Figure 66 a, b.

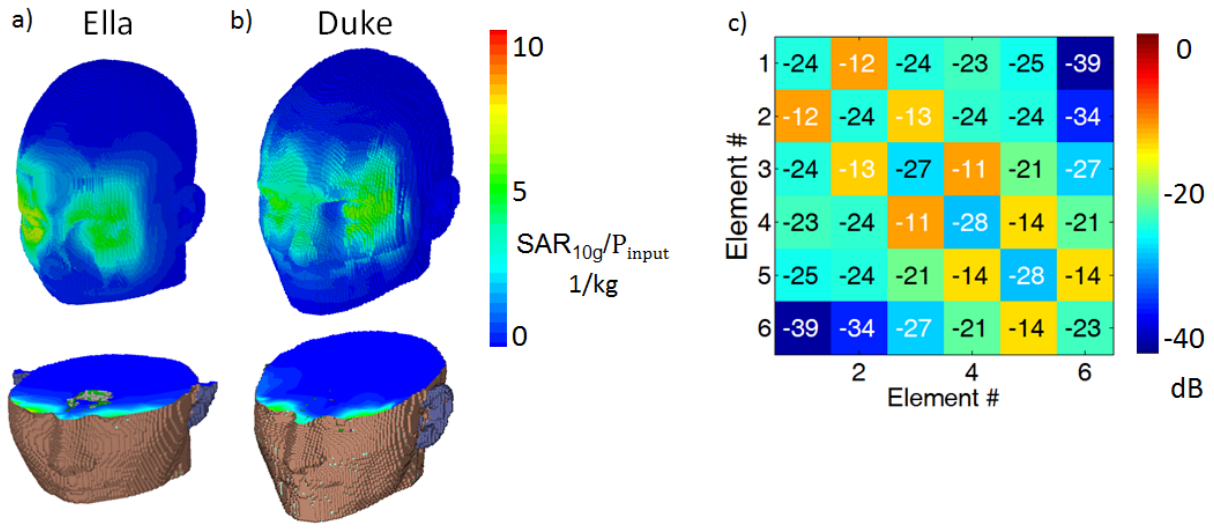

Figure 66: *SAR simulation results for the female voxel model Ella* ***(a)*** *and the male voxel model Duke* ***(b)*** *using the phase setting of Table 12. The comparable quantitative and qualitative results of the two independent simulations underline the validity of the derived power restrictions.****(c)*** *S-parameter matrix measured on a healthy human subject.*

Channel	1	2	3	4	5	6
phase °	0	-327	-250	0	-327	-250

Table 12: *Transmission phases used in the in-vivo study for homogeneous excitation with the six channel orbita array.*

The loop elements showed an average QU/QL of 4.6. Reflection coefficients of the individual elements averaged over five volunteers were in a range of -22 dB to -28 dB. Element coupling was below -10 dB for all elements and subjects. Noise correlation was below 0.4 for all elements and subjects.

Based on a thorough safety assessment in line with IEC 60601-2-33:2010 Ed.3 and IEC 60601-1:2005 Ed.3 [81], the technical documentation and a risk management file the RF array was approved for implementation in clinical studies following certification by a notified body.

4.10.3 In-vivo MR imaging study

Eye imaging at 7.0 T was performed on healthy subjects (n=17, 24-64 years, BMI 24.5±2) using T1- and T2-weighted techniques. Subject preparation to reduce eye motion artifacts was performed [121]. The investigated eye was kept closed to omit susceptibility artifacts, while the fixation with the open eye lead to a steady state of both eyes. Furthermore each protocols was subdivided into several data acquisition periods by the use of an external trigger [121,142]. The audio-visual triggering scheme indicated the acquisition time by a bell tone followed by a red screen presented to the subject at the end of the bore including a cross to fixate the gaze of the open eye for 3 s. A green screen allowed for a closing or blinking period of another 3 s. Subsequently, the bell again asked for re-fixation. The alternating gaze fixation-resting periods were repeated until the end of each scan series. Absolute transmission field mapping using the Bloch-Siegert method was used for flip angle calibration so that the actual flip angle represents the nominal flip angle in the center of the eye. The imaging protocol included four different imaging protocols. For 3D gradient echo imaging (3D GRE) with a spatial resolution of (0.3 x 0.3 x 1.0) mm3 the parameters were: TR=10.3 ms, TE=3.6 ms, nominal flip angle 6°, FOV=(81 x 58) mm², matrix size=320 x 230, 24 slices per slab, receiver bandwidth of 300 Hz/pixel, number of averages=2. The nominal acquisition time was 3:12 min. For 3D gradient echo imaging (3D GRE) with a spatial resolution of (0.2 x 0.2 x 1.0) mm3 the parameters were: TR = 12 ms, TE = 5.9 ms, nominal flip angle 8°, FOV = (50 x 50) mm², matrix size = 256 x 256, 32 slices per slab, receiver bandwidth of 230 Hz/pixel. The acquisition time was 2:09 min including resting periods for eye blinking. For inversion recovery 3D gradient echo (3D IR-GRE) imaging with a spatial resolution of (0.4 x 0.4 x 1.0) mm3 the parameters were: TR = 13.6 ms, TE = 6.5 ms, inversion time TI= 1900 ms, nominal flip angle 6°, FOV = (103 x 74) mm², matrix size = 256 x 184, 24 slices per slab, receiver bandwidth=300 Hz/pixel, 2 averages, and linear, regular density Cartesian phase encoding. The nominal acquisition time was 1:43 min. For 2D T2 weighted fast spin-echo (2D FSE) imaging using a spatial resolution of (0.25 x 0.25 x 0.7) mm3 the parameters were: TR=2940 ms, TE=85 ms, nominal flip angle of the refocussing pulses= 100°, FOV = (84 x 60) mm², matrix size = 384 x 245, 6 slices, receiver bandwidth of 260 Hz/pixel, 4 averages, and two-fold acceleration along the A-P phase encoding direction using GRAPPA reconstruction. The acquisition time was approximately 2:00 min per average including resting periods for eye blinking.

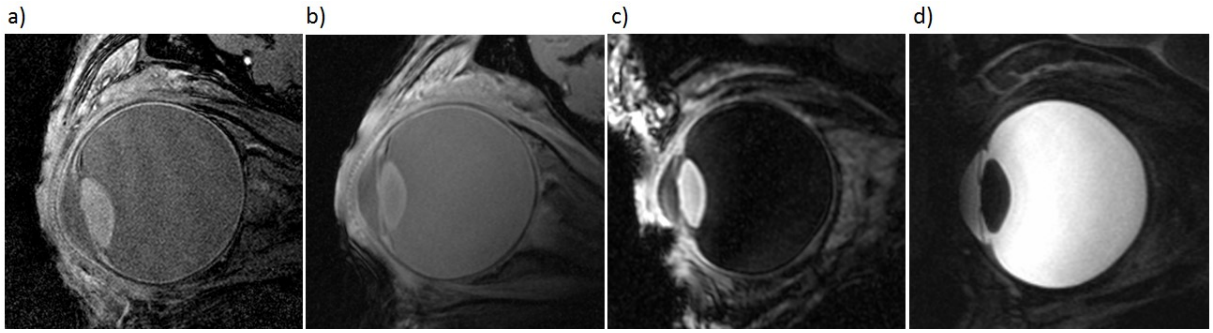

Figure 67: *Results of ophthalmic MRI in healthy subjects using the six-channel transceiver array.* ***(a)*** *Transversal view of the eye derived from 3D GRE imaging using a spatial resolution of 0.2x 0.2x1.0 mm3 and* ***(b)*** *0.3x0.3x 1.0 mm3.* ***(c)*** *Sagittal views of the eye derived from 3D IR-GRE imaging using a spatial resolution of 0.4x 0.4x 1.0 mm3.* ***(d)*** *Sagittal views of the eye derived from T2-weighted 2D FSE imaging with a spatial resolution of 0.25x 0.25x 0.7 mm3.*

In vivo imaging demonstrated rather uniform signal intensity for sagittal and transverse views of the eye as shown in Figure 67. For parallel imaging, mean geometry factors based on SNR scaled imaging [72] of g=1.1 (R=2), g=1.9 (R=3) and g=3.4 (R=4) were observed for a ROI covering the eyes and segments of the optical nerve.

4.10.4 In-vivo MR imaging of tumor patients

M vitreous humor R imaging was performed in patients with intraocular masses (uveal melanoma, n=5, 50-68 years, BMI 26±5) using the protocols adjusted during the healthy subject study. Figure 68 depicts the MR imaging results of two patients with malignant melanoma of choroidea with retinal detachment. All images exhibit a homogeneous signal throughout the homogeneous vitreous humor and the tumor tissue is clearly delineated.

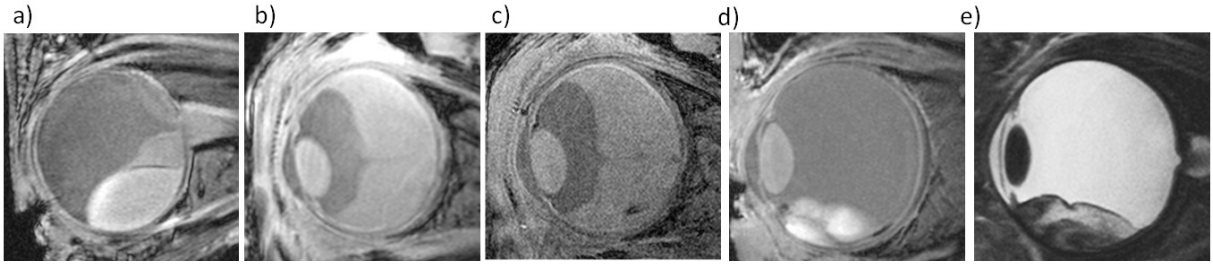

Figure 68: (*a,b)* *Sagittal and transversal invivo images of the right eye obtained from 3D GRE imaging (spatial resolution, 0.3x0.3x1.0 mm3) of a patient with malignant melanoma of choroidea with retinal detachment.* ***(c)*** *Further improved spatial resolution of 0.2x0.2x1.0mm3 for the view shown in (b).* ***(d)*** *Sagittal views of the left eye obtained from 3D GRE imaging (spatial resolution, 0.3x0.3x1.0 mm3).* ***(e)*** *Sagittal views of the left eye obtained from 2DT2-weighted FSE imaging (spatial resolution, 0.25x0.25x0.7 mm3) of another patient with malignant melanoma of choroidea with retinal detachment.*

4.10.5 Comparison with a commercial head coil

For comparison with a commercially available head coil T2-weighted 2D FSE imaging was performed using a head coil equipped with one transmit and 24 receive channels (Nova Medical Inc., Wilmington MA, US). For this purpose the imaging parameters were adjusted to avoid folding artifacts (TR=2940 ms, TE=85 ms, spatial resolution=(0.53 x 0.53 x 0.7) mm3, FOV=(204 x 130) mm², matrix size=384 x 245, receiver bandwidth=260 Hz/pixel, 4 averages), while keeping the acquisition time constant at 2:00 min per average as for the orbita array. Two-fold acceleration along the A-P phase encoding direction using GRAPPA reconstruction was applied. Figure 69 displays the results. For the 6 channel TX/RX coil rather uniform signal intensity was observed across the eye, while the head coil configuration yielded a substantial change in signal intensity across the eye. For a profile (marked by the blue dotted line) perpendicular to the line connecting the lens with the retina (marked by the red dotted line) a mean signal intensity change of <5 % was determined for the 6 channel TX/RX array. In comparison, the head coil configuration showed a 90 % signal intensity decrease for the same profile.

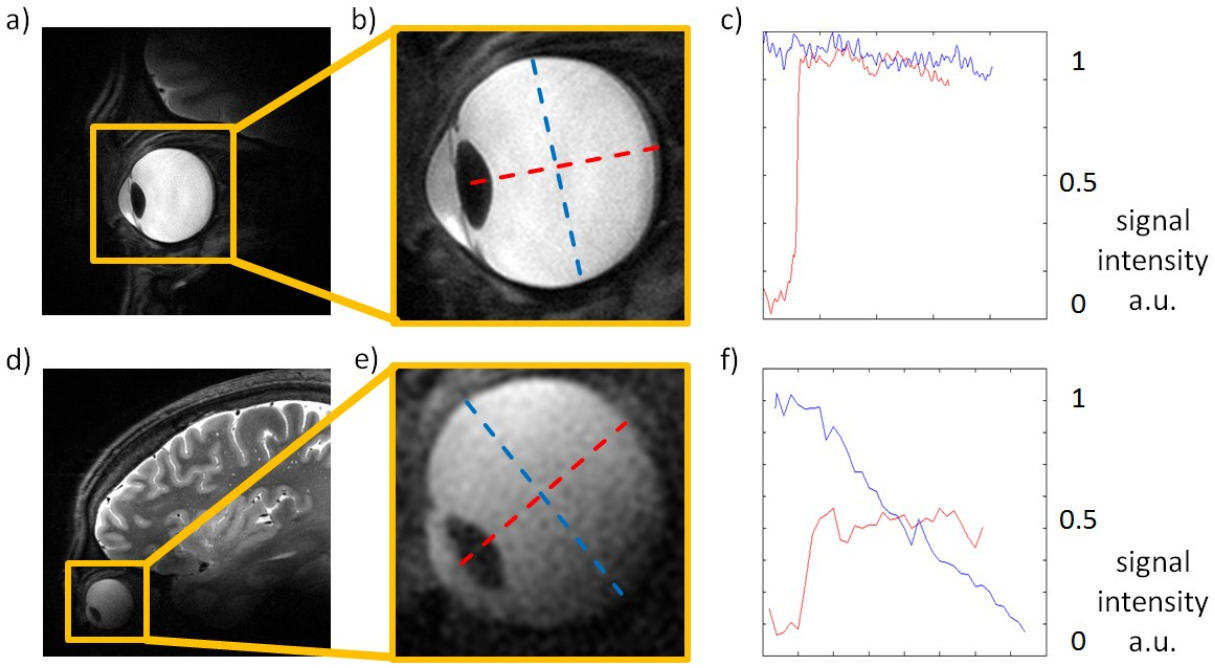

Figure 69: *Comparison of results derived from T2-weighted 2D fast spin-echo imaging of healthy subjects using the 6 channel TX/RX local array* ***(a,b,c)*** *versus the TX1RX24 head coil* ***(d,e,f)****. The uncropped images a) and d) show the different FOVs necessary to avoid folding artifacts in the eye. The zoomed views b) and e) show the image result of the eye for a similar image size. The red and blue line plots c) and f) exhibit the signal intensity along the corresponding red and blue dotted lines from left to right in the zoom images.*

4.11 Cardiac imaging with a sodium multi-channel transceiver array

The intrinsic SNR gain of UHR MRI is particular interesting to explore the capabilities of x-nuclei imaging, which historically suffer from insufficient SNR levels at clinical magnetic field strength. To investigate ^{23}Na cardiac imaging at 7.0 T tailored radiofrequency technology for transmission and reception at the corresponding frequency of 76 MHz is crucial. Realizing this necessity this work proposes a four-channel transmit and receive RF coil array for ^{23}Na cardiac imaging at 7.0 T. Electro-magnetic field simulations were conducted for RF safety evaluation. Volunteer studies, as a precursor to a broader clinical study are performed and demonstrate the feasibility of clinically relevant ^{23}Na imaging of the heart.

Parts of the work outlined in this chapter were published in a peer reviewed journal [162].

4.11.1 Development of a transceiver array for sodium cardiac MRI

The setup consists of separate elements for ^{23}Na and ^{1}H imaging. This assures a minimum of additional hardware in the RF elements intended for sodium imaging. A four channel ^{23}Na RF

coil array was constructed in two modestly curved lightweight housings to conform to an average chest and back as illustrated on a mannequin in Figure 70 a. Each section contains two 210 x 140 mm² rectangular loop elements sharing a common conductor as shown in Figure 70 b, c. The structure shown in Figure 70 b was etched from 32 µm copper on 1mm FR4 substrate. The loop is divided into five parts by chip capacitors to form a homogeneous current distribution along the loop. A trimmer capacitor (C4) is part of the shared conductor to allow for adjustable decoupling of the neighbouring loops [51]. The common conductor of the anterior part also includes a parallel resonant trap circuit (C6/L6) tuned to 297 MHz to prevent ^{1}H signals to couple into the loop structure. The ports are connected to the coaxial cables with a tune/match network consisting of a parallel tuning capacitor and a serial matching trimmer capacitor for each loop element. The coil was tuned to 78.6 MHz which corresponds to the resonance frequency of ^{23}Na at 7.0 T and matched to 50 Ω. Unbalanced currents on the coaxial cables were suppressed by parallel resonant cable traps. Cable traps were designed as double-turn solenoids of the coaxial cable with an appropriate capacitor soldered to the outer conductor at the crossing of the cable.

^{1}H imaging capabilities are added by a dipole element tuned to 297 MHz as introduced in [131] and used for the sixteen-channel cardiac array in chapter 4.4. It is placed inside the left loop element of the anterior section as depicted in Figure 70 b. This adds means for basic localization, B0 shimming and slice positioning based on ^{1}H images.

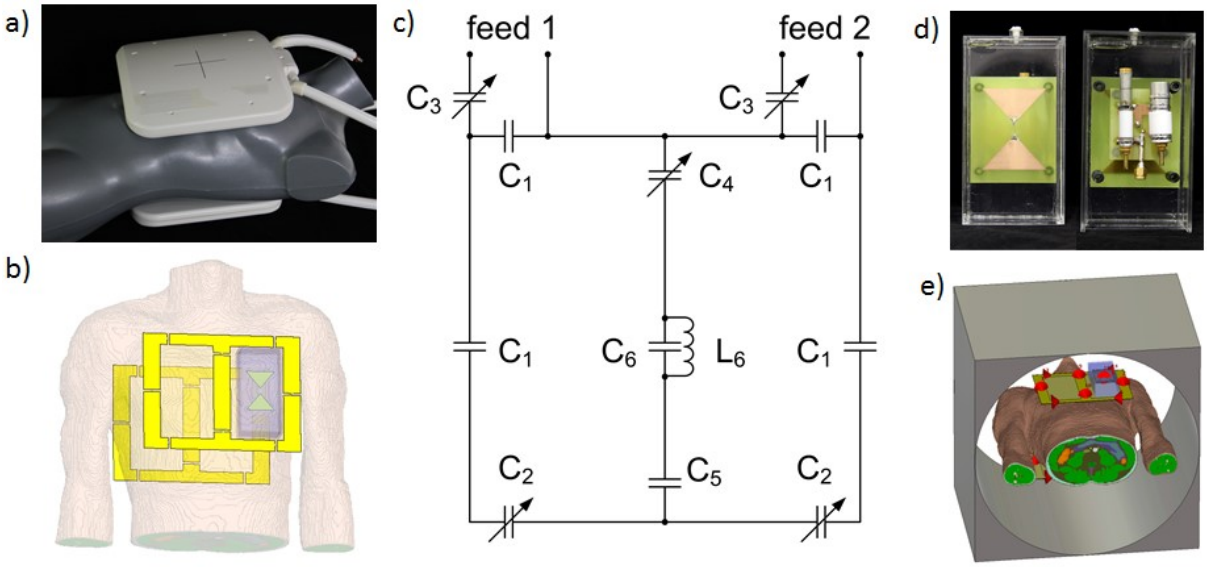

Figure 70: ***(a)*** *The anterior and posterior part of the sodium array on a mannequin.* ***(b)*** *Basic loop structure of the sodium array shown in the simulation model.* ***(c)*** *Circuit diagram of the anterior part of the sodium loop array.* ***(d)*** *Picture photograph of the dipole element for proton imaging, placed inside loop element two as illustrated in b).* ***(e)*** *Simulation setup consisting of the sodium array, the dipole element and the voxel model duke inside the bore given by the gradient shield.*

The x-nuclei amplifier output was split into 4 equal-amplitude signals by means of three hybrid couplers (Anaren Microwave Inc., New York, US) compiled to a splitting cascade from 1:2 and 2:4. Phase adjustments of the single channels were implemented by phase-shifting coaxial cables connected to the power splitting network. The four ^{23}Na elements and the one ^{1}H element were connected to the RF system using an interface box with transmit/receive switches and integrated low-noise preamplifiers designed for the corresponding frequencies (Stark Contrast, Erlangen, Germany).

4.11.2 EM simulation and RF characterization

At 78.6 MHz, in the frequency range of 1.5T proton imaging, transmission field homogeneity and RF shimming present no major hurdles in UHF sodium imaging. Therefore a circular polarized (CP) like mode is used for transmission. The CP mode refers to a phase setting with each channel driven by a phase corresponding to its angular position relative to the body centre in the transversal plane. All simulation results as well as the in-vivo study are based on the phase setting in Table 13.

Channel	1	2	3	4
phase °	0	-305	-136	-93

Table 13: *Transmission phases used in the in-vivo study for homogeneous excitation with the four-channel sodium array.*

EMF and SAR simulations were performed using the finite integration technique of CST Studio Suite 2012 (CST AG, Darmstadt, Germany) together with human voxel models Duke. The simulations included the RF shield of the gradient coils. The voxel model was truncated at the neck and at the hips as displayed in Figure 70b, allowing for a high resolution mesh in the target region. Two simulations were performed with voxel model tissue parameters corresponding to 78.6 MHz and 297 MHz as listed in [40] to estimate SAR values for the respective frequencies. The input power for both frequencies was adjusted to meet the regulations of the IEC guideline IEC 60601-2-33 Ed.3 [81].

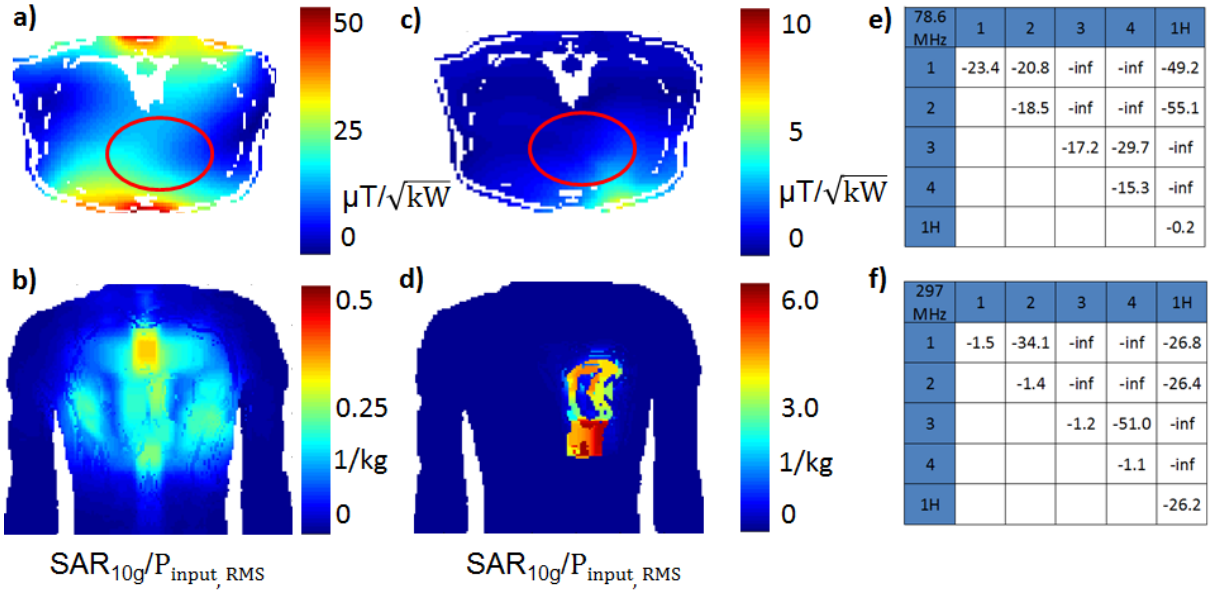

e)

78.6 MHz	1	2	3	4	1H
1	-23.4	-20.8	-inf	-inf	-49.2
2		-18.5	-inf	-inf	-55.1
3			-17.2	-29.7	-inf
4				-15.3	-inf
1H					-0.2

f)

297 MHz	1	2	3	4	1H
1	-1.5	-34.1	-inf	-inf	-26.8
2		-1.4	-inf	-inf	-26.4
3			-1.2	-51.0	-inf
4				-1.1	-inf
1H					-26.2

Figure 71: ***(a)*** *Transmission field simulation for the four channel ^{23}Na array depicted in a transversal plane through the heart (ROI in red) using the circular polarized phase setting.* ***(b)*** *Maximum projection plot of the local SAR_{10g} distribution for the human voxel model Duke based on the circular polarized phase setting.* ***(c)*** *Transmission field simulation at 297 MHZ for the ^{1}H dipole element depicted in a transversal plane through the heart (ROI in red).* ***(d)*** *Maximum projection plots of the local SAR_{10g} distribution for the male human voxel model induced by the dipole element.* ***(e)*** *Scattering parameters measured on a subject to demonstrate the resonance behavior of the ^{23}Na/^{1}H setup at 78.6 MHZ.* ***(f)*** *Scattering parameters measured on a subject at 297 MHZ.*

Figure 71a shows the combined transmit field for the ^{23}Na array driven with the CP like phase setting for a transversal slice through the voxel model's heart. $SAR_{10\,g}$ values derived from the EM simulations are outlined in Figure 71b. For the CP like mode the maximum local $SAR_{10\,g}$ value was found to be 0.39 1/kg per input power. For the ^{1}H dipole element the transmit field is shown in Figure 71c. The respective local $SAR_{10\,g}$ distribution in Figure 71d exhibits a maximum value of 1.46 1/kg per input power. With an input power of 25 W for the ^{23}Na array and 6.8 W input power for the ^{1}H dipole, considering the measured power losses in the RF chain, $SAR_{10\,g}$ values were below the limits permitted by the IEC guidelines [81]. The first and second level controlled mode given by the IEC guidelines were not used in the in-vivo applications which limits the maximum local $SAR_{10\,g}$ to 10 W/kg and thus preserves a safety margin of factor 2.

The ^{23}Na loop elements were found to have an average Q_U/ Q_L of 8.4. Reflection coefficients of -15 dB or less were observed. Element coupling was below -20 dB for the neighboring elements. Anterior posterior coupling was below noise level. The reflection coefficient of the ^{1}H dipole was -26 dB. The decoupling of the ^{23}Na loop elements to the ^{1}H dipole was below -49 dB at 78.6 MHz and below -26 dB at 297 MHz for all ^{23}Na loops. The complete set of s-parameters for both frequencies is surveyed in Figure 71e, f. Overall losses from the system RF output to the individual coil connectors were determined to be -0.7 dB for the ^{23}Na path and -1.4 dB for the ^{1}H path, which were considered for the input power calculation.

4.11.3 In-vivo study

In-vivo cardiac MR was performed in three healthy subjects (2 male, 1 female; age range: 26 - 29; BMI range: 19 - 22, heart rate range: 62 - 78 bpm). Flip angle calibration was done offline in Matlab, using a curve fitting algorithm on a set of signal intensity points, acquired with a set of reference amplitudes. For flip angle calibration the whole field of view was taken into account. CMR images were acquired using two imaging protocols for ^{23}Na MRI. A 3D gradient echo sequence adjusted to a short TE as well as a density-adapted 3D radial acquisition technique described in [143, 161]. The In vivo study yielded a recognizable ^{23}Na contrast in all regions of the human heart. The reference amplitude was found to be 680 Volts in an exemplary subject, leading to a 180° pulse assuming a rectangular pulse applied for 1 ms. An intense signal caused by the high ^{23}Na concentration of the ribs was observed in all acquisitions. For the gradient echo acquisitions the SNR maps were estimated using the methods 4 proposed in the NEMA standard MS-1 [144]. According to [144] the noise value in

magnitude images is given by the standard deviation of the signal in a noise-only region divided by the factor 0.66. Contrast-to-noise-ratio (CNR) values were estimated by subtraction of the mean SNR values of the myocardium from the mean SNR values of the left ventricular blood pool. The signal intensity profile along a circular trajectory inside the myocardium was analyzed for a mid-ventricular short axis view. The results were labeled using the common segmentation of the myocardium [97].

^{1}H imaging was performed using 3D CINE Flash imaging (Matrix size 256x256, TE/TR 1.84/29ms, voxel size 1.4x1.4x4mm³, TA 0:16 min). Standard cardiac views along the short and long axis of the heart were acquired. The obtained slice positions were subsequently used for slice positioning for 3D ^{23}Na imaging and for post processing of 3D radial sodium datasets.

4.11.3.1 Sodium 2D gradient echo MR imaging

^{23}Na short axis images were acquired using untriggered gradient echo (3D FLASH) imaging (FOV 240 x 320, TE/TR 1.91/ 28 ms; TA 6:16 min; voxel size (5 x 5 x 15) mm³, averages 35, Bandwidth/pixel 120 Hz, calibrated flip angle 28°, 8 slices per slab)

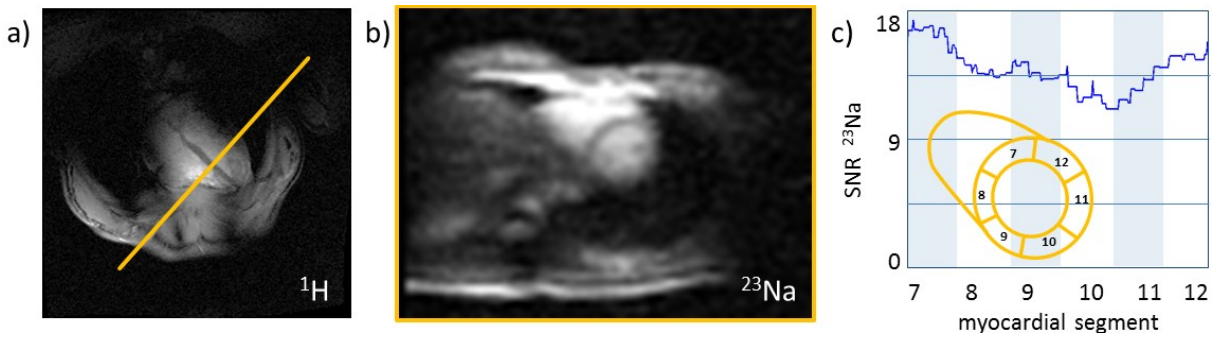

Figure 72: ***(a)*** *A ^{1}H four chamber view provided by the single dipole element for localization.* ***(b)*** *^{23}Na short axis view acquired with the four channel loop array at the slice position indicated in the four chamber view* ***(c)*** *SNR evaluation on a trajectory following the myocardium around the left ventricle. The standardized myocardial segment model proposed in* [97] *is illustrated in orange.*

Figure 72 illustrates the results of 3D GRE imaging together with slice positioning based on proton imaging. The additional proton element enabled planning of standard cardiac views in a clinical workflow for subsequent sodium imaging. For 3D GRE imaging an in-plane resolution of (5 x 5) cm² and a slice thickness of 15mm was found to be feasible. The SNR

evaluated over all volunteers was found to be 16±5 in the blood pool and 11±4 in the myocardium. This led to a contrast to noise ratio of 5±1.

4.11.3.2 Sodium 3D radial acquisition MR imaging

^{23}Na 3D datasets were acquired with a density-adapted 3D radial acquisition technique (TE/ TR 0.4/ 11 ms, T_{RO} 7.1 ms, FA 36°, projections 10000, averages 10, voxel size 6 x 6 x 6 mm³, TA 18:20 min). For retrospective triggered reconstruction an acoustic cardiac gating device (easyACT, MRI.Tools GmbH, Germany) [95] was used to capture the heart cycles during image acquisition. The normal vectors extracted from ^{1}H DICOM images were used offline in a Matlab routine to extract the standard cardiac views from the reconstructed 3D dataset. Three reconstruction modi were applied on the 3D datasets:

(i) untriggered reconstruction of the acquired data

(ii) Triggered reconstruction of the data using a time resolution of 0.1 s and time steps of 0.05s. With this approach ^{23}Na CINE images with 20 frames per heart cycle were reconstructed from the 3D acquisition.

(iii) Triggered selective reconstruction of the diastole. Based on the trigger information data acquired during systole was discarded.

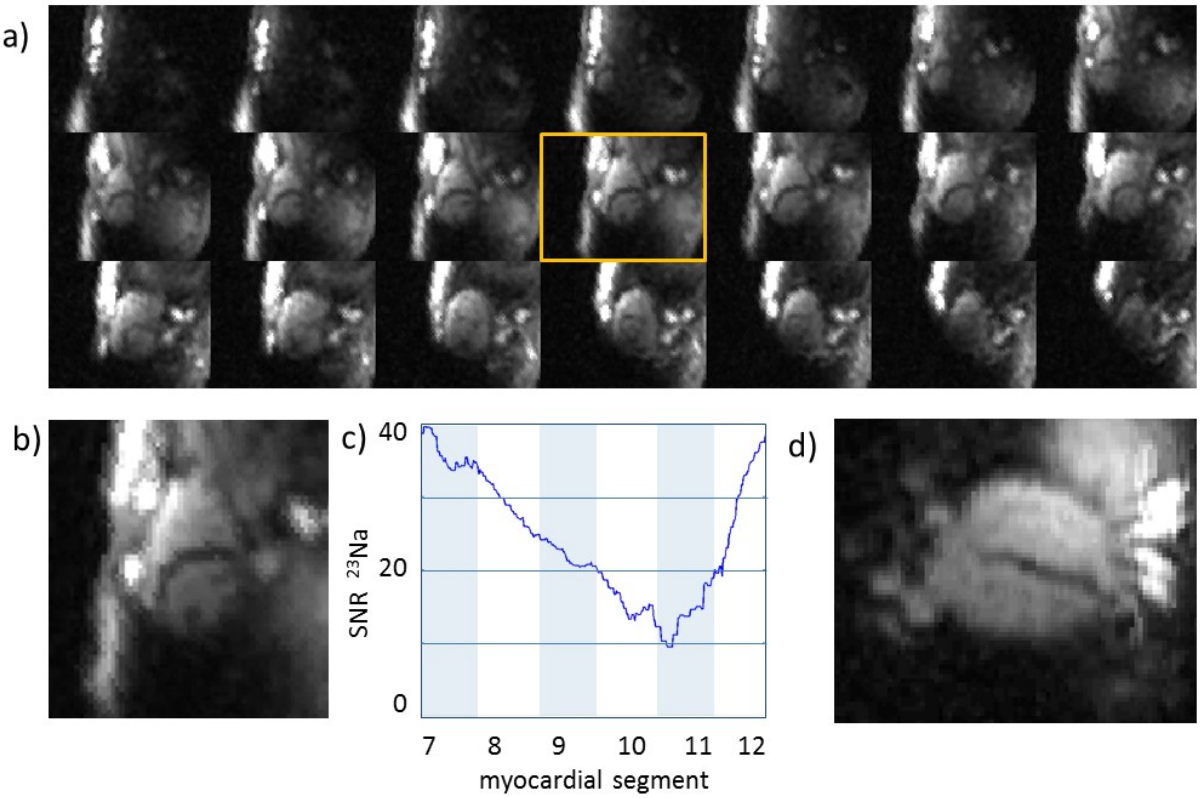

Figure 73: *Cardiac images derived from a 3D dataset with an isotropic spatial resolution of 6mm acquired with a 3D radial sequence. Standard cardiac views were extracted using normal vectors from ^{1}H image positioning.* ***(a)*** *A stack of short axis views covering the whole heart from the apex to the atrium.* ***(b)*** *Mid-ventricular short axis view used for SNR evaluation.* ***(c)*** *SNR evaluation on a trajectory following the myocardium around the left ventricle.* ***(d)*** *Four chamber view extracted from the 3D dataset.*

Using the 3D radial sequence dedicated for ^{23}Na imaging a spatial resolution of 6mm isotropic was achieved, which is promising to reduce partial volume effects in the slice direction. Figure 73 surveys the results reconstructed from 3D imaging without respect to cardiac triggering. A stack of short axis views shows the consistent image quality throughout the complete heart. A SNR of 40±4 in the blood pool and 27±3 in the myocardium led to a blood myocardium contrast of 13±1 for a mid-ventricular short axis view.

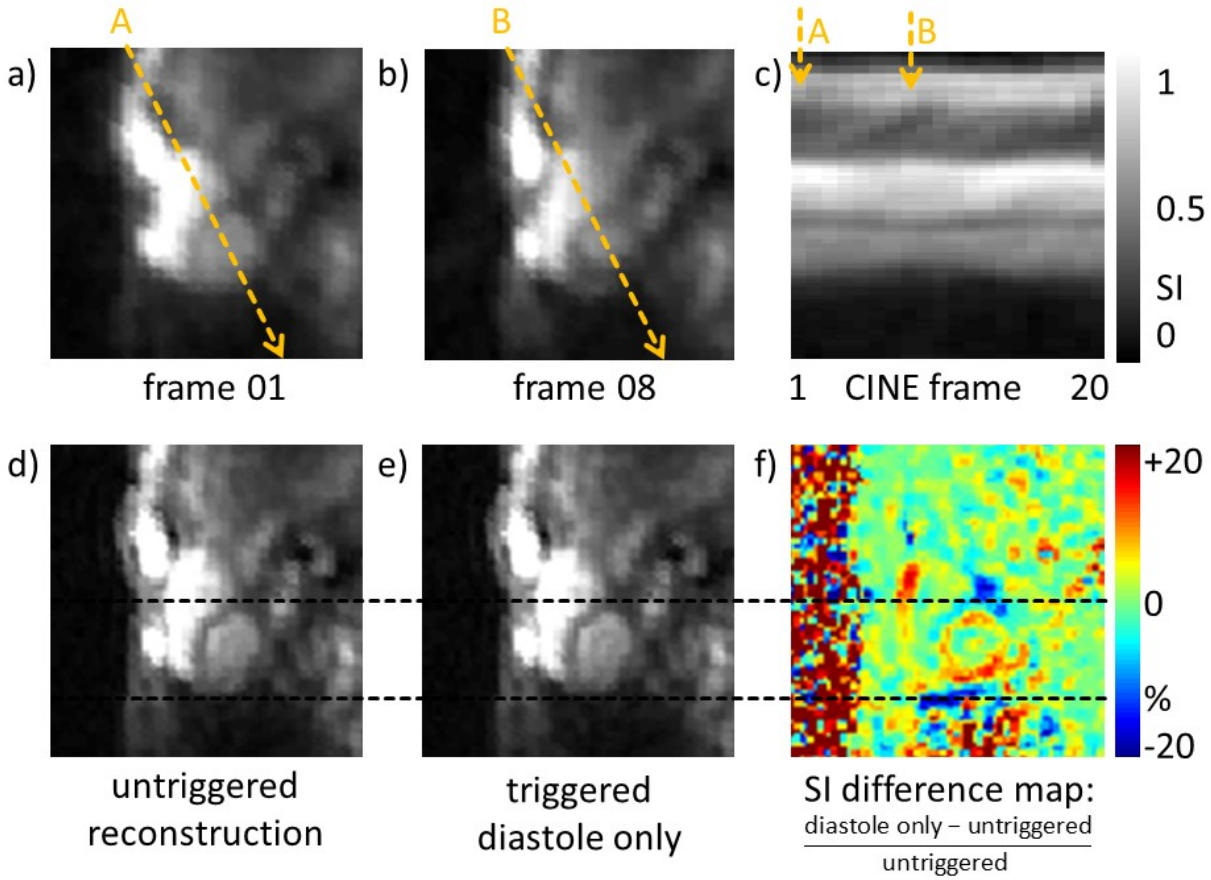

Figure 74: *Cardiac CINE images reconstructed from a 3D dataset with an isotropic spatial resolution of 6mm acquired with a 3D radial sequence. Retrospective triggering was applied during reconstruction using a time steps of 0.05s and time frames of 0.1s. Short axis views were extracted using the normal vector from ^{1}H image positioning.* ***(a)*** *Mid-ventricular short axis CINE frame in diastole.* ***(b)*** *Mid-ventricular short axis CINE frame in systole.* ***(c)*** *Time resolved signal evolution extracted on a line along the long axis of the heart, as depicted in a) and b), for all 20 frames of the CINE acquisition. The line shown in a) and b) are marked by the arrows A and B.* ***(d)*** *Untriggered reconstruction based on the complete dataset.* ***(e)*** *Selective reconstruction discarding the frames 05-12 of the systole part of the cardiac cycle.* ***(f)*** *The difference map of the untriggered and the triggered reconstruction reveals a signal gain of +20% of the triggered image in the blood pool regions nearby the myocardium, leading to a better delineation of blood/myocardium.*

Figure 74 illustrates the sodium CINE imaging capabilities of the proposed RF array together with the dedicated 3D sequence and cardiac triggering. Figure 74 a,b show two exemplary frames of the CINE dataset consisting of 20 frames. To illustrate the movement and contrast throughout the cardiac cycle, a line along the long axis of the heart is extracted from every frame and surveyed in Figure 74 c. With equation (2-10) the SNR of every single CINE frame can be estimated to 0.32 times the SNR of the untriggered image, resulting in a mean SNR of 12 in the blood pool and a mean SNR of 8 in the myocardium. Figure 74 d-f illustrates the impact of triggering for the delineation of the myocardium. When reconstructing the 3D

dataset retrospectively triggering to diastole, the local blood/myocardium contrast in the image areas affected by the contraction of the heart increases by 20%.

5. Discussion

During the time period 2011 to 2014 a vast variety of research connected with ultrahigh field MRI was conducted and pushed the field a major step towards clinical applicability. By 2010 the field had a strong focus on brain imaging, as functional MRI promised timely benefits from UHF MRI, while the concomitant technological challenges were reduced to a minimum by the limited size of the head and the static and reproducibly well-defined position of the brain. While UHF brain imaging is still a vibrant field of research that delivers new concepts and methods to be migrated to the entire field, other application are catching up. Cardiac MRI [145] and musculoskeletal MRI [107] have also produced evidence that UHF MRI is of benefit for future clinical imaging.

This work contributes to the radio frequency technology essential to exploit the benefits of UHF MRI, most prominently by pushing the limit of available transmit and receive elements for cardiac imaging at 7.0 T to 32 independent channels for the time being. As can be appreciated in the results section, the underlying knowledge about design principles was acquired by designing an eight-channel transceiver array for CMR, that already provided diagnostic image quality within clinical acceptable scan times, while exhibiting the challenges of restricted transmission field shaping and parallel imaging capabilities.

Given the presented 32 channel transceiver RF array the preferred transmit power amplifier would consists of 32 independent signal sources to apply an individual phase and amplitude to each channel. Unfortunately the majority of current UHR MRI Systems are only equipped with a single power amplifier, with eight channel RF amplifier arrays slowly becoming available. But the principle necessity for those systems is recognized and a 32 channels RF amplifier array is in the state of ongoing research [146]. Accepting the current limitation the 32 channel transceiver array is designed with a power splitting network that allows the migration to every single channel, eight channel or ultimately a 32 channel RF amplifier setup. This setup limits the transmission setting to different phase values for the single channels, easily introduced by additional cable length, while the power is split equally. The following transmission field optimization also follows this approach and was limited to phase optimization.

The transmission field shaping was a major issue to be tackled for all RF arrays presented in this work to achieve diagnostic image quality. During the work on this thesis there was no

established procedure for absolute valued transmission field mapping available for in-vivo CMR applications at UHF, although pioneering results within acceptable scan times were reported [61] and may become an option in near future. Relative B_1^+ mapping techniques resulting in phase maps are easier to implement, but B_1^+ shimming based on phase information only disregards significant differences in sensitivity of elements in the vicinity and elements located further away, resulting in field combinations far from the ideal case. Therefore transmission field shaping in this work was based on simulated B_1^+-field distributions. On the one hand this leads to very well defined 3D field distributions inside the entire region of interest and enables transmission field shaping for multi-oblique slices commonly used in CMR. On the other hand the simulation necessarily relies on the chosen human voxel model incorporated in the simulation. This leads to field results that only resemble the reality as good as the real subject matches the voxel model. For the presented pre-clinical studies the BMI range of the subjects was centered around the BMI of the used voxel model. With an increasing number of human voxel models of different gender, age and BMI becoming available (The Virtual Family, IT IS Foundation, Zurich, Switzerland) this drawback is offset. The simulation results for the 32 channel RF array show impressive capabilities for transmit homogeneity adjustments throughout the heart for the exemplarily chosen four chamber cardiac standard view. Admittedly, the focus on B_1^+ homogeneity comes at the cost of B_1^+ efficiency. In reality the model-subject discrepancy lead to slightly reduced homogeneity. The investigation of B_1^+shimming with the 16 channel dipole array revealed that a homogeneous solution does not compromise the efficiency as much for the dipole elements versus the loop elements. This result is backed up by the previously described symmetric B_1^+distributions of dipole elements [130]. This preliminary result asks for further research on dipole transceiver arrays with respect to SNR performance and g-factor assessment. Another promising direction for further research on cardiac arrays is the use of dynamic B_1^+ shimming and the application of spoke RF pulses, closely related with the availability and capabilities of multi-channel power amplifier arrays. Sophisticated implementations are reported for coronary MR angiography [147], renal MR angiography [58] at 7.0 T which all use cascades of dynamic B_1^+ shimming stages to balance the needs of preparation techniques such as inversion or fat suppression with navigator gated respiratory motion compensation and rapid imaging techniques. To this end transmission schemes using spokes provide means to balance B_1^+ efficiency against B_1^+ homogeneity which might even benefit from the variety of transmission fields provided by 32 and more independent transceiver channels [61,148].

Regarding patient safety and applicable transmit power estimation numerical simulations play again an important role. The same model-subject discrepancy applies and therefore with the exception of the eight channel array all transceiver arrays were evaluated using two independent simulations using a male and a female voxel model. The comparable results in all cases underline the validity of the simulated SAR values for all subjects included in the in-vivo study. For reasons of safety the more conservative value of both models was chosen to set the power limits for the in-vivo studies. A patient specific estimation of the SAR by means of MR acquisitions prior to the image acquisition is reported for the human head [149,150] and may be translated for body imaging in future. Regardless of the SAR estimation technique, SAR values are only a surrogate for RF induced tissue heating. A maximum rise of 1Kelvin in tissue temperature is given as the limit in the regulatory norms [81]. The SAR evaluation in compliance with the regulatory norms does not consider the influences of thermoregulation processes, i.e. increased perfusion and convection on the body surface. For brain MRI deep lying localized SAR hotspots are reported [151], while in the assessments of the surface RF arrays in this work the local SAR maxima are exclusively found on the skin, where thermoregulation is most effective. Thinking about direct MR temperature supervision at UHF body MRI in the future the applicable transmit power can be expected to rise significantly. As the achieved flip angles for deep lying regions of the body, especially the heart, were SAR restricted in every study, a further step in contrast may be hidden in the current way of limiting the transmit power.

All presented RF coils do not require patient specific tuning and matching. This accelerates the workflow of subject preparation significantly, while careful assessments of the RF characteristics during the initial studies were performed to prove the validity of this approach for every single RF array. The BMI of the subjects included in the studies admittedly did not include overweight and obese subjects. But as tuning and matching are mainly affected by the loading conditions in the vicinity of the coil, the influence of BMI was found to be small, while a much stronger influence was observed in case of air gaps between RF array and subject due to suboptimal fitting of the RF array. This problem was recognized for the tailored, yet rigid eight channel RF array and was mitigated by the modular approach of the 32 channel coil. With the small modules and flexible intersections air gaps almost disappear for both genders and resulted in very stable loading conditions.

The 8, 16 and 32 channel transceiver coil arrays support the acquisition of high spatial resolution images of the heart at 7.0 T. A spatial resolution for 2D CINE FLASH imaging of

the heart as good as (1.4 x 1.4 x 4) mm^3 or even (1.1 x 1.1 x 2.5) mm^3 was achieved within a single breath hold scan. The eight channel RF array showed g-factors of 2 or less, what is commonly considered to indicate an acceptable noise amplification, for one dimension acceleration factors of up to R=3. The 32 channel array supports acceleration with reduction factors of R=4 in two dimensions with g-factors below 2. This parallel imaging performance affords the acquisition of up to 4 slices per breath-hold with a clinically acceptable image quality. The evaluation of 3D acquisition techniques and real-time imaging using the proposed coil array is conceptually appealing for further research, which was beyond the scope of this work though. The overall image quality and the high spatial resolution help to reduce partial volume effects. These improvements may be particularly useful for visualizing small rapidly moving structures such as valve cusps, assessing subtle anatomical features such as trabeculae, or extending morphologic assessment to the right ventricle [128].

The benefits of the sensitivity gain inherent to UHF-MR together with the SNR gain of a closely fitting local 6 channel TX/RX coil array were exploited for high spatial resolution ophthalmic imaging. The results demonstrate that the proposed coil design affords uniform signal intensity across a region of interest encompassing the eye and facilitates the depiction of subtle anatomical details of the eye. Our in vivo feasibility study using the proposed six-channel array together with a 2D gradient echo imaging protocol yielded a 2% signal intensity change for the vitreous humor along a profile perpendicular to the line connecting the lens with the retina. The spatial resolution was as good as (0.2 x 0.2 x 1.0) mm3. Unlike previous studies we did not use general anesthesia for high spatial resolution imaging of the eye [152]. Imaging a relatively small field of view is another challenge of ophthalmic MRI since it bears the risk of aliasing artifacts superimposed to the eye. For this, parallel transmit techniques using multi-channel TX/RX coil arrays might be productively employed for spatially selective excitation [153,154] to enable zoomed imaging by selectively excitation of a FOV smaller than the object size. Progress in ophthalmic MRI at 7.0 T may serve to enhance the capabilities of MR image based biometry with the ultimate goal to support advanced intraocular lens implantation or refilling procedures that restore visual function and accommodation.

The results on sodium MRI of the human heart demonstrate the feasibility and opportunities of x-nuclei body imaging at 7.0 T. The proposed RF coil setup exhibits adequate RF characteristics, B_1^+ homogeneity and penetration depth for sodium imaging of the heart at 7.0 T. This resulted in images of notable SNR within clinically acceptable scan times for free

breathing, cardiac triggered and untriggered acquisitions. The SNR of the myocardium did not drop below 9 in any volunteer or position for the evaluated mid-ventricular short axis views. This leads to a clear delineation also in deep lying regions of the heart, which was reported to be an issue in a previous 3T CMR study [155]. Efficient RF excitation of large body parts is a challenging task. At 3T whole body results were reported using a 16-rung birdcage resonator body coil for ^{23}Na MRI [156]. However, as available transmit power is limited, the high transmit power requirements of volume coils limit the flip angles for short excitation pulses used in sodium MRI. The higher efficiency of a local transceiver array releases this technological constraint with the applicable flip angles only restricted by the SAR constraints. The use of a density-adapted 3D radial acquisition technique exhibited a SNR of about 180% compared to the used 3D gradient echo sequence. The isotropic resolution of the 3D radial MRI acquisitions allows reconstruction of arbitrary slices including a stack of short axis and four chamber standard cardiac views from a single acquisition. The development of a tailored local transceiver RF coil array in combination with a dedicated sequence ultimately enabled sodium CINE imaging of the heart with 10 frames per cardiac cycle within a 18 min acquisition. Cardiac triggering can be considered beneficial to produce a sharp diastolic image, as the delineation of the myocardium and the blood pool increased by sorting out data acquired during systole. A two channel transmit loop together with an 8 channel receive array was reported to be feasible for sodium cardiac imaging [157] at 3T. The measured Q ratio of 8 for the proposed four channel transceiver array leaves reasonable space for further subdivision of the elements into an array of 8 or 16 TX/RX channels to further boost SNR and spatial resolution together with scan time shortening. To increase the quality of the proton imaging capabilities we anticipate the incorporation of multiple ^{1}H elements into the ^{23}Na array in the anterior and posterior sections of the array. This can either be done by dipole elements inside the loops or overlapping loops for proton imaging as reported previously for a lower abdomen coil [158]. In summary, the proposed transceiver array enables sodium imaging of the human heart at 7T with reasonable SNR throughout the whole heart within clinical acceptable scan times and can foster future clinical studies on myocardial physiology at 7T.

To conclude, the range of transceiver arrays developed in this work provides a technological basis for the future clinical assessment of parallel transmit techniques designed for ultrahigh magnetic field MRI at 7.0 T using proton and sodium imaging. This work demonstrated the feasibility of the proposed 4, 8, 16 and 32 channel transceiver arrays for UHF cardiac MR as well as for musculoskeletal applications including spine and shoulder imaging. Abdominal imaging and other large volume MRI applications can be equally supported by rearranging the

positioning of the building block modules. The full capabilities of the modular 32 channel transceiver array will be explored with upcoming 32 channel transmit array and might ultimately lead to a body array for 7.0 T consisting of 64 or even more independent transceiver channels. The presented modular RF array approach supports this already today.

References

1. Rabi I, Zacharias J, Millman S, Kusch P. A New Method of Measuring Nuclear Magnetic Moment. Phys. Rev. 1938;53(4):318.
2. Lauterbur P. Image Formation by Induced Local Interactions: Examples Employing Nuclear Magnetic Resonance. Nature 1973;242(5394):190–1.
3. Blamire A. The technology of MRI - the next 10 years? British Journal of Radiology 2008;81(968):601–17.
4. Shah RV, Abbasi SA, Kwong RY. Role of Cardiac MRI in Diabetes. Curr Cardiol Rep 2014;16(2).
5. Cardiac magnetic resonance imaging for the diagnosis of coronary artery disease: An evidence-based analysis. Toronto, Ont: Medical Advisory Secretariat, Ontario Ministry of Health and Long-Term Care; 2010.
6. Magnetic resonance imaging (MRI) for the assessment of myocardial viability: An evidence-based analysis. Toronto, Ont: Medical Advisory Secretariat, Ontario Ministry of Health and Long-Term Care; 2010.
7. Lupo JM, Li Y, Hess CP, Nelson SJ. Advances in ultra-high field MRI for the clinical management of patients with brain tumors. Current Opinion in Neurology 2011;24(6):605–15.
8. Snyder CJ, DelaBarre L, Metzger GJ, van de Moortele P, Akgun C, Ugurbil K et al. Initial results of cardiac imaging at 7 Tesla. Magn Reson Med 2009;61(3):517–24.
9. Vaughan JT, Snyder CJ, DelaBarre LJ, Bolan PJ, Tian J, Bolinger L et al. Whole-body imaging at 7T: Preliminary results. Magn. Reson. Med 2009;61(1):244–8.
10. Versluis MJ, Tsekos N, Smith NB, Webb AG. Simple RF design for human functional and morphological cardiac imaging at 7tesla. J. Magn. Reson 2009;200(1):161–6.
11. Dieringer MA, Renz W, Lindel T, Seifert F, Frauenrath T, Knobelsdorff-Brenkenhoff F von et al. Design and application of a four-channel transmit/receive surface coil for functional cardiac imaging at 7T. J Magn Reson Imaging 2011;33(3):736–41.
12. Lattanzi R, Grant AK, Polimeni JR, Ohliger MA, Wiggins GC, Wald LL et al. Performance evaluation of a 32-element head array with respect to the ultimate intrinsic SNR. NMR Biomed 2010;23(2):142–51.
13. Adriany G, Ritter J, Vaughan T, Ugurbil K, van de Moortele P. Experimental Verification of Enhanced B1 Shim Performance with a Z-Encoding RF Coil Array at 7 Tesla. In: ISMRM, editor. Proc. Intl. Soc. Mag. Reson. Med. 18; 2010, p. 3831.
14. Keil B, Triantafyllou C, Hamm M, Wald L. Design Optimization of a 32-Channel Head Coil at 7T. In: ISMRM, editor. Proc. Intl. Soc. Mag. Reson. Med. 18; 2010.
15. Maderwald S, Orzada S, Schäfer LC, Bitz AK, Brote I, Kraff O et al. 7T Human in Vivo Cardiac Imaging with an 8-Channel Transmit/Receive Array. In: ISMRM, editor. Proc. Intl. Soc. Mag. Reson. Med. 17; 2009, p. 822.
16. Adriany G, Auerbach EJ, Snyder CJ, Gözübüyük A, Moeller S, Ritter J et al. A 32-channel lattice transmission line array for parallel transmit and receive MRI at 7 tesla. Magn. Reson. Med 2010;63(6):1478–85.

17. Ohliger MA, Grant AK, Sodickson DK. Ultimate intrinsic signal-to-noise ratio for parallel MRI: electromagnetic field considerations. Magn Reson Med 2003;50(5):1018–30.

18. Pruessmann KP, Weiger M, Scheidegger MB, Boesiger P. SENSE: sensitivity encoding for fast MRI. Magn Reson Med 1999;42(5):952–62.

19. Constantinides CD, Kraitchman DL, O'Brien KO, Boada FE, Gillen J, Bottomley PA. Noninvasive quantification of total sodium concentrations in acute reperfused myocardial infarction using23Na MRI. Magn. Reson. Med. 2001;46(6):1144–51.

20. Chen C, Hoult DI. Biomedical magnetic resonance technology. Bristol, New York: A. Hilger; 1989.

21. Gillies RJ. NMR in physiology and biomedicine. San Diego: Academic Press; 1994.

22. Hayes CE, Edelstein WA, Schenck JF, Mueller OM, Eash M. An efficient, highly homogeneous radiofrequency coil for whole-body NMR imaging at 1.5 T. Journal of Magnetic Resonance (1969) 1985;63(3):622–8.

23. Bloch F. Nuclear Induction. Phys. Rev. 1946;70(7):460–73.

24. Ocali O, Atalar E. Ultimate intrinsic signal-to-noise ratio in MRI. Magn. Reson. Med 1998;39(3):462–73.

25. Macovski A. Noise in MRI. Magn Reson Med 1996;36(3):494–7.

26. Hahn E. Spin Echoes. Phys. Rev. 1950;80(4):580–94.

27. Carr H. Steady-State Free Precession in Nuclear Magnetic Resonance. Phys. Rev. 1958;112(5):1693–701.

28. Hennig J, Nauerth A, Friedburg H. RARE imaging: a fast imaging method for clinical MR. Magn Reson Med 1986;3(6):823–33.

29. Haase A, Frahm J, Matthaei D, Hanicke W, Merboldt K. FLASH imaging. Rapid NMR imaging using low flip-angle pulses. Journal of Magnetic Resonance (1969) 1986;67(2):258–66.

30. Sodickson DK, Manning WJ. Simultaneous acquisition of spatial harmonics (SMASH): fast imaging with radiofrequency coil arrays. Magn Reson Med 1997;38(4):591–603.

31. Breuer FA, Blaimer M, Heidemann RM, Mueller MF, Griswold MA, Jakob PM. Controlled aliasing in parallel imaging results in higher acceleration (CAIPIRINHA) for multi-slice imaging. Magn Reson Med 2005;53(3):684–91.

32. Griswold MA, Jakob PM, Heidemann RM, Nittka M, Jellus V, Wang J et al. Generalized autocalibrating partially parallel acquisitions (GRAPPA). Magn Reson Med 2002;47(6):1202–10.

33. Shannon CE. Communication in the Presence of Noise. Proc. IRE 1949;37(1):10–21.

34. Maxwell JC. A Dynamical Theory of the Electromagnetic Field. Philosophical Transactions of the Royal Society of London 1865;155(0):459–512.

35. Rogers J, Plett C, Marsland I. Radio frequency system architecture and design.

36. Bowick C, Blyler J, Ajluni CJ. RF circuit design. 2nd ed. Amsterdam, Boston: Newnes/Elsevier; 2008.

37. Doty FD, Entzminger G, Hauck CD, Staab JP. Practical aspects of birdcage coils. J. Magn. Reson. 1999;138(1):144–54.

38. Edelstein WA, Glover GH, Hardy CJ, Redington RW. The intrinsic signal-to-noise ratio in NMR imaging. Magn. Reson. Med 1986;3(4):604–18.

39. Schenck JF. The role of magnetic susceptibility in magnetic resonance imaging: MRI magnetic compatibility of the first and second kinds. Med. Phys. 1996;23(6):815.

40. Gabriel C, Gabriel S. Compilation of the Dielectric Properties of Body Tissues at RF and Microwave Frequencies; Available from: http://www.brooks.af.mil/AFRL/HED/hedr/reports/dielectric/home.htmlhttp://www.brooks.af.mil/AFRL/HED/hedr/reports/dielectric/home.html.

41. Frauenrath T, Hezel F, Renz W, d'Orth TG de, Dieringer M, Knobelsdorff-Brenkenhoff F von et al. Acoustic cardiac triggering: a practical solution for synchronization and gating of cardiovascular magnetic resonance at 7 Tesla. J Cardiovasc Magn Reson 2010;12:67.

42. Oppelt A. Imaging systems for medical diagnostics: Fundamentals, technical solutions and applications for systems applying ionization radiation, nuclear magnetic resonance and ultrasound. 2nd ed. Erlangen: Publicis; 2005.

43. Koo C, Godley RF, Park J, McDougall MP, Wright SM, Han A. A magnetic resonance (MR) microscopy system using a microfluidically cryo-cooled planar coil. Lab Chip 2011;11(13):2197–203.

44. Wright AC, Song HK, Wehrli FW. In vivo MR micro imaging with conventional radiofrequency coils cooled to 77 degrees K. Magn Reson Med 2000;43(2):163–9.

45. Friis HT. Noise Figures of Radio Receivers. Proc. IRE 1944;32(7):419–22.

46. Lattanzi R, Sodickson DK. Ideal current patterns yielding optimal signal-to-noise ratio and specific absorption rate in magnetic resonance imaging: Computational methods and physical insights. Magn. Reson. Med 2012;68(1):286–304.

47. General Services Administration. Federal Standard 1037C, GLOSSARY OF TELECOMMUNICATION TERMS; 1996.

48. Compton R, McPhedran R, Popovic Z, Rebeiz G, Tong P, Rutledge D. Bow-tie antennas on a dielectric half-space: Theory and experiment. IEEE Trans. Antennas Propagat. 1987;35(6):622–31.

49. Yu-De Lin, Syh-Nan Tsai. Analysis and design of broadside-coupled striplines-fed bow-tie antennas. IEEE Trans. Antennas Propagat. 1998;46(3):459–60.

50. Collins CM, Yang QX, Wang JH, Zhang X, Liu H, Michaeli S et al. Different excitation and reception distributions with a single-loop transmit-receive surface coil near a head-sized spherical phantom at 300 MHz. Magn. Reson. Med. 2002;47(5):1026–8.

51. Roemer, P B, Edelstein W A, Hayes C E, Souza S P, Mueller O M. The NMR phased array. Magn. Reson. Med. 1990;16(2); 192–225.

52. Hayes CE, Roemer PB. Noise correlations in data simultaneously acquired from multiple surface coil arrays. Magn Reson Med 1990;16(2):181–91.

53. Sacolick LI, Wiesinger F, Hancu I, Vogel MW. B1 mapping by Bloch-Siegert shift. Magn. Reson. Med 2010;63(5):1315–22.

54. Bloch F, Siegert A. Magnetic Resonance for Nonrotating Fields. Phys. Rev. 1940;57(6):522–7.

55. Schneider E, Glover GH. Rapid in vivo proton shimming. Magn Reson Med 1991;18(2):335–47.

56. Ibrahim TS, Hue Y, Tang L. Understanding and manipulating the RF fields at high field MRI. NMR Biomed 2009;22(9):927–36.

57. Metzger GJ, Snyder C, Akgun C, Vaughan T, Ugurbil K, van de Moortele P. Local B1+ shimming for prostate imaging with transceiver arrays at 7T based on subject-dependent transmit phase measurements. Magn Reson Med 2008;59(2):396–409.

58. Metzger GJ, Auerbach EJ, Akgun C, Simonson J, Bi X, Uğurbil K et al. Dynamically applied B1+ shimming solutions for non-contrast enhanced renal angiography at 7.0 tesla. Magn Reson Med 2013;69(1):114–26.

59. Orzada S, Maderwald S, Poser BA, Bitz AK, Quick HH, Ladd ME. RF excitation using time interleaved acquisition of modes (TIAMO) to address B1 inhomogeneity in high-field MRI. Magn Reson Med 2010;64(2):327–33.

60. Bitz A, Orzada S, Kraff O, Maderwald S, Quick H, Solbach K, Bahr, A, Fautz H-P, Schmitt F, Ladd M. Comparison of simulation-based and measurement-based RF shimming for whole-body MRI at 7 Tesla. In: ISMRM, editor. Proc. Intl. Soc. Mag. Reson. Med. 18; 2010, p. 4720.

61. Schmitter S, DelaBarre L, Wu X, Greiser A, Wang D, Auerbach EJ et al. Cardiac imaging at 7 tesla: Single- and two-spoke radiofrequency pulse design with 16-channel parallel excitation. Magn. Reson. Med. 2013;70(5):1210–9.

62. Tarantola A. Inverse problem theory and methods for model parameter estimation. Philadelphia, PA: Society for Industrial and Applied Mathematics; 2005.

63. Katscher U, Vernickel P, Graesslin I, Boernert P. RF shimming using a mult-element transmit system in phantom and in vivo studies. In: ISMRM, editor. Proc. Intl. Soc. Mag. Reson. Med. 15; 2007.

64. Graessl A, Renz W, Hezel F, Dieringer MA, Winter L, Oezerdem C et al. Modular 32-channel transceiver coil array for cardiac MRI at 7.0T. Magn. Reson. Med. 2014;72(1):276–90.

65. Setsompop K, Wald LL, Alagappan V, Gagoski BA, Adalsteinsson E. Magnitude least squares optimization for parallel radio frequency excitation design demonstrated at 7 Tesla with eight channels. Magn Reson Med 2008;59(4):908–15.

66. Hoffmann J, Budde J, Shajan G, Pohmann R. SLICE-SELECTIVE B1 PHASE SHIMMING AT 9.4 TESLA. In: ISMRM, editor. Proc. Intl. Soc. Mag. Reson. Med. 18; 2010.

67. Kassakian PW. Convex Approximation and Optimization with Applications in Magnitude Filter Design and Radiation Pattern Synthesis; 2006.

68. Levenberg K. A method for the solution of certain non-linear problems in least squares. Quarterly Journal of Applied Mathmatics 1944;II(2):164–8.

69. Kirkpatrick S, Gelatt CD, Vecchi MP. Optimization by simulated annealing. Science 1983;220(4598):671–80.

70. Knobelsdorff-Brenkenhoff F von, Frauenrath T, Prothmann M, Dieringer M, Hezel F, Renz W et al. Cardiac chamber quantification using magnetic resonance imaging at 7 Tesla—a pilot study. European Radiology 2010;20(12):2844–52.

71. Henkelman RM. Measurement of signal intensities in the presence of noise in MR images. Med Phys 1985;12(2):232–3.

72. Kellman P, McVeigh ER. Image reconstruction in SNR units: a general method for SNR measurement. [Published erratum in Magn Reson Med 2007;58:211-212]. Magn Reson Med 2005;54(6):1439–47.

73. International Electrotechnical Commission (IEC). Medical electrical equipment. Part 2-33: Particular requirements for the safety of magnetic resonance equipment for medical diagnosis(IEC 60601-2-33). Geneva: IEC; 2006.

74. Kane Yee. Numerical solution of initial boundary value problems involving maxwell's equations in isotropic media. IEEE Trans. Antennas Propagat. 1966;14(3):302–7.

75. Taflove A, Brodwin ME. Numerical Solution of Steady-State Electromagnetic Scattering Problems Using the Time-Dependent Maxwell's Equations. IEEE Trans. Microwave Theory Techn. 1975;23(8):623–30.

76. Weiland T. A discretization model for the solution of Maxwell's equations for six-component fields. Archiv fuer Elektronik und Uebertragungstechnik 1977;31:116–20.

77. Kozlov M, Turner R. Fast MRI coil analysis based on 3-D electromagnetic and RF circuit co-simulation. J. Magn. Reson 2009;200(1):147–52.

78. Christ A, Kainz W, Hahn EG, Honegger K, Zefferer M, Neufeld E et al. The Virtual Family--development of surface-based anatomical models of two adults and two children for dosimetric simulations. Phys Med Biol 2010;55(2):N23-38.

79. Gabriel S, Lau RW, Gabriel C. The dielectric properties of biological tissues: II. Measurements in the frequency range 10 Hz to 20 GHz. Phys. Med. Biol. 1996;41(11):2251–69.

80. Vaughan JT, Griffiths JR. RF coils for MRI. Chichester: Wiley; 2012.

81. International Electrotechnical Commission (IEC). Medical electrical equipment. Part 2-33: Particular requirements for the safety of magnetic resonance equipment for medical diagnosis(IEC 60601-2-33). Geneva: International Electrotechnical Commission; 2006.

82. Institute of Electrical and Electronics Engineers (IEEE). IEEE C95.3: IEEE; 2002.

83. Seifert F, Wübbeler G, Junge S, Ittermann B, Rinneberg H. Patient safety concept for multichannel transmit coils. J Magn Reson Imaging 2007;26(5):1315–21.

84. Schaefers G. Testing MR Safety and Compatibility. IEEE Eng. Med. Biol. Mag. 2008;27(3):23–7.

85. World Health Orginization. The top 10causes of death, factsheet No.310. [February 19, 2014]; Available from: http://who.int/mediacentre/factsheets/fs310/en/.

86. World health report, 2013: Research for unversal health coverage. Geneva: World Health Organization; 2013.

87. Knobelsdorff-Brenkenhoff F von, Schulz-Menger J. Cardiovascular magnetic resonance imaging in ischemic heart disease. J. Magn. Reson. Imaging 2012;36(1):20–38.

88. Hundley WG, Bluemke DA, Finn JP, Flamm SD, Fogel MA, Friedrich MG et al. ACCF/ACR/AHA/NASCI/SCMR 2010 expert consensus document on cardiovascular magnetic resonance: a report of the American College of Cardiology Foundation Task Force on Expert Consensus Documents. J. Am. Coll. Cardiol 2010;55(23):2614–62.

89. Gerber BL, Raman SV, Nayak K, Epstein FH, Ferreira P, Axel L et al. Myocardial first-pass perfusion cardiovascular magnetic resonance: history, theory, and current state of the art. J Cardiovasc Magn Reson 2008;10(1):18.

90. Wagner A, Mahrholdt H, Holly TA, Elliott MD, Regenfus M, Parker M et al. Contrast-enhanced MRI and routine single photon emission computed tomography (SPECT) perfusion imaging for detection of subendocardial myocardial infarcts: an imaging study. The Lancet 2003;361(9355):374–9.

91. Suttie JJ, DelaBarre L, Pitcher A, van de Moortele PF, Dass S, Snyder CJ et al. 7 Tesla (T) human cardiovascular magnetic resonance imaging using FLASH and SSFP to assess cardiac function: validation against 1.5 T and 3 T. NMR Biomed 2012;25(1):27–34.

92. Niendorf T, Sodickson D, Krombach G, Schulz-Menger J. Toward cardiovascular MRI at 7 T: clinical needs, technical solutions and research promises. European Radiology 2010;20(12):2806–16.

93. Brandts A, Westenberg JJM, Versluis MJ, Kroft LJM, Smith NB, Webb AG et al. Quantitative assessment of left ventricular function in humans at 7 T. Magn. Reson. Med 2010;64(5):1471–7.

94. van Elderen SGC, Versluis MJ, Westenberg JJM, Agarwal H, Smith NB, Stuber M et al. Right coronary MR angiography at 7 T: a direct quantitative and qualitative comparison with 3 T in young healthy volunteers. Radiology 2010;257(1):254–9.

95. Frauenrath T. Acoustic method for synchronization of Magnetic Resonance Imaging (MRI). Acta Acustica united with Acustica 2008;94(1):148–55.

96. Phibbs B. The human heart: A basic guide to heart disease. 2nd ed. Philadelphia: Lippincott Williams & Wilkins; 2007.

97. Cerqueira MD, Weissman NJ, Dilsizian V, Jacobs AK, Kaul S, Laskey WK et al. Standardized myocardial segmentation and nomenclature for tomographic imaging of the heart. A statement for healthcare professionals from the Cardiac Imaging Committee of the Council on Clinical Cardiology of the American Heart Association. Int J Cardiovasc Imaging 2002;18(1):539–42.

98. Madelin G, Regatte RR. Biomedical applications of sodium MRI in vivo. J. Magn. Reson. Imaging 2013;38(3):511–29.

99. Kim RJ, Lima JA, Chen EL, Reeder SB, Klocke FJ, Zerhouni EA et al. Fast 23Na magnetic resonance imaging of acute reperfused myocardial infarction. Potential to assess myocardial viability. Circulation 1997;95(7):1877–85.

100. Rochitte CE, Kim RJ, Hillenbrand HB, Chen EL, Lima JA. Microvascular integrity and the time course of myocardial sodium accumulation after acute infarction. Circ. Res. 2000;87(8):648–55.

101. Beer M, Sandstede J, Pabst T, Landschütz W, Harre K, Kienlin M von et al. Assessment of myocardial viability by 31P-MR-spectroscopy and 23Na-MR imaging. MAGMA 2000;11(1-2):44–6.

102. Sandstede, Joern J W, Hillenbrand H, Beer M, Pabst T, Butter F, Machann W et al. Time course of 23Na signal intensity after myocardial infarction in humans. Magn Reson Med 2004;52(3):545–51.

103. Polimeni PI. Extracellular space and ionic distribution in rat ventricle. Am. J. Physiol. 1974;227(3):676–83.

104. Jerecic R, Bock M, Nielles-Vallespin S, Wacker C, Bauer W, Schad LR. ECG-gated 23Na-MRI of the human heart using a 3D-radial projection technique with ultra-short echo times. MAGMA 2004;16(6):297–302.

105. Konstandin S, Schad LR. Two-dimensional radial sodium heart MRI using variable-rate selective excitation and retrospective electrocardiogram gating with golden angle increments. Magn. Reson. Med. 2013;70(3):791–9.

106. Parish TB, Fieno DS, Fitzgerald SW, Judd RM. Theoretical basis for sodium and potassium MRI of the human heart at 1.5 T. Magn. Reson. Med. 1997;38(4):653–61.

107. Trattnig S, Zbýň Š, Schmitt B, Friedrich K, Juras V, Szomolanyi P et al. Advanced MR methods at ultra-high field (7 Tesla) for clinical musculoskeletal applications. Eur Radiol 2012;22(11):2338–46.

108. Krug R, Stehling C, Kelley, Douglas A. C., Majumdar S, Link TM. Imaging of the Musculoskeletal System In Vivo Using Ultra-high Field Magnetic Resonance at 7 T. Investigative Radiology 2009;44(9):613–8.

109. Deligianni X, Bär P, Scheffler K, Trattnig S, Bieri O. High-resolution Fourier-encoded sub-millisecond echo time musculoskeletal imaging at 3 Tesla and 7 Tesla. Magn. Reson. Med. 2013;70(5):1434–9.

110. Regatte RR, Schweitzer ME. Ultra-high-field MRI of the musculoskeletal system at 7.0T. J. Magn. Reson. Imaging 2007;25(2):262–9.

111. Strickland CD, Kijowski R. Morphologic Imaging of Articular Cartilage. Magnetic Resonance Imaging Clinics of North America 2011;19(2):229–48.

112. Zhao W, Cohen-Adad J, Polimeni JR, Keil B, Guerin B, Setsompop K et al. Nineteen-channel receive array and four-channel transmit array coil for cervical spinal cord imaging at 7T. Magn. Reson. Med. 2013:n/a.

113. Brown R, Deniz C, Zhang B, Chang G., Sodickson DK, Wiggins G. Design and Application of Combined 8-Channel Transmit and 10-Channel Receive Arrays and Radiofrequency Shimming for 7-T Shoulder Magnetic Resonance Imaging. Invest Radiol 2013.

114. Tartaglione T, Pagliara MM, Sciandra M, Caputo CG, Calandrelli R, Fabrizi G et al. Uveal melanoma: evaluation of extrascleral extension using thin-section MR of the eye with surface coils. Radiol med 2014.

115. Berkowitz BA, Townsend KA, Wollstein G, Schuman JS. Clinical application of MRI in ophthalmology. NMR Biomed. 2008;21(9):997–1002.

116. Wollstein G, Paunescu LA, Ko TH, Fujimoto JG, Kowalevicz A, Hartl I et al. Ultrahigh-resolution optical coherence tomography in glaucoma. Ophthalmology 2005;112(2):229–37.

117. Walter U, Niendorf T, Graessl A, Rieger J, Krüger P, Langner S et al. Ultrahigh field magnetic resonance and colour Doppler real-time fusion imaging of the orbit – a hybrid tool for assessment of choroidal melanoma. Eur Radiol 2014;24(5):1112–7.

118. Récsán Z, Karlinger K, Fodor M, Zalatnai A, Papp M, Salacz G. MRI for the Evaluation of Scleral Invasion and Extrascleral Extension of Uveal Melanomas. Clinical Radiology 2002;57(5):371–6.

119. Wuerfel J, Sinnecker T, Ringelstein EB, Jarius S, Schwindt W, Niendorf T et al. Lesion morphology at 7 Tesla MRI differentiates Susac syndrome from multiple sclerosis. Mult. Scler. 2012;18(11):1592–9.

120. Sinnecker T, Dörr J, Pfueller CF, Harms L, Ruprecht K, Jarius S et al. Distinct lesion morphology at 7-T MRI differentiates neuromyelitis optica from multiple sclerosis. Neurology 2012;79(7):708–14.

121. Richdale K, Wassenaar P, Teal Bluestein K, Abduljalil A, Christoforidis JA, Lanz T et al. 7 Tesla MR imaging of the human eye in vivo. J. Magn. Reson. Imaging 2009;30(5):924–32.

122. Gräßl A, Winter L, Thalhammer C, Renz W, Kellman P, Martin C et al. Design, evaluation and application of an eight channel transmit/receive coil array for cardiac MRI at 7.0T. European journal of radiology 2013;82(5):752–9.

123. Hardy CJ, Cline HE, Giaquinto RO, Niendorf T, Grant AK, Sodickson DK. 32-element receiver-coil array for cardiac imaging. Magn. Reson. Med 2006;55(5):1142–9.

124. Bottomley PA, Olivieri CHL, Giaquinto R. What is the optimum phased array coil design for cardiac and torso magnetic resonance? Magn. Reson. Med 1997;37(4):591–9.

125. Kramer CM, Barkhausen J, Flamm SD, Kim RJ, Nagel E. Standardized cardiovascular magnetic resonance imaging (CMR) protocols, society for cardiovascular magnetic resonance: board of trustees task force on standardized protocols. J Cardiovasc Magn Reson 2008;10(1):35.

126. Thalhammer C, Renz W, Winter L, Hezel F, Rieger J, Pfeiffer H et al. Two-Dimensional sixteen channel transmit/receive coil array for cardiac MRI at 7.0 T: Design, evaluation, and application. J. Magn. Reson. Imaging 2012;36(4):847–57.

127. Butler J, Lowe R. Beam forming matrix simplifies design of electronically scanned antennas. Electronic Design 1961(9):170–3.

128. Knobelsdorff-Brenkenhoff F von, Tkachenko V, Winter L, Rieger J, Thalhammer C, Hezel F et al. Assessment of the right ventricle with cardiovascular magnetic resonance at 7 Tesla. J Cardiovasc Magn Reson 2013;15(1):23.

129. Winter L, Kellman P, Renz W, Gräßl A, Hezel F, Thalhammer C et al. Comparison of three multichannel transmit/receive radiofrequency coil configurations for anatomic and functional cardiac MRI at 7.0T: implications for clinical imaging. Eur Radiol 2012;22(10):2211–20.

130. Raaijmakers AJE, Ipek O, Klomp DWJ, Possanzini C, Harvey PR, Lagendijk JJW et al. Design of a radiative surface coil array element at 7 T: The single-side adapted dipole antenna. Magn. Reson. Med 2011;66(5):1488–97.

131. Winter L, Özerdem C, Hoffmann W, Santoro D, Müller A, Waiczies H et al. Design and Evaluation of a Hybrid Radiofrequency Applicator for Magnetic Resonance Imaging and RF Induced Hyperthermia: Electromagnetic Field Simulations up to 14.0 Tesla and Proof-of-Concept at 7.0 Tesla. PLoS ONE 2013;8(4):e61661.

132. Frulio N, Trillaud H, Deckers R, Lepreux S, Moonen C, Quesson B. Influence of ultrasound induced cavitation on magnetic resonance imaging contrast in the rat liver in the presence of macromolecular contrast agent. Invest Radiol 2010;45(5):282–7.

133. Koning GA, Eggermont, Alexander M M, Lindner LH, ten Hagen, Timo L M. Hyperthermia and thermosensitive liposomes for improved delivery of chemotherapeutic drugs to solid tumors. Pharm. Res. 2010;27(8):1750–4.

134. Graessl A, Langner S, Hoehne M, Niendorf T. En route to clinical ultrahigh field musculoskeletal MR using multi-purpose transceiver RF modules for spine und shoulder imaging at 7.0 T. In: ISMRM, editor. Proc. Intl. Soc. Mag. Reson. Med. 22; 2014, p. 1431.

135. Hezel F, Gräßl A, Kellman P, Niendorf T. Feasibility of Abdominal MRI at 7.0 T Using a Novel 32 Channel Transceiver Coil Array. In: ISMRM, editor. Proc. Intl. Soc. Mag. Reson. Med. 20; 2012, p. 2808.

136. Gräßl A, Renz W, Hezel F, Frauenrath T, Pfeiffer H, Hoffmann W et al. Design, Evaluation and Application of a Modular 32 Channel Transmit/Receive Surface Coil Array for Cardiac MRI at 7T. In: ISMRM, editor. Proc. Intl. Soc. Mag. Reson. Med. 20; 2012, p. 305.

137. Kraff O, Bitz AK, Kruszona S, Orzada S, Schaefer LC, Theysohn JM et al. An eight-channel phased array RF coil for spine MR imaging at 7 T. Invest Radiol 2009;44(11):734–40.

138. Graessl A, Muhle M, Schwerter M, Rieger J, Oezerdem C, Santoro D et al. Ophthalmic magnetic resonance imaging at 7 T using a 6-channel transceiver radiofrequency coil array in healthy subjects and patients with intraocular masses. Invest Radiol 2014;49(5):260–70.

139. Muhle M. Design, Simulation and Evaluation of a Transceiver Coil Array for Magnetic Resonance Imaging of the Human Eye at 7.0 Tesla. Bachelor Thesis; 2012.

140. Schwerter M. Design, Construction and Evaluation of a Transceiver Coil Array for Magnetic Resonance Imaging of the Human Eye at 7.0 Tesla. Bachelor Thesis; 2012.

141. Krueger P, Stachs O, Hadlich S, Falke K, Erbersdobler A, Hosten N et al. MR Microscopy of the Human Eye at 7.1 T and Correlation with Histopathology – Proof of Principle. Orbit 2012;31(6):390–3.

142. Berkowitz BA, McDonald C, Ito Y, Tofts PS, Latif Z, Gross J. Measuring the human retinal oxygenation response to a hyperoxic challenge using MRI: Eliminating blinking artifacts and demonstrating proof of concept. Magn. Reson. Med. 2001;46(2):412–6.

143. Nagel AM, Laun FB, Weber M, Matthies C, Semmler W, Schad LR. Sodium MRI using a density-adapted 3D radial acquisition technique. Magn Reson Med 2009;62(6):1565–73.

144. National Electrical Manufacturers Association. NEMA Standards Publication MS 1-2008 Determination of Signal-to-Noise Ratio (SNR) in Diagnostic Magnetic Resonance Imaging. Rosslyn, VA 22209: National Electrical Manufacturers Association; 2008; Available from: www.nema.org.

145. Niendorf T, Graessl A, Thalhammer C, Dieringer MA, Kraus O, Santoro D et al. Progress and promises of human cardiac magnetic resonance at ultrahigh fields: A physics perspective. Journal of Magnetic Resonance 2013;229:208–22.

146. Poulo L, Alon L, Deniz C, Haefner R, Sodickson D, Stoeckel B et al. A 32-Channel Parallel Exciter/Amplifier Transmit System for 7T Imaging. In: ISMRM, editor. Proc. Intl. Soc. Mag. Reson. Med. 19; 2011, p. 1867.

147. Metzger G, Bi X, DelaBarre L, Shah S, Ugurbil K, van de Moortele P et al. Left Coronary Artery Imaging at 7T: Initial Results Using Multiple B1+ Shimming Algorithms and Targets. In: ISMRM, editor. Proc. Intl. Soc. Mag. Reson. Med. 19; 2011, p. 116.

148. Setsompop K, Alagappan V, Gagoski B, Witzel T, Polimeni J, Potthast A et al. Slice-selective RF pulses for in vivo B1+ inhomogeneity mitigation at 7 tesla using parallel RF excitation with a 16-element coil. Magn Reson Med 2008;60(6):1422–32.

149. Voigt T, Homann H, Katscher U, Doessel O. Patient-individual local SAR determination: in vivo measurements and numerical validation. Magn Reson Med 2012;68(4):1117–26.

150. Katscher U, Voigt T, Findeklee C, Vernickel P, Nehrke K, Dossel O. Determination of Electric Conductivity and Local SAR Via B1 Mapping. IEEE Trans. Med. Imaging 2009;28(9):1365–74.

151. Greef M de, Ipek O, Raaijmakers, Alexander J E, Crezee J, van den Berg, Cornelis A T. Specific absorption rate intersubject variability in 7T parallel transmit MRI of the head. Magn Reson Med 2013;69(5):1476–85.

152. Khurana A, Eisenhut CA, Wan W, Ebrahimi KB, Patel C, O'Brien JM et al. Comparison of the diagnostic value of MR imaging and ophthalmoscopy for the staging of retinoblastoma. Eur Radiol 2013;23(5):1271–80.

153. Schneider JT, Kalayciyan R, Haas M, Herrmann SR, Ruhm W, Hennig J et al. Inner-volume imaging in vivo using three-dimensional parallel spatially selective excitation. Magn. Reson. Med 2012:n/a.

154. Zelinski AC, Angelone LM, Goyal VK, Bonmassar G, Adalsteinsson E, Wald LL. Specific absorption rate studies of the parallel transmission of inner-volume excitations at 7T. J Magn Reson Imaging 2008;28(4):1005–18.

155. Gai ND, Rochitte C, Nacif MS, Bluemke DA. Optimized three-dimensional sodium imaging of the human heart on a clinical 3T scanner. Magn. Reson. Med. 2014:n/a.

156. Wetterling F, Corteville DM, Kalayciyan R, Rennings A, Konstandin S, Nagel AM et al. Whole body sodium MRI at 3T using an asymmetric birdcage resonator and short echo time sequence: first images of a male volunteer. Phys. Med. Biol. 2012;57(14):4555–67.

157. Lanz T, Mayer M, Robson MD, Neubauer S, Ruff J, Weisser A. An 8 Channel 23Na Heart Array for Application at 3 T. In: ISMRM, editor. Proc. Intl. Soc. Mag. Reson. Med. 15; 2007, p. 241.

158. Bae K, Kim J, Furlan A, Moon C, Park B, Zhao T. Proton and sodium MR imaging of in vivo human prostate using dual-tuned body and endorectal coils at 7T. In: ISMRM, editor. Proc. Intl. Soc. Mag. Reson. Med. 18; 2010, p. 2693.

159. Graessl A, Winter L, Özerdem C, Hezel F, Fuchs K, Pfeiffer H, Hoffmann W, Niendorf T. A two-dimensional 16 Channel Dipole Transceiver Array for Cardiac MR at 7.0 T: Design, Evaluation of RF Shimming Behavior and Application in CINE Imaging. In: ISMRM, editor. Proc Intl Soc Mag Reson Med 21. Volume 21; 2013. p 395.

160. Özerdem C, Winter L, Graessl A, Paul K, Els A, Kraus O, Rieger J, Kuehne A, Dieringer A M, Hezel F, Frahm J, Niendorf T. 16 Channel Bow Tie Antenna Transceiver Coil Array for Cardiac Magnetic Resonance at 7.0 T. Magn. Reson. Med. 2015

161. Resetar A, Hoffmann S, Graessl A, Winter L, Waiczies H, Ladd M, Niendorf T, Nagel A M. Retrospectively-Gated CINE 23Na Imaging of the Heart at 7.0 Tesla Using Density-Adapted 3D Projection Reconstruction Magnetic Resonance Imaging. Magn. Reson. Imag. 2015

162. Graessl A, Ruehle A, Waiczies H, Resetar A, Hoffmann S, Rieger J, Wetterling F, Winter L, Nagel AM, Niendorf T. Sodium Magnetic Resonance Imaging of the Human Heart at 7.0T: Preliminary Results. NMR in Biomedicine 2015

List of publications

Publications in peer reviewed journals (1st author)

- Graessl A, Ruehle A, Waiczies H, Resetar A, Hoffmann S, Rieger J, Wetterling F, Winter L, Nagel AM, Niendorf T. Sodium Magnetic Resonance Imaging of the Human Heart at 7.0T: Preliminary Results. NMR in Biomedicine 2015; 28(8):967-975
- Graessl A, Muhle M, Schwerter M, Rieger J, Oezerdem C, Santoro D, Lysiak D, Winter L, Hezel F, Waiczies S, Guthoff RF, Falke K, Hosten N, Hadlich S, Krueger P, Langner S, Stachs O, Niendorf T. Ophthalmic MRI at 7.0 Tesla Using a Six-Channel Transceiver Radiofrequency Coil Array in Healthy Subjects and Patients with Intraocular Masses. Investigative radiology. 2014; 49(5):260-270.
- Graessl A, Renz W, Hezel F, Dieringer MA, Winter L, Oezerdem C, Rieger J, Kellman P, Santoro D, Lindel TD, Frauenrath T, Pfeiffer H, Niendorf T. Modular 32-channel transceiver coil array for cardiac MRI at 7.0T. Magnetic Resonance in Medicine. 2014; 72(1):276-290
- Gräßl A, Winter L, Thalhammer C, Renz W, Kellman P, Martin C, Knobelsdorff-Brenkenhoff Fv, Tkachenko V, Schulz-Menger J, Niendorf T. Design, evaluation and application of an eight channel transmit/receive coil array for cardiac MRI at 7.0T. European journal of radiology 2013;82(5):752-9.

Publications in peer reviewed journals (co-author)

- Özerdem C, Winter L, Graessl A, Paul K, Els A, Kraus O, Rieger J, Kuehne A, Dieringer A M, Hezel F, Frahm J, Niendorf T. 16 Channel Bow Tie Antenna Transceiver Coil Array for Cardiac Magnetic Resonance at 7.0 T. Magn. Reson. Med. 2015
- Resetar A, Hoffmann S, Graessl A, Winter L, Waiczies H, Ladd M E, Niendorf T, Nagel A M. Retrospectively-Gated CINE 23Na Imaging of the Heart at 7.0 Tesla Using Density-Adapted 3D Projection Reconstruction Magnetic Resonance Imaging. Magn. Reson. Imag. 2015
- Niendorf T, Paul K, Oezerdem C, Graessl A, Klix S, Huelnhagen T, Hezel F, Rieger J, Waiczies H, Frahm J, Nagel AM, Oberacker E, Winter L. W(h)ither human cardiac and body magnetic resonance at ultrahigh fields? Technical advances, practical considerations, applications, and clinical opportunities. NMR in Biomedicine 2015
- Paul K, Graessl A, Rieger J, Lysiak D, Huelnhagen T, Winter L, Heidemann R, Lindner T, Hadlich S, Zimpfer A, Pohlmann A, Endemann B, Krüger P, Langner S, Stachs O, Niendorf T. Diffusion-Sensitized Ophthalmic Magnetic Resonance Imaging Free of Geometric Distortion at 3.0 and 7.0 T: A Feasibility Study in Healthy Subjects and Patients With Intraocular Masses. Investigative Radiology 2015;50(5):309-321
- A Klix S, Els A, Paul K, Graessl A, Oezerdem C, Weinberger O, Winter L, Thalhammer C, Huelnhagen T, Rieger J, Mehling H, Schulz-Menger J, Niendorf T. On the subjective

acceptance during cardiovascular magnetic resonance imaging at 7.0 Tesla. PloS one 2015;10(1):e0117095

- Niendorf T, Paul K, Graessl A, Els A, Pohlmann A, Rieger J, Lindner T, Krueger P, Hadlich S, Langner S, Stachs O. Ophthalmologische Bildgebung mit Ultrahochfeld-Magnetresonanztomografie: technische Innovationen und wegweisende Anwendungen. Klinische Monatsblätter für Augenheilkunde. 2014;231(12):1187–1195
- Walter U, Niendorf T, Graessl A, Rieger J, Krüger P, Langner S, Guthoff RF, Stachs O. Ultrahigh field magnetic resonance and colour Doppler real-time fusion imaging of the orbit – a hybrid tool for assessment of choroidal melanoma. European radiology. 2014; 24(5):1112-1117
- Winter L, Özerdem C, Hoffmann W, Santoro D, Müller A, Waiczies H, Seemann R, Graessl A, Wust P, Niendorf T, Yacoub E. Design and Evaluation of a Hybrid Radiofrequency Applicator for Magnetic Resonance Imaging and RF Induced Hyperthermia: Electromagnetic Field Simulations up to 14.0 Tesla and Proof-of-Concept at 7.0 Tesla. PLoS ONE 2013;8(4):e61661.
- Niendorf T, Graessl A, Thalhammer C, Dieringer MA, Kraus O, Santoro D, Fuchs K, Hezel F, Waiczies S, Ittermann B, Winter L. Progress and promises of human cardiac magnetic resonance at ultrahigh fields: A physics perspective. Journal of Magnetic Resonance 2013;229:208-22.
- Knobelsdorff-Brenkenhoff Fv, Tkachenko V, Winter L, Rieger J, Thalhammer C, Hezel F, Graessl A, Dieringer MA, Niendorf T, Schulz-Menger J. Assessment of the right ventricle with cardiovascular magnetic resonance at 7 Tesla. Journal of Cardiovascular Magnetic Resonance 2013;15(1):23.
- Winter, Lukas; Kellman, Peter; Renz, Wolfgang; Gräßl, Andreas; Hezel, Fabian; Thalhammer, Christof; Knobelsdorff-Brenkenhoff, Florian; Tkachenko, Valeriy; Schulz-Menger, Jeanette; Niendorf, Thoralf; Comparison of three multichannel transmit/receive radiofrequency coil configurations for anatomic and functional cardiac MRI at 7.0T: implications for clinical imaging. Eur Radiol 2012;22(10):2210-20.
- Thalhammer C, Renz W, Winter L, Hezel F, Rieger J, Pfeiffer H, Graessl A, Seifert F, Hoffmann W, Knobelsdorff-Brenkenhoff Fv, Tkachenko V, Schulz-Menger J, Kellman P, Niendorf T. Two-Dimensional sixteen channel transmit/receive coil array for cardiac MRI at 7.0 T: Design, evaluation, and application. Journal of Magnetic Resonance Imaging 2012; 36(4):847-57.
- Santoro D, Winter L, Müller A, Vogt J, Renz W, Özerdem C, Grässl A, Tkachenko V, Schulz-Menger J, Niendorf T. Detailing Radio Frequency Heating Induced by Coronary Stents: A 7.0 Tesla Magnetic Resonance Study. PLoS ONE 2012;7(11):e49963.

Publications in peer reviewed conference proceedings (1st author)

- Graessl A, Langner S, Hoehne M, Niendorf T. En route to clinical ultrahigh field musculoskeletal MR using multi-purpose transceiver RF modules for spine und shoulder imaging at 7.0 T. In: ISMRM, editor. Proc. Intl. Soc. Mag. Reson. Med. 22. ISMRM; Milano/Italy; 2014.
- Graessl A, Rieger J, Stachs O, Langner S, Schwerter M, Muhle M, Niendorf T. High Spatial Resolution In Vivo Human Eye MRI at 7.0 Tesla in Patients with Intraocular

Masses. In: Ismrm, editor. Proc. Intl. Soc. Mag. Reson. Med. 22. ISMRM; Milano/Italy; 2014.

- Graessl A, Winter L, Özerdem C, Hezel F, Fuchs K, Pfeiffer H, Hoffmann W, Niendorf T. A two-dimensional 16 Channel Dipole Transceiver Array for Cardiac MR at 7.0 T: Design, Evaluation of RF Shimming Behavior and Application in CINE Imaging. In: Ismrm, editor. Proc Intl Soc Mag Reson Med 21. Volume 21; 2013. p 395.
- Graessl A, Schwerter M, Muhle M, Rieger J, Özerdem C, Ok A, Santoro D, Lysiak D, Stachs O, Langer S, Krueger P-C, Niendorf T. Design, Evaluation and Application of a Six-Channel Transceiver Array Tailored for In Vivo Human Eye Imaging at 7.0 T. In: Ismrm, editor. Proc Intl Soc Mag Reson Med 21. Volume 21; 2013. p 2747.
- Gräßl A, Renz W, Hezel F, Frauenrath T, Pfeiffer H, Hoffmann W, Kellman P, Martin C, Niendorf T. Design, Evaluation and Application of a Modular 32 Channel Transmit/Receive Surface Coil Array for Cardiac MRI at 7T. In: Ismrm, editor. Proc Intl Soc Mag Reson Med 20; 2012. p 305.
- Graessl A, Ruehle A, Renz W, Winter L, Pfeiffer H, Ruff J, Rieger J, Niendorf T. Sodium imaging of the heart at 7T: design, evaluation and application of a four-channel transmit/receive surface coil array. Journal of Cardiovascular Magnetic Resonance. 2013;(15):(Suppl 1):W14.

Publications in peer reviewed conference proceedings (co-author)

- Kraus O, Winter L, Dieringer MA, Graessl A, Rieger J, Oezerdem C, Hezel F, Kuehne A, Waxmann P, Pfeiffer H, Niendorf T. Local Coil versus Conventional Body Coil Transmission for Cardiac MR: B1+ Efficiency Improvements and Enhanced Blood Myocardium Contrast for 2D CINE SSFP Imaging at 3T. In: ISMRM, editor. Proc. Intl. Soc. Mag. Reson. Med. 22. ISMRM; Milano/Italy; 2014.
- Resetar A, Hoffmann SH, Graessl A, Waiczies H, Niendorf T, Nagel AM. Retrospectively gated CINE 23Na imaging of the heart at 7.0 T using density-adapted 3D projection reconstruction. In: ISMRM, editor. Proc. Intl. Soc. Mag. Reson. Med. 22. ISMRM; Milano/Italy; 2014.
- Waiczies H, Rieger J, Graessl A, Niendorf T. High Resolution Double Resonant 1H/19F RF Coil for Small Rodent MRI and MRS at 3T. In: ISMRM, editor. Proc. Intl. Soc. Mag. Reson. Med. 22. ISMRM; Milano/Italy; 2014.
- Winter L, van de Lindt T, Özerdem C, Hoffmann W, Santoro D, Müller A, Graessl A, Seeman R, Marek J, Niendorf T. Hybrid MRI/RF-Heating at 7.0 Tesla and 11.7 Tesla: Electro-Magnetic Field Simulations, Temperature Simulations/Measurements, Dipole Antenna Design and Heating Experiments. In: Ismrm, editor. Proc Intl Soc Mag Reson Med 21. Volume 21; 2013. p 833.
- Winter L, Santoro D, Müller A, Renz W, Özerdem C, Graessl A, Tkachenko V, Schulz-Menger J, Niendorf T. Detailing RF Heating Induced by Coronary Stents at 7.0T Using Numerical EMF Simulations and Heating Experiments. In: Ismrm, editor. Proc Intl Soc Mag Reson Med 21. Volume 21; 2013. p 2839.
- Fuchs K, Hezel F, Winter L, Özerdem C, Graessl A, Dieringer MA, Kraus O, Niendorf T. Feasibility of Cardiac Fast Spin Echo Imaging at 7.0 T Using a Two-Dimensional 16

Channel Array of Bowtie Transceivers. In: Ismrm, editor. Proc Intl Soc Mag Reson Med 21. Volume 21; 2013. p 1412.

- Kraus O, Dieringer MA, Hezel F, Winter L, Graessl A, Özerdem C, Niendorf T. 2D CINE SSFP Imaging At 7.0T Using 8-Channel Bowtie Antenna Transceiver Arrays: A Cardiac MR Feasibility Study. In: Ismrm, editor. Proc Intl Soc Mag Reson Med 21. Volume 21; 2013. p 580.
- Frauenrath T, Pfeiffer H, Hezel F, Dieringer MA, Winter L, Graessl A, Santoro D, Özerdem C, Renz W, Greiser A, Niendorf T. Lessons Learned from Cardiac MRI at 7.0 T: LV Function Assessment at 3.0 T Using Local Multi-Channel Transceiver Coil Arrays. In: Ismrm, editor. Proc Intl Soc Mag Reson Med 20; 2012. p 2803.
- Ok, Abdullah; Rieger, Jan; Gräßl, Andreas; Madai, Vince Istvan; Sobesky, Jan; Niendorf, Thoralf; High Spatial Resolution MR Imaging of the Carotid Arteries at 7.0 T Using an 8 Channel Transceiver Coil Array; Proc.Intl.Soc.Mag.Reson.Med.20 (2012)
- Santoro, Davide; Müller, Alexander; Winter, Lukas; Renz, Wolfgang; Gräßl, Andreas; Özerdem, Celal; Tkachenko, Valeriy; Schulz-Menger, Jeanette; Niendorf, Thoralf; Analysis of Radio Frequency Heating Induced by a Coronary Stent at 7.0 T; Proc.Intl.Soc.Mag.Reson.Med.20 (2012)
- Hezel, Fabian; Gräßl, Andreas; Kellman, Peter; Niendorf, Thoralf; Feasibility of Abdominal MRI at 7.0 T Using a Novel 32 Channel Transceiver Coil Array; Proc.Intl.Soc.Mag.Reson.Med.20 (2012)

Acknowledgement

My first thanks are due to my supervisor Professor Thoralf Niendorf for the comprehensive, yet in-depth supervision during all stages of the work towards this thesis. The strong focus on application and publication of the gained results was a key factor to achieve the presented work in the given timeframe. Based on his efforts the team of the Berlin Ultrahigh Field facility (B.U.F.F.) was always versatile, collegial and in best shape to foster leading edge research for every member. The same applies to the availability of state-of-the art MRI and RF equipment that made it a pleasure to work at B.U.F.F. I also like to give special thanks to Wolfgang Renz from Siemens for the invaluable first-hand introduction into the field of ultrahigh field MRI during the first three month of this work. The efforts of Peter Kellman from the National Institute of Health (NIH, Bethesda, US) to provide and support the SNR scaled imaging sequence added a vital part to the meaningful assessment of the developed radio frequency arrays. The work on sodium imaging of the human heart led to the first animated sodium MRI datasets of the human heart based on the collegial cooperation with Armin Nagel, Stefan Hofmann and Ana Resetar from the German Cancer Research Center (DKFZ) Heidelberg, who provided and supported the 3D radial imaging sequence for sodium imaging. I also like to acknowledge Werner Hoffmann, Harald Pfeifer and Bernd Ittermann from the Physikalisch Technische Bundesanstalt (PTB) for valuable discussions on RF technology and the thorough design and built up of multiple hardware interfaces to interconnect RF antenna arrays and the MR system. I would also like to thank Tomasz Lindel for helpful discussions on numerical optimization of transmission field settings. I wish to thank Max Muhle and Michael Schwerter for their thorough work on the orbita array during their bachelor theses that paved the way for successful follow up studies in ophthalmic MRI. It was a pleasant and instructive experience to co-supervise these theses. In the same context I want to thank Sönke Langner for adding clinical expertise connected with ophthalmic MRI as well as providing insights from a radiologist's point of view on the UHF musculoskeletal MR images.

This work was funded in part by the Helmholtz Alliance ICEMED - Imaging and Curing Environmental Metabolic Diseases, through the Initiative and Network Fund of the Helmholtz Association.

Selbstständigkeitserklärung

Ich versichere hiermit, die vorliegende Dissertation selbständig und nur unter der Verwendung der angegebenen Hilfen und Hilfsmittel angefertigt zu haben.

Andreas Gräßl Stuttgart, den 19.11.2015